Manipulation of Fullerene C_{60} Spintronic Devices via Ferromagnetic Resonance

May Catherine Wheeler

School of Physics and Astronomy

University of Leeds

Submitted in accordance with the requirements for the degree of

Doctor of Philosophy

September 2014

Intellectual Property Statement

The candidate confirms that the work submitted is her own, except where work which has formed part of jointly authored publications has been included. The contribution of the candidate and the other authors to this work has been explicitly indicated below. The candidate confirms that appropriate credit has been given within the thesis where reference has been made to the work of others.

For all publications Dr O. C*é*spedes suggested experiments, discussed results and reviewed the manuscripts. Work from the following jointly authored publications is presented in this thesis:
M. Wheeler, B. J. Hickey and O. C*é*spedes. Enhanced exchange bias of spin valves fabricated on fullerene-based seed layers, *IEEE Transactions on Magnetics* Vol. 48, No. 11, 2012. Chapter 4 section 4.3. **Work attributable to the candidate:** Deposition and measurement of samples, as well as analysis. Preparation of manuscript. **Work attributable to others:** Professor Bryan Hickey discussed results and reviewed the manuscript.

F. Al Ma'Mari, **M. Wheeler**, E. Kendrick, G. Burnell, B.J. Hickey, T. Moorsom and O. Céspedes. Direct measurement of spin polarization in ferromagnetic C_{60} interfaces using point-contact Andreev reflection, *IEEE Transactions on Magnetics* Vol. 50, No. 11, 2014. Chapter 5. **Work attributable to the candidate:** Deposition and measurement of hybrid-organic spin valves, as well as analysis of data. Helped with set up and some PCAR measurements. Reviewed and edited manuscript. **Work attributable to others:** Ms F. Al Ma'Mari and Ms E. Kendrick did the PCAR measurements. Ms F. Al Ma'Mari prepared the manuscript.

T. Moorsom, **M. Wheeler**, T. M. Khan, F. Al Ma'Mari, C. Kinane, S. Langridge, D. Ciudad, A. Bedoya-Pinto, L. Hueso, G. Teobaldi, V. K. Lazarov, D. Gilks, G. Burnell, B. J. Hickey and O. Céspedes. Spin polarised electron transfer in ferromagnet/C_{60} interfaces, *Physical Review B* Vol. 90, No. 12, 2014. Figure 4.5 in chapter 4. **Work attributable to the candidate:** Set up of sample deposition and initial characterisation of the C_{60}/Co bilayers and multilayers, including XRD and magnetometry measurements. Discussion of results. Reviewed and edited manuscript. **Work attributable to others:** Mr T. Moorsom and Dr O. Céspedes did the majority of the experimental work and analysis used in this paper.

T. Moorsom, **M. Wheeler**, T. M. Khan, F. Al Ma'Mari, G. Burnell, B. J. Hickey, V. Lazarov, D. Gilks, and O. Céspedes. Effects of spin doping and spin injection in the luminescence and vibrational spectrum of C_{60}, *Applied Physical Letters*, 105, 2014. Figures 7.7 and 7.10 in chapter 7 **Work attributable to the candidate:** Set up of sample deposition and made/measured the first samples for this purpose. General help with this work and with discussion/ideas. Reviewed and edited manuscript. **Work attributable to others:** Mr T. Moorsom and Dr O. Céspedes did the majority of the experimental work used in this paper.

Acknowledgements

Firstly, I thank my supervisor Dr Oscar Céspedes for his support, encouragement and interesting ideas throughout my PhD. Thank you to Professor Bryan Hickey for his wise words and guidance. Dr Gavin Burnell has been invaluable in my work, from helping me get to grips with Python and LabView to continuous help with discussion of my work. The group would simply not function without Dr Mannan Ali; I thank him for his willingness to help me and the rest of "team goo". I have appreciated all the advice and help from Dr Nick Porter throughout my PhD. Thank you to Ms Fatma Al Ma'Mari for being such a pleasure to work with. The work carried out with Mr Timothy Moorsom has been valuable for this research. Thank you to Dr Rowan Temple for being a great friend and tea buddy, and for turning the thesis submission into a competition! A big thanks to Ms Sophie Morley and Dr Robin Richardson who have suffered living with me (and Sophie sharing an office too) for the last couple of years and who have helped me get through the experience with my sanity intact. Thank you to everyone in the Condensed Matter group for making it an enjoyable place to work. I would like to thank the Nanodevices group in San Sebastian and in particular Professor Luis Hueso for giving me the opportunity to spend a month secondment there. I also thank Professor Robert Stamps and Mr Francisco Goncalves for their help and advice with FMR. Thank you to Dr Matthew Newman for his love, encouragement and proof reading skills. Thank you to my parents and sister, Laura, for always being there for me and for their excellent proof reading skills.

At some point everyone in the mechanical workshop has helped me and every time with a smile. Thanks for all the help in getting my experiments set up through innovative solutions. Thank you to the electronics workshop who have also been invaluable in my work and solving problems. Finally, thank you to John Turton and the late Philip Cale for the continuous flow of cryogens. John Turton has been vital to my work, particularly for helping to set up new experiments. Philip Cale was also incredibly kind and helpful. His big smile will always be missed by the Condensed Matter Group.

Abstract

C_{60} has been included in hybrid magneto-molecular devices as an active layer where the C_{60} is thermally sublimated under high vacuum and the metals are sputter deposited in-situ. Multilayer C_{60}/Co samples were measured by x-ray reflectivity and transmission electron microscopy to show that there is little interdiffusion of layers suggesting C_{60} is robust to the deposition of metals by sputtering. We have observed 25% magnetoresistance through 60 nm of C_{60} at 10 K as well as 8% magnetoresistance at room temperature through 20 nm of C_{60}. Unexpected asymmetric effects in external magnetic field were observed in some C_{60} spin valves as a result of interfacial hybridisation between C_{60} and ferromagnetic materials. It has also been shown that when C_{60} is in contact with a ferromagnetic material, spin polarised electrons from the ferromagnet are transferred into the C_{60} as a result of differences in chemical potential. This has been measured in C_{60}/Co and C_{60}/Py bilayer samples and observed via ferromagnetic resonance and point contact Andreev reflection. The molecular properties of C_{60} can be manipulated by an adjacent ferromagnetic material at ferromagnetic resonance dissipating energy into the C_{60}. This changes the frequency/energy of molecular vibrations, as well as an enhanced photoemission from the C_{60}. The changes can be correlated to spin pumping and phonon injection. The conductivity through a C_{60} layer is also increased during ferromagnetic resonance of the adjacent Py by up to 8% owing to increased phonon-assisted hopping steps.

CONTENTS

Abbreviations

AC	alternating current	AFM	atomic force microscopy
AMR	anisotropic magnetoresistance	BTK	Blonder Tinkham Klapwijk
BCS	Bardeen-Cooper-Schrieffer	DC	direct current
FCC	face centred cubic	FM	ferromagnet
FMR	ferromagnetic resonance	FWHM	full width half maximum
GMR	giant magnetoresistance	HOMO	highest occupied molecular orbital
ISHE	inverse spin Hall effect	IV	current-voltage
LUMO	lowest unnoccupied molecular orbital	MOKE	magneto optical Kerr effect
MR	magnetoresistance	MTJ	magnetic tunnel junction
NM	normal metal	PCAR	point contact Andreev reflection
PCB	printed circuit board	PL	photoluminescence
Py	permalloy: nickel/iron alloy	RF	radio frequency
SC	superconductor	STT	spin transfer torque
TEM	transmission electron microscopy	TMR	tunnel magnetoresistance
UHV	ultra high vacuum	VNA	vector network analyser
VSM	vibrating sample magnetometry	XRD	xray diffraction
XRR	xray reflection	YIG	yttrium iron garnet

CHAPTER 1

Introduction

Spintronics or spin-electronics utilises both the spin degree of freedom and charge of electrons in magnetoelectronic devices. Devices such as spin valves or magnetic tunnel junctions use the dependence of the resistivity on magnetic field: magnetoresistance (MR). The read heads in hard disk drives are composed of spintronic devices and have been in part responsible for the exponential growth of digital data storage in recent years. The increasing desire for faster, smaller and more efficient data storage has particularly driven forward research into spintronics and the prospects of second generation devices. One branch of this research is organic spintronics, which is particularly interesting because of molecular chemical flexibility and the potential to utilise molecular properties such as vibrations for novel functionalities. Organic materials are beneficial for spintronics because they generally have a low atomic mass, leading to a weak spin orbit interaction and therefore longer spin lifetimes [1]. The spin orbit interaction causes spin flip processes, so if it is small then a spin polarisation can be maintained for longer times and over greater length scales. However, diffusion is low, so the spin diffusion length is generally small, except for materials with small hyperfine interaction, for instance pure carbon. The hyperfine interaction acts to hinder the spin lifetimes [2], however it is absent in molecules such as C_{60} because of the lack of spin in the nuclei as a result of the absence of hydrogen. C_{60}, therefore, has a large spin diffusion length on the order of 100 nm at room temperature [3].

Interest in molecular electronics in general has increased in the past two decades, involving a wide range of devices such as field effect transistors [4–9], solar cells [10–13] and light emitting diodes [14–16]. A range of other molecular materials, particularly organic semiconductors, are being studied widely but the focus of my research has been C_{60} because it is a simple model molecule and is relatively easy to deposit via thermal sublimation. C_{60} is an intriguing molecule to study in terms of fundamental physics, and has been researched thoroughly since its discovery in 1985 [17]. Furthermore, C_{60} is robust to the deposition of metals on top and can thus be used in a wide range of devices [18; 19]. C_{60} has been incorporated in field effect transistors [20–22], solar cells [23–25] and in light emitting diodes [26–28]. In terms of spintronic applications, a range of molecules has been successfully used as active layers in spin valves. Spin valves are devices in which the resistance is dependent on the relative alignment of the magnetisation of two ferromagnetic electrodes, separated by a spacer layer, and

can be controlled with an external magnetic field. Successful molecules used as the spacer layer include pi-conjugated organic semiconducting oligomer (sexi-thiophene, T6) [29], tris(8-hydroxyquinolinato)aluminium (or Alq_3) [30; 31] and C_{60} [18; 32–34].

Despite there having been significant progress with regards to spin valve devices with an organic as the spacer layer, the conductivity mismatch between a metal and semiconductor remains a problem for efficient spin injection [35]. An insulating tunnel barrier can be used to overcome this problem [36] and has been used to inject spin into a range of inorganic [37; 38] and organic semiconductors [18; 32–34]. However, the high resistance of these contacts means there is room for significant improvement in making low power devices. A more desirable method for injecting spins and overcoming the conductivity mismatch problem was introduced by Ando et al [39]. Here it was shown that the conductivity mismatch problem between metals and an inorganic semiconductor, GaAs, is not a problem when spin pumping via ferromagnetic resonance (FMR) is used as the method of spin injection. More recently, spin pumping via FMR has been used to inject spin polarised electrons into a conducting polymer [40] and an organic semiconductor [41]. The inverse spin Hall effect (ISHE) is the conversion of a spin current into an electric voltage and can be used to detect a pure spin current [42]. A spin current can be thought of as two electrons travelling in opposite directions with opposite spins along a particular spin-current direction J_S. The trajectory of these electrons is modified via the spin-orbit interaction which induces an electric field, E_{ISHE}, transverse to J_S and the spin polarisation vector σ of the spin current [42] and is described by

$$E_{ISHE} \propto J_S \times \sigma. \tag{1.1}$$

Thus a spin current is converted to charge via the ISHE in the conducting polymer and can be detected across two gold electrodes [40]. In the case of spin pumping into the semiconducting polymer, a voltage is induced in a platinum spin sink layer via the ISHE in the platinum [41]. Until recently, the Hanle effect, which describes the precession of injected spins about an external magnetic field, had been absent from organic materials, which has been a major concern for the organic spintronics community because it is a good test of spin injection [43]. Although spin injection had previously

been detected in Alq_3 via muon spin spectroscopy [44], there had been a drive to actually measure the Hanle effect in organics. Hanle precession has now been measured in a semiconducting conjugated polymer by spin pumping into the polymer via FMR and angular measurements of the voltage detected as a result of the ISHE [41]. Detection of spin pumping into C_{60} via the ISHE is yet to be realised in this research or in the literature to date. The focus of our research has been to use a combination of FMR, spectroscopy and transport to determine whether we are truly injecting a spin polarised current into C_{60} when it is adjacent to a ferromagnetic material at FMR.

1.1 Thesis Layout

Throughout this thesis the interplay between C_{60} and ferromagnetic materials has been studied using a variety of techniques. To date, the rich spectroscopic molecular properties of organic materials remain underused in spintronics in comparison to their inorganic counterparts [45]. This thesis seeks to establish the first principles of manipulating molecular properties, in particular vibrational modes of C_{60}, using spin pumping and phonon injection from a ferromagnetic material at FMR. The spectroscopic and electronic properties of C_{60} can be utilised in multifunctional structures with potential in spin dependent optoelectronics as well as THz spintronics. The vibrational modes of the C_{60} are in the THz frequency region and are shifted in frequency, broadened and split when adjacent to a ferromagnet at resonance. The photoemission and conductivity of C_{60} is enhanced by a few percent as a result of the energy dissipated into the C_{60} from an adjacent ferromagnetic layer at resonance.

Chapter 2 covers the basic concepts of spintronics and introduces organic spintronics with a review of some of the relevant literature. Superconductivity is introduced in terms of an experimental technique known as point contact Andreev reflection, as a means to measure the spin polarisation. The theory behind magnetisation dynamics, FMR and spin pumping in organic materials has been discussed in depth using relevant literature.

Key experimental techniques used throughout this research are covered in Chapter 3. The more novel techniques in this research include the deposition of hybrid-organic

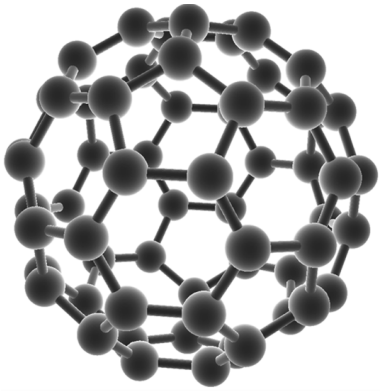

Figure 1.1: *A C_{60} molecule composed of of 60 carbon atoms at each vertex of 20 hexagons and 12 pentagons. Plotted using Virtual Nanolab.*

spin valves via thermal sublimation and sputter deposition. In addition to this I set up an adaptable FMR system that can be used simultaneously with electron transport, Raman spectroscopy and photoluminescence measurements. Other important techniques in this work include low temperature transport measurements, a variety of magnetometry including vibrating sample magnetometry (VSM), magneto-optical Kerr effect (MOKE) and Kerr microscopy. Transmission electron microscopy (TEM) and x-ray reflectivity (XRR) were used to characterise the sample structure and determine the thickness and roughness of thin films. I spent a month working at NanoGune in San Sebastian (Spain) where I made hybrid C_{60} based spin valves using thermal sublimation and electron beam evaporation, so this deposition system is described.

Results on hybrid magneto-C_{60} interfaces are presented in chapter 4. Here bilayer and multilayer samples of C_{60}/Co thin films are studied in terms of magnetic properties and structure. It is shown that C_{60} in contact with Co becomes doped with spin polarised electrons, reducing the magnetisation of the Co and inducing a magnetisation in C_{60} [46]. We investigated the use of C_{60} as an underlayer for exchange biased spin valve devices and showed that the exchange bias is enhanced in comparison to devices with a Ta underlayer [47]. Multilayer C_{60}/Co samples were characterised via transmission electron microscopy and x-ray reflectivity to determine whether sputter deposition of metals on C_{60} is a suitable technique. These measurements are compared to multilayers where the metals were electron beam evaporated during my secondment

in NanoGune.

Chapter 5 is a discussion of the work carried out to improve C_{60} based spin valve devices. Firstly the optimisation of the insulating barrier in magnetic tunnel junctions is presented. The magneto-transport measurements across C_{60} spin valves made in Leeds and NanoGune are compared to show sputter deposition and electron beam evaporation are suitable for the deposition of metal layers on C_{60} in these devices. Some of the C_{60} based spin valves made in Leeds show asymmetries in resistance that can only be explained by hybridisation of the C_{60} to a ferromagnetic layer [34]. Some research to elucidate the role of the Al_2O_3 layer is presented here as well as direct measurements of the spin polarisation of a ferromagnetic material in contact with C_{60} via point contact Andreev reflection [34].

FMR measurements on C_{60}/ferromagnetic bilayers were carried out as shown in chapter 6. Changes in effective magnetisation and changes in damping of the ferromagnet with/without C_{60} can be determined from such measurements. The changes in effective magnetisation can be correlated to results presented in chapters 4 and 5. The change in damping leads to a further understanding of the spin pumping mechanism from a ferromagnetic material into an organic semiconductor. C_{60}/YIG bilayers were also measured via FMR because one would expect to observe spin pumping but an absence of charge transfer owing to the insulating properties of YIG [48].

In chapter 7 results using a combination of techniques to utilise the damping mechanism of a ferromagnetic material at FMR are presented. These measurements were used to detect evidence of spin doping, spin pumping and phonon injection in the C_{60}. Simultaneous electron transport-FMR measurements are presented across a film of C_{60} adjacent to a ferromagnetic electrode at resonance to observe the conductivity. Results probing the vibrational modes of C_{60} during FMR via Raman spectroscopy are presented and compared to the vibrational modes during heating or spin injection [49]. Finally, simultaneous FMR-photoluminescence measurements are discussed to determine the changes to the optical properties of C_{60} and whether there is evidence of phonon injection.

CHAPTER 2

Theoretical background

In order to investigate and improve on organic spintronic devices, a thorough understanding of conventional spintronics is required. The basic concepts in spintronics and some historical insight into the topic will be discussed in this chapter. Throughout this research thin films are studied in order to observe physical effects not found in bulk materials, for instance exchange-bias in ferromagnetic/antiferromagnetic bilayer films and tunnelling magnetoresistance (TMR). The concepts involved in superconductivity will be reviewed in terms of an experimental method to measure the spin polarisation in a thin film via point contact Andreev reflection (PCAR). Raman scattering theory will be discussed because this spectroscopic technique is used throughout this work to investigate the molecular vibrations of C_{60}. Molecular electronics and organic spintronics will be introduced in the latter part of this chapter with a review of key results in the field that are relevant to this work as well as the motivation behind using C_{60}. Magnetisation dynamics plays a vital role in magnetic devices and is key to unlock new paradigms in both conventional spintronics and organic spintronics. Thus this chapter will also cover the basic principles of magnetisation dynamics as well as a brief literature review on spin pumping in organic materials.

2.1 Spintronics

2.1.1 Tunnel magnetoresistance

If two ferromagnetic layers are separated by an ultra-thin insulating barrier then the electrons have a finite probability of quantum tunnelling through the barrier. The electrical resistance through this insulating barrier is dependent on the relative orientation of magnetisation of the ferromagnetic layers; this effect is known as tunnel magnetoresistance (TMR). When the ferromagnetic layers are aligned, the conductivity is higher compared to when the ferromagnetic layers are aligned antiparallel to each other [50]. The TMR effect was first observed at 4.2 K in Fe/GeO/Co junctions in 1975 by Julliere [51]. TMR can be utilised in sensor devices known as magnetic tunnel junctions (MTJs).

In order to simplify the concept of magnetoresistance (MR), resistors of high and low resistivity in series and parallel can be used as shown in figure 2.1[52]. Here the

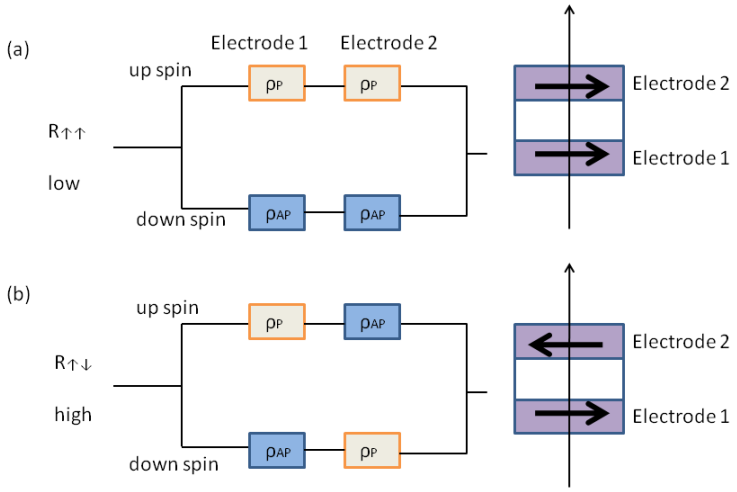

Figure 2.1: *Diagram showing resistors in series and parallel to represent a device with current travelling perpendicular to the plane (a) when the resistance is low because the magnetisation of the electrodes are parallel (P) to each other and (b) when the resistance is high because the magnetisation of the electrodes are antiparallel (AP) to each other. Here ρ represents the resistivity where ρ_{AP} is greater than ρ_P so the total resistance in case (b) is greater than in case (a).*

overall resistance is low when the low resistors are in series, analogous to weak scattering for electrons parallel to the magnetisation. The scattering probability for up spin and down spin electrons differs, which can be related to the density of states at the Fermi level which is split for ferromagnetic materials. In figure 2.1a the conduction is dominated by the spin up electrons because weak scattering occurs when the spin of the electrons are parallel to the magnetisation, resulting in a lower resistance. Figure 2.1b shows an overall high resistance as a result of strong scattering for the up spin electrons in one layer of the device and down spin electrons in the other representing an antiparallel magnetic orientation of electrodes [52].

An insulating barrier regularly used in the fabrication of MTJs is Al_2O_3. It is beneficial for this purpose because high TMR values can be observed and it is relatively easy to make barriers without pinholes [50; 53]. Mott's two current model can be used to describe the tunnelling current of each direction of spin as shown in figure 2.1 and figure 2.2. Here the tunnelling current is proportional to the product of the

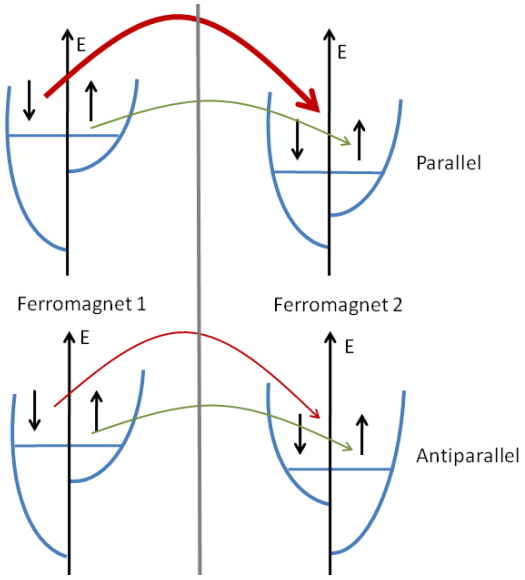

Figure 2.2: *Illustration of the density of states and transport of majority and minority spins. The thickness of the arrows represent the amount of spin current moving from the one electrode to the other.*

density of states at the Fermi level in the ferromagnetic layer at either side of the tunnel barrier. Figure 2.2 represents the spin current (J) moving between the electrodes in different relative orientations. The current when the ferromagnetic electrodes are parallel J^P and antiparallel J^{AP} to each other respectively can be described by the following equations [54]:

$$J^P \propto N_1^{\uparrow} N_2^{\uparrow} + N_1^{\downarrow} N_2^{\downarrow}, \tag{2.1}$$

$$J^{AP} \propto N_1^{\uparrow} N_2^{\downarrow} + N_1^{\downarrow} N_2^{\uparrow}, \tag{2.2}$$

where N_1 and N_2 refer to the density of states at the Fermi level for the top and bottom electrodes respectively where the arrow superscript represents up or down spin. TMR is a ratio of the change in resistance, *R*, between the parallel, *P*, and antiparallel, *AP*, alignments of the electrode compared to the resistance in parallel orientation [54] and can be written as

$$TMR = \frac{R_{AP} - R_P}{R_P}. \tag{2.3}$$

The spin polarisation (P) is normally based on the measure of ratio of the density of

states of the up and down spin electrons as described by

$$P = \frac{N^{\uparrow}(E_F) - N^{\downarrow}(E_F)}{N^{\uparrow}(E_F) + N^{\downarrow}(E_F)}. \tag{2.4}$$

For tunnelling spin polarisation, equation 2.4 would be weighted by a spin dependent tunnelling matrix. Ferromagnetic materials have a non-zero spin polarisation resulting from exchange splitting of electronic states at the Fermi level (E_F). This means ferromagnetic materials have a majority and minority spin as shown in figure 2.2. The s-electrons dominate the tunnelling current because they are dispersive and decay slowly. However the d-electrons have a large effective mass and decay rapidly so they are not responsible for the tunnelling current.

A higher spin polarisation results in an increased TMR. Julliere assumed that the electrons of different spin move along separate channels and that the spin is conserved during tunnelling [51]. By combining equations 2.1,2.2 and 2.3 the spin polarisation can be related to the ratio of resistance in the parallel and antiparallel orientation as shown in the Julliere equation:

$$\frac{\Delta R}{R_{AP}} = \frac{2P_1P_2}{1 + P_1P_2}. \tag{2.5}$$

There is a finite probability that electrons tunnel across the insulating barrier. This probability decreases exponentially with increasing effective thickness because of the evanescent state of the electron wave. An applied bias voltage acts to reduce the effective thickness of the insulating barrier and therefore the tunnelling probability should increase at higher biases. Simmons introduced a model for the current-voltage (I-V) characteristics of a tunnel junction as shown in a simplified form as [55]

$$J = \beta(V + \gamma V^3), \tag{2.6}$$

where J is the current density, V is the voltage, and β and γ are related to the barrier height and width respectively as modelled by Simmons [55]. Figure 2.3 shows an example Simmons fit to I-V measurements through an Al_2O_3 tunnel junction. Here the non-linear I-V characteristics are apparent. However, there is an intrinsic systematic error in the Simmons model because it correlates barrier height and width with a square dependence. This model is too simple to describe the variable range hopping transport

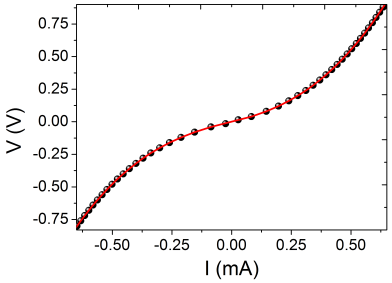

Figure 2.3: *Example I-V characteristics for an Al_2O_3 based tunnel junction fitted with the Simmons equation (red line).*

through C_{60} junctions as discussed in section 2.5.

In order to determine if a device is exhibiting tunnelling characteristics there are some criteria to be met; these are known as the Rowell criteria [56]. Firstly the resistance-area (RA) product of the device should depend exponentially on the barrier thickness. The RA product is simply the product of the saturation resistance of the device and the area of the junction. The I-V measurements should be non-linear and fit to a tunnelling model. The resistance should also be inversely dependent on the temperature. These criteria will be used in chapter 5 to show the transport regime through hybrid C_{60} spin valves is tunnelling or hopping like.

2.1.2 Exchange biased spin valves

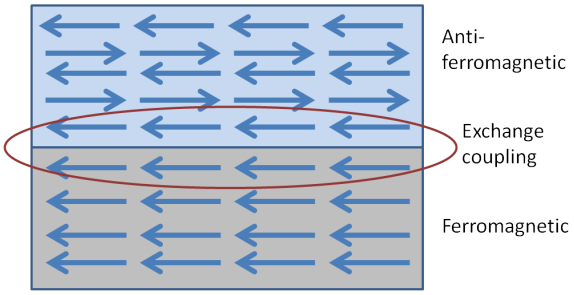

Figure 2.4: *Schematic of an exchange biased system. Here an antiferromagnetic material is adjacent to a ferromagnetic material. The magnetisation direction of the ferromagnetic and antiferromagnetic sample align at the interface.*

A ferromagnetic layer can be pinned in a particular orientation using an antiferromagnetic material to exchange couple to the ferromagnetic layer at the interface [57]. This results from the exchange anisotropy at the interface between the ferromagnet and antiferromagnet. When an antiferromagnetic film is deposited on top of a ferromagnetic film the antiferromagnetic spins at the interface align to the ferromagnetic spins as shown in figure 2.4. The rest of the antiferromagnetic layer then follows this order in alternate layers, so that the net magnetisation is zero in the antiferromagnet. The antiferromagnetic spins at the interface exert a microscopic torque on the ferromagnetic spins to keep them in the original position. This means a greater field is required in order to reverse the orientation of the ferromagnetic spins [58]. The larger field required to switch the spins results in a hysteresis loop shifted away from zero field as shown in figure 2.5a.

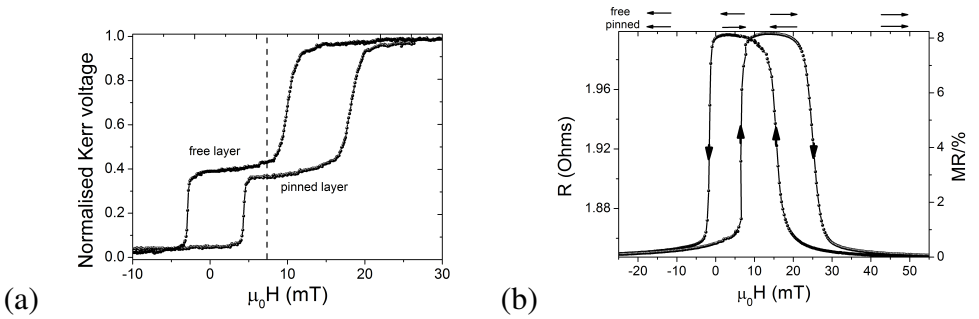

Figure 2.5: *(a) Typical magneto-optical Kerr effect (MOKE) measurement on a copper based spin valve (refer to section 3.2.4). The hysteresis loops corresponding to the free and pinned ferromagnetic layers are labelled. (b) Typical MR measurement on a copper based spin valve carried out using a room temperature magneto-transport rig. The arrows represent the relative orientation of the free and pinned ferromagnetic layers.*

Figure 2.5a shows a typical MOKE (magneto-optical Kerr effect) (refer to section 3.2.4) measurement on a copper based spin valve with the structure Ta/Co/Cu/Co/IrMn/Ta. Two hysteresis loops are observed because the magnetic moments of the free layer switch at lower fields than the pinned layer. This is known as an exchanged bias system. The antiferromagnetic material used in this research to pin one of the ferromagnetic layers is iridium manganese (IrMn). The relative orientation of ferromagnetic layers separated by a non-magnetic spacer can therefore be controlled by an external

magnetic field. The resistance across a device can be measured as the magnetic field is varied using a four point contact measurement to eliminate resistance contributions from the electrodes and leads. Figure 2.5b shows a typical MR measurement on a spin valve. The arrows represent the relative orientation of the free and pinned electrodes as the field is swept.

2.2 Point contact Andreev reflection

A thorough discussion and explanation of superconductivity is beyond the scope of this thesis, however this section will cover some of the basic theory and go into some depth of Andreev reflection and the modified Blonder-Tinkham-Klapwijk (BTK) theory [59; 60]. This introduction into the subject is required to understand point contact Andreev reflection (PCAR), a technique which can be used to measure the spin polarisation of metals by the limitation of Cooper pair formation as a current is passed at a metal/superconducting point contact interface. PCAR has been used to measure the spin polarisation of a range of different thin film materials.

In 1998 two groups introduced the PCAR technique in different ways, one by using a superconducting tip in contact with a metal sample, and the other through nanocontacts between a metal and superconductor [61; 62]. Despite the techniques differing, the concept is the same, studying the variation of the conductance through a point contact at a ferromagnetic-superconducting interface to determine the spin polarisation.

A charge carrier incident at an interface between a metal and superconductor can propagate into the superconductor in one of two ways. Firstly if the charge carrier has energy greater than the superconducting energy gap, Δ, of the superconductor then it can propagate into the superconductor as a quasiparticle. However if the charge carrier has energy smaller than that of the Δ then there are no quasiparticle states available [63]. This means the charge carrier must convert to a supercurrent by pairing with a charge carrier of opposite spin. To do this Andreev reflection must occur, which involves the reflection of a hole back into the metal [59]. For a normal metal/superconducting interface, the conductance measured at voltage bias below that of the Δ will have double the conductance compared to biases above the Δ of the

superconductor. Thus, the typical conductance with voltage bias for a normal metal-superconducting point contact reveals a double conductance in the superconducting state (G_{NN}) compared to that in the normal state ($G(V = 0)$), for instance if P=0 in equation 2.7. The relationship between conductance and spin polarisation can be written as

$$\frac{G\,(V=0)}{G_{NN}} = 2\,(1-P)\,, \tag{2.7}$$

where P is the spin polarisation from the ratio of the density of states weighted by the spin dependent Fermi velocities v_f:

$$P = \frac{N\uparrow v_f\uparrow - N\downarrow v_f\downarrow}{N\uparrow v_f\uparrow + N\downarrow v_f\downarrow} \tag{2.8}$$

The idea of using the formation of Cooper pairs to measure the spin polarisation of a material was introduced by de Jong et al [64]. Andreev reflection or the formation of Cooper pairs would be limited for a spin polarised-superconducting interface because at the Fermi level there is a lack of available minority carriers [59]. For instance not every up spin charge carrier would have an available down spin charge carrier it could pair with. Assuming a perfect contact, the spin polarisation could simply be extracted by the comparison between the zero bias conductance and the conductance above the Δ (in the normal state). However, the conductance at lower biases is normally affected by some form of tunnel barrier at the interface. Thus in order to extract the spin polarisation from this technique one must use a more complicated analysis to take into account not only scattering and the barrier parameter but also the smearing parameter.

The unmodified BTK theory describes scattering at the interface between a normal metal and a superconductor, whereas the modified BTK theory has been changed to take into account a ferromagnetic material instead of a normal metal [60]. Figure 2.6 shows a depiction of the density of states and process of Andreev reflection comparing the interface between a superconductor and normal metal, and a superconductor and 100 % spin polarised ferromagnetic material [61].

The model used in this research to describe the conductance at a superconducting-ferromagnetic point contact is given in equation 2.9. In this model the conductance is assumed to be the sum of the conductance at a non-magnetic-superconducting interface

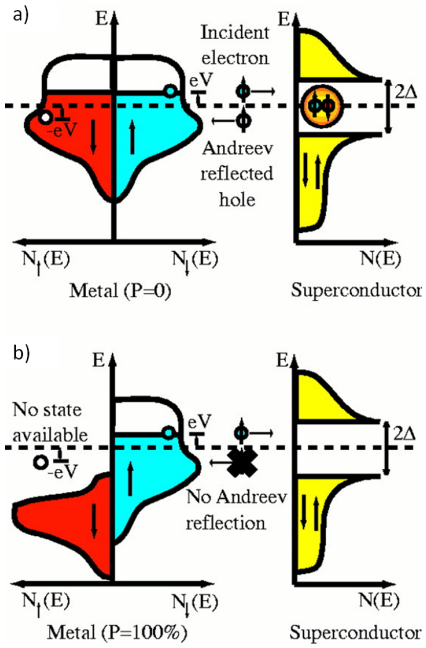

Figure 2.6: *Depiction of (a) normal-metal-superconducting interface and (b) 100% spin polarised ferromagnetic-superconducting interface. Taken from [61].*

and a 100 % spin polarised-superconducting interface. In the latter the Cooper pair formation or Andreev reflection is completely quenched. The conductance can be described by

$$\frac{\partial I}{\partial V}_{Total} = (1-P)\left(\frac{\partial I}{\partial V}_{unpol}\right) + P\left(\frac{\partial I}{\partial V}_{100\%spinpol}\right), \tag{2.9}$$

$$\beta = \frac{V}{\sqrt{|\Delta^2 - V^2|}}, \tag{2.10}$$

where V depicts the voltage bias across the point contact and the partial differential

Table 2.1: Differential conductance terms for different transport regimes and different spin polarisations [65].

BTK	E< Δ	E> Δ
$\frac{\partial I}{\partial V}_{unpol}$	$\frac{2\left(1+\beta^2\right)}{\beta^2+(1+2Z^2)^2}$	$\frac{2\beta}{1+\beta+2Z^2}$
$\frac{\partial I}{\partial V}_{100\%spinpol}$	0	$\frac{4\beta}{(1+\beta)^2+4Z^2}$

conductances given in table 2.1 were derived and introduced by Blonder, Tinkham and Klapwijk (BTK) [60]. In this model Z is the interfacial barrier parameter which is dimensionless and takes into account tunnelling resulting from an oxide layer at the interface. In addition to these parameters, the effects of measuring at a finite temperature and other scattering events must be included in the model. This parameter is known as the smearing parameter, which can be related to the temperature of the system, where a Gaussian function with a defined width of ω can be convoluted with the conductance data. Thus, the parameters V, Δ, ω and Z can be extracted from fitting experimental PCAR conductance data.

2.3 Raman scattering theory

Raman spectroscopy utilises the inelastic scattering of monochromatic light, named after Raman who discovered the phenomena in 1928 [66]. Typically a monochromatic source is incident on a sample and photons are scattered. Most of the photons are elastically scattered which is known as Rayleigh scattering. However some are inelastically scattered and the frequency of the resulting photons are shifted; this is known as the Raman effect. Figure 2.7 shows the possible types of elastic and inelastic collisions of photons: elastic Rayleigh scattering, inelastic Stokes and anti-Stokes scattering. The change in frequency is dependent on the transitions or modes, such as vibrational or rotational modes, of the sample.

When an electric field $\bar{E}$ is incident on a sample, a dipole moment is induced, P. The polarisability α is dependent on the molecular structure and the bonds of the material [67]. This can be written as

$$P = \alpha \bar{E}. \tag{2.11}$$

The electric field $\bar{E}$ is time dependent and is a function of the frequency of the incident electromagnetic wave ν_0 where

$$\bar{E} = E_0 \cos(2\pi\nu_0 t). \tag{2.12}$$

Thus the strength of the induced dipole moment can be expressed as

$$P = \alpha E_0 \cos(2\pi\nu_0 t). \tag{2.13}$$

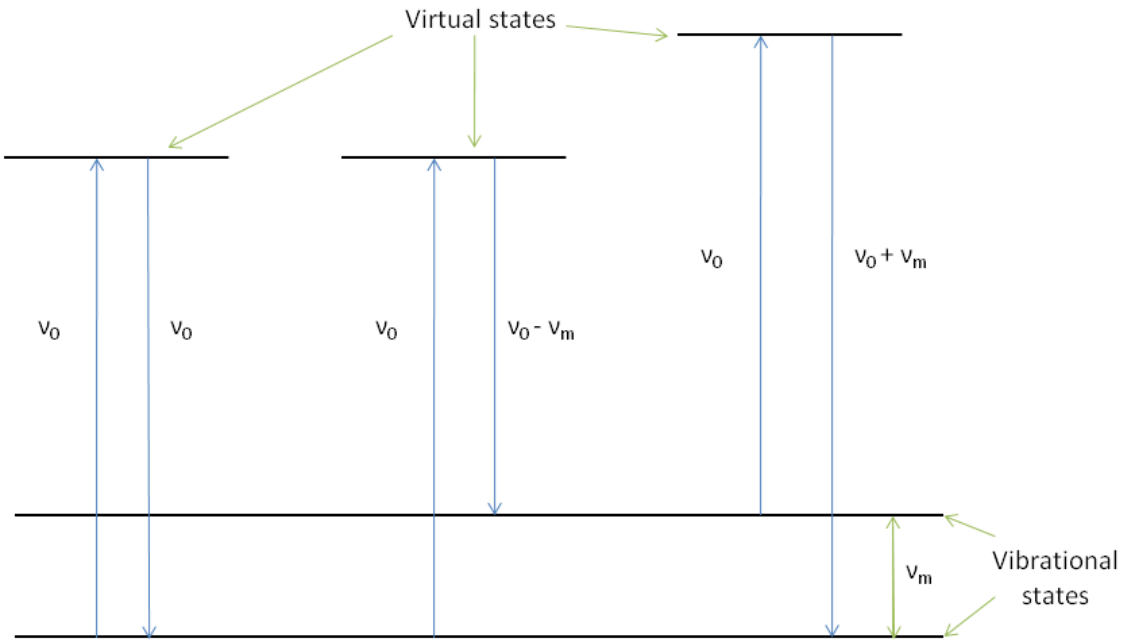

Figure 2.7: *Diagram representing the transitions of photons in Raman spectroscopy. When the frequency of the scattered photon is the same as the incident photon this is known as Rayleigh scattering. The Raman effect is when the frequency of the scattered photon is shifted from the incident frequency; this is known as Stokes and Anti-Stokes for frequencies shifted up or down respectively.*

For a given molecular bond, the atoms have allowed vibrational modes to which they are confined. These vibrational modes are quantised and the energy of a particular vibrational mode, E_{vib}, can be written as

$$E_{vib} = (j + 1/2)h\nu_{vib}, \tag{2.14}$$

where *j* is the vibrational quantum number and ν_{vib} is the frequency of a vibrational mode. The polarisability is related to the instantaneous position of atoms because the perturbation of electrons by an electric field depends on the relative location of atoms in the molecular structure. The physical displacement from equilibrium due to a vibrational mode dQ can be related to the maximum displacement Q_0 by

$$dQ = Q_0 \cos(2\pi\nu_0 t). \tag{2.15}$$

A Taylor series expansion can be used to describe the polarisability for small displacements, where

$$\alpha = \alpha_0 + \frac{\partial \alpha}{\partial Q} dQ. \tag{2.16}$$

The polarisability can be related to the physical displacement by combining the previous equations:

$$\alpha = \alpha_0 + \frac{\partial \alpha}{\partial Q} Q_0 \cos(2\pi \nu_{vib} t), \tag{2.17}$$

$$P = \alpha_0 E_0 \cos(2\pi \nu_0 t) + \frac{\partial \alpha}{\partial Q} Q_0 E_0 \cos(2\pi \nu_0 t) \cos(2\pi \nu_{vib} t). \tag{2.18}$$

The strength of the dipole moment can be separated into three terms which describe Rayleigh, Stokes and anti-Stokes scattering as shown in

$$P = \alpha_0 E_0 \cos(2\pi \nu_0 t) + \left(\frac{\partial \alpha}{\partial Q} \frac{Q_0 E_0}{2} \right) \left\{ \cos(2\pi(\nu_0 - \nu_{vib})t) + \cos(2\pi(\nu_0 + \nu_{vib})t) \right\}, \tag{2.19}$$

by the first, second and third term respectively.

2.4 C_{60} buckyballs

Carbon can form three types of orbital hybridisations: sp^3, sp^2 and sp^1, thus a range of crystalline and disordered structures of carbon exist. These hybridisations can lead to a huge variation in the properties of the allotrope, such as band structure and density [68; 69]. A single carbon atom in its ground state has six electrons in the configuration $1s^2$, $2s^2$ and $2p^2$. To lower the total energy in a carbon system the s and p states in the valence shell hybridise when forming molecular bonds. Figure 2.8 shows how these sp^3, sp^2 and sp^1 states form, where the weak π bonds and strong σ bonds are represented by shaded and unshaded regions respectively. When the electrons in the $2s^2$ and $2p^2$ orbitals hybridise with each other, as shown in the sp^3 configuration in figure 2.8, tetrahedrally directed orbitals are formed, thus forming strong sigma bonds between the four nearest neighbours, leading to the structure of diamond as shown in figure 2.9.

The sp^2 configuration is responsible for a number of structures, including graphene, carbon nanotubes and C_{60}. One can imagine cutting up graphene and folding it to form

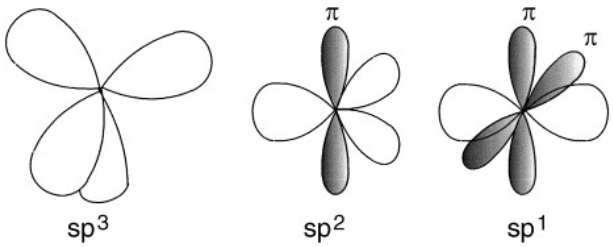

Figure 2.8: *Bonding in carbon showing the different hybridisations of orbitals taken from [68].*

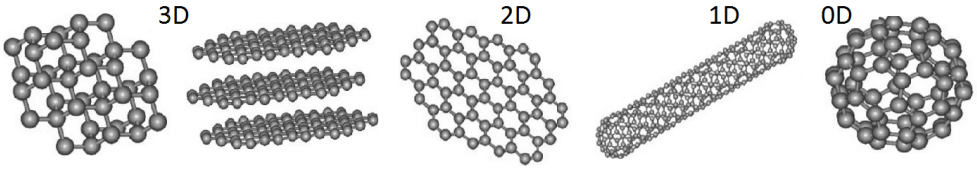

Figure 2.9: *Allotropes of carbon from left to right: 3D diamond lattice, 3D graphite, 2D graphene, 1D single wall carbon nanotube, 0D C_{60} or buckminsterfullerene or buckyball. Adapted from [70].*

carbon nanotubes or C_{60}, as can be visualised using figure 2.9. The sp^2 configuration, as shown in figure 2.8 is formed when there is a hybridisation between the 2s orbital and the 2px and 2py orbitals. This leads to strong covalent 120° bonds between three adjacent atoms in the same plane. A weak π bond is formed between adjacent atoms because the pz orbital sits perpendicular to the plane. In this sort of structure the π bonds are delocalised and are thus responsible for conduction of electrons through such a structure. However, the σ bonds are localised and therefore not responsible for conduction of electrons. The bonding in C_{60} is more complex than purely being sp^2, because the sp^2 orbitals do not all lie in the same plane. Thus the hybridisation can only be approximated to sp^2 but is in fact somewhere between the sp^2 and sp^3 configurations.

C_{60} is also known as buckminsterfullerene or buckyballs because of the resemblance of the molecule to famous geodesic domes designed by Buckminster Fuller. C_{60} was discovered by Harold Kroto, Robert Curl and Richard Smalley in 1985, for which Kroto won the Nobel prize in Chemistry for this discovery [17]. It was discovered when they were studying carbon plasmas through the laser evaporation of graphite

Table 2.2: Properties of C_{60} [71].

Property	Value
crystal structure	FCC
density (g/cm^3)	1.65
lattice constant (Å)	14.5
C-C length (Å)	1.455
C=C length (Å)	1.391
sublimation temperature (K)	800
index of refraction	2.2
conductivity	n-type semiconductor
resistivity (Ωm)	1 x 10^{14} room temperature
naturally occurring deposit	shungite
C_{60}-C_{60} nearest approach (Å)	3.1
relative periativity	4.4
electron affinity (eV)	2.6
Ionisation potentials (eV)	
C_{60} to C_{60}+	7.6$\pm$0.2
C_{60}+ to C_{60}2+	12.3$\pm$0.5
C_{60}2+ to C_{60}3+	17$\pm$0.7
C_{60}3+ to C_{60}4+	21.7

[17]. They were developing a method to study the conditions in interstellar clouds and the conditions that carbon experiences in such an environment. From the stabilisation of the benzene chains, fullerenes were formed where the most stable and therefore most abundant were C_{60} and C_{70}. When C_{60} is doped with alkali metals it has been shown to be superconducting to a higher temperature compared to any other organic superconductor [72]. As shown in figure 1.1, the C_{60} molecule is made up of 20 hexagons and 12 pentagons with a carbon atom at each vertex [73]. C_{60} is particularly interesting in thin film form and has been shown to exhibit n-type semiconducting behaviour [74]. The properties of C_{60} (some of which are listed in table 2.2) are very dependent on growth, purity and oxidation defects so optimising and determining these aspects is important. Various techniques have been used in the study and characterisation of

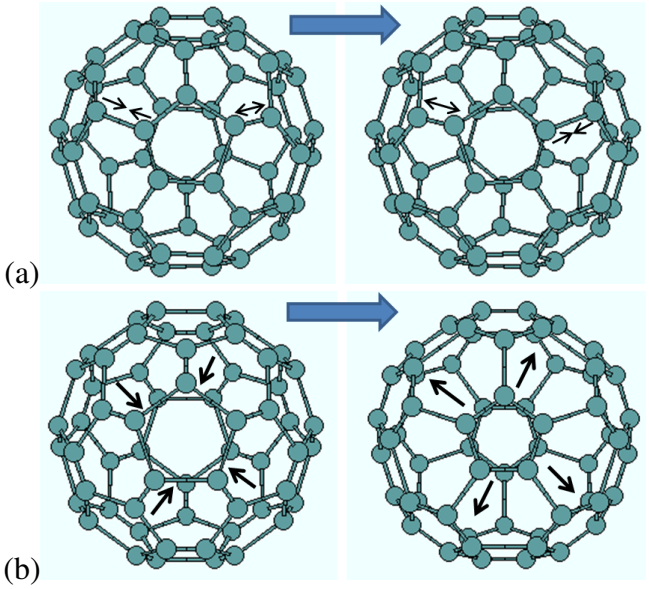

Figure 2.10: *(a) Diagram of Hg(7) mode. (b) Diagram of Ag(2) mode. Adapted from reference [75].*

C_{60}, including electrical conductivity, photoconductivity and optical absorption [74]. C_{60} molecules can be grown by sublimation under high vacuum conditions and can withstand the deposition of metals [18].

Phonons are quasiparticles that are quantised vibrations of a crystal lattice. In a crystal there can be 3N phonon branches, where N is the number of atoms in one unit cell [76]. Thus for C_{60} there can be 180 degrees of freedom, 3 of which are translational, 3 rotational and 174 vibrational. These C_{60} vibrations are related to the structure and symmetry of the C_{60} molecules. Due to the high symmetry of the C_{60}, a lot of the vibrational modes are degenerate in frequency, leaving 46 distinct frequencies, in theory. It is well known in solid C_{60} that the 240-1600 cm^{-1} vibrational spectrum are intramolecular interactions, whereas the 0-65 cm^{-1} vibrational spectrum are the intermolecular interactions [76]. C_{60} has 10 Raman active vibrational modes as given in table 2.3. A schematic representation of two of these Raman active vibrational modes is given in figure 2.10 showing the Hg(7) breathing mode in (a) and the Ag(2) pinching mode in (b).

Table 2.3: Raman active vibrational modes of C_{60}

Vibrational mode	Degeneracy	Wavenumber (cm^{-1})
Hg(1)	5	272
Hg(2)	5	433
Ag(1)	1	496
Hg(3)	5	709
Hg(4)	5	772
Hg(5)	5	1099
Hg(6)	5	1252
Hg(7)	5	1425
Ag(2)	1	1471
Hg(8)	5	1575

In terms of spintronics, C_{60} molecules are desirable as they are relatively light and also do not contain hydrogen, therefore they possess a weak hyperfine interaction and weak spin orbit interaction. As a result of these weak interactions, the spin lifetime and spin diffusion lengths are exceptionally long (on the order of 100 nm)[3]. The molecular vibrations of C_{60} are affected by the presence of charge or spin polarised electrons [49]. Therefore, we are interested in measuring such vibrations using Raman spectroscopy.

2.5 Hopping transport

If electrons are not able to travel through a material as a continuum then they need to tunnel from one atomic site to another. For hopping transport in a strongly disordered system, the charge carriers are localised and they hop between different atomic sites. In order for the charge carriers to hop they must overcome an energy barrier. As a result of this activation energy required, the conductivity σ is dependent on the temperature T for a d dimensional system and can be written as

$$\sigma = e^{-b/T^{1/(d+1)}}, \tag{2.20}$$

where b is related to disorder. This hopping process is dependent on thermal activation so the overall conductance of materials that exhibit hopping is smaller than the con-

ductance of metals [77]. For low temperatures the hopping is not most likely to occur between nearest neighbours. The electrons can hop further to reach a lower energy state. The probability P for a charge carrier to hop a distance R is given by

$$P = e^{-2\alpha R} e^{-\Delta E/k_B T}, \tag{2.21}$$

where $1/\alpha$ is the decay length of the localised wave. The probability of hopping is not maximised for nearest neighbours but for R, given by

$$R = (8\pi N(E)\alpha k_B T)^{-1/4}, \tag{2.22}$$

where N(E) is the density of states [77]. For C_{60} films, the electrons tunnel between localised states on a molecule by a phonon-assisted variable range hopping mechanism. Energy is required to overcome a barrier and such hopping events can be assisted by vibrons (molecular vibrations) [78]. Inelastic scattering between electrons and phonons gives the localised electrons enough energy to overcome the barrier. Therefore as the temperature is reduced, phonons in the lattice become frozen, giving the electrons less energy for hopping steps, and thus the resistance is increased. In a C_{60} crystal lattice the intermolecular interactions are weak Van der Waals interactions. Therefore the intramolecular vibrations dominate the phonon-assisted hopping mechanism [78].

2.6 Organic spintronic devices

Figure 2.11 shows how the spin dependent density of states of a molecule can be modified by coming into contact with an inorganic ferromagnetic interface. In order to achieve good spin injection into molecules these interfacial effects must be further understood. Barraud et al investigated the nature of spin injection into organic materials and found that it is very dependent on the chemical bonds at the interface [80]. It was proposed that these chemical bonds can be engineered in order to control spin injection into molecules. The spin polarisation is dependent on the density of states of the electrodes. At the organic/inorganic ferromagnetic interface there are hybrid electronic states which can act as spin filters. Barraud et al investigated nanocontacts in order to probe the organic/inorganic interface locally. They observed that locally the MR can be different and even an opposite sign depending on the interaction between the organic

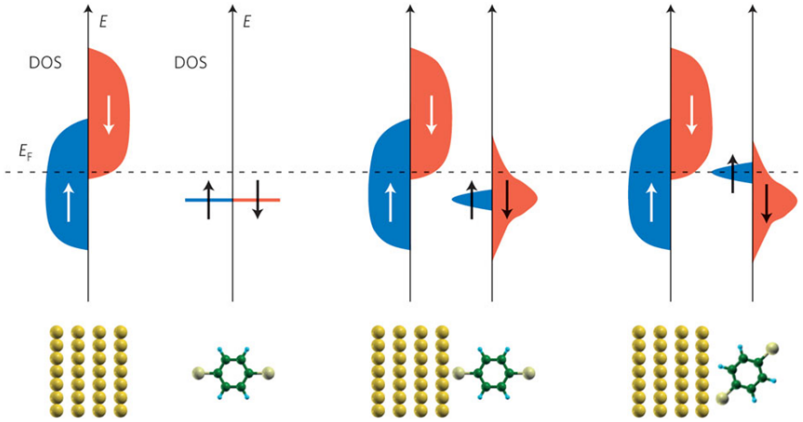

Figure 2.11: *Schematic diagram of the density of states (DOS) at the inorganic/organic interface showing the spin filtering mechanism as a molecule is (left) far away from the ferromagnetic material (middle) in contact with the ferromagnetic material (right) in contact with the ferromagnetic material in a different orientation [79].*

and ferromagnetic material. They found that there can be a few 'hot spots' where the spin polarised current density is high and this can change the overall MR in the device where the organic layer here is the active spacer layer.

To understand the interfacial effects it is important to think about the density of states for the organic and inorganic ferromagnetic material. The ferromagnetic density of states is broad and the spins are split in energy into majority and minority sub-bands as shown in figure 2.11a [79]. The organic material is made up of discrete molecular energy levels. Only the highest occupied molecular orbital (HOMO) is close enough to the Fermi energy of the ferromagnetic material in order to contribute to the current. If there is no interaction at the hybrid interface then the electronic structure is simply a superposition of the components from either material. However if the molecule is brought into contact with the ferromagnetic material, then the density of states is altered. This can happen in more than one way. Firstly, the molecular orbitals become finite because electrons leak in and out of the molecule which broadens the density of states. This broadening effect depends on the interaction at the interface and the proximity. There is an imbalance in energy for the up and down spin electrons in the ferromagnetic material so the molecular orbitals for up and down spin electrons broaden by

different amounts as shown in figure 2.11b. It can happen that a broadened molecular orbital can lead to opposite spin polarisation at the Fermi energy which carries most of the current, changing the nature of the MR in a device. The energy levels of the molecular orbital can also be shifted and this too can be spin dependent. Figure 2.11c shows an energy shift in the molecular orbitals and here the majority spin would dominate the current, however this can occur the other way round (thus changing the sign of MR). The strength of the interaction at the interface determines the spin-filtering effect [79].

One benefit of organic semiconductors in spintronics is the weak spin scattering mechanism allowing the spin polarisation of carriers to be maintained for longer times and larger length scales. This is a result of the low atomic number, Z, of carbon and therefore the weak spin-orbit interaction which is proportional to Z^4 [81]. The spin relaxation times in organic materials usually exceed that of metals and most semiconductors by orders of magnitude [82] because the electrons are transported through π delocalised orbitals [80]. The electronic properties of organic semiconductors vary from the typical semiconductors used in spintronic devices. The transport and spin injection in normal semiconductors can be described ballistically or as diffusive motion of carriers that are spin polarised. The spin flip in such materials is a result of the spin-orbit interaction. However, in the case of organic semiconductors the charge carriers hop incoherently between strongly localised states and propagate in this manner. The localised states can be thought of as very narrow bands at low temperatures. Hybrid organic spintronic devices have the potential to compete with and even replace the inorganic equivalents. For organic semiconductors the active conduction channels are the LUMO for n-type carriers and the HOMO for p-type carriers. The highest occupied molecular orbital and the lowest unoccupied molecular orbital are analogous to the valence band and conduction band in crystalline materials. The molecular orbitals are a superposition of the atomic orbitals. Rocha et al discussed the effect of the end groups of molecules at the interface and their effect on the spin polarisation [82]. Depending on the organic material, the spin transport can either be tunnelling-like or metallic-like. For metallic-like transport the carriers can hop between extended delocalised states over the molecule [82].

Dediu et al were the first to show evidence for spin polarised injection in an organic semiconductor [83]. They measured up to 30 % MR at room temperature in sexiothiophene with LSMO ($La_{0.7}Sr_{0.3}MnO_3$) electrodes. LSMO is a half-metal and thus has a high spin polarisation. There has been an increasing interest in Alq_3 (tris[8-hydroxyquionoline] aluminium) since Xiong et al measured a large inverse spin valve effect in 2004 [29]. Up to 300 % MR has been measured in Alq_3 based junctions with LSMO and Co electrodes [80]. Despite achieving such large percentages in MR the spin injection mechanism still remains elusive.

2.6.1 Spin injection

Two requirements of a good semiconducting based spintronic device are a long spin lifetime in the semiconducting material and efficient spin injection. Generally the spin lifetime in semiconductors is greater than in metals, so using a semiconductor as a spacer layer, the layer between two ferromagnetic electrodes in spin valves, could be beneficial. However, the problem of conductivity mismatch between the ferromagnetic material and the semiconducting material can be detrimental to devices. One method to overcome this is to introduce a spin dependent interface resistance at the interface between the ferromagnet and semiconductor. Including an insulating barrier showed that the spin polarisation of injected current is significant if the interface resistance is greater than a threshold resistance [84].

There has been disagreement in the literature as to why C_{60} spin valves require an interface resistance in the form of an Al_2O_3 layer to show MR. It has been proposed by Gobbi et al that the Al_2O_3 layer is present simply to facilitate the growth of smooth C_{60} [18]. They fabricate "leaky" Al_2O_3 layers so that electrons do not need to tunnel over this layer but can simply conduct through pinholes. They also propose that this layer prevents the C_{60} and Co from interacting which could be detrimental to the device. Alternatively, it was proposed by Lin et al that the Al_2O_3 is in fact present to prevent the loss of spin polarisation at the interface due to scattering [85]. The devices are biased so that the electrons move from the first ferromagnetic electrode and tunnel across the Al_2O_3 barrier, through the C_{60} and then to the second electrode [85]. Tran et al have successfully deposited C_{60} spin valves where the Al_2O_3 layer is not leaky and

they propose that the electrons tunnel through this layer directly into the C_{60} layer if it is thick enough or tunnels over both layers if it is thin enough [33].

2.6.2 Electron transport through C_{60} spin valves

In order to achieve efficient spin injection from a ferromagnetic material into any semiconducting material the problem of the conductivity mismatch must be overcome. This can be improved using a spin dependent barrier at the interface between the two materials where a diagram showing the relationship between the Fermi energy of the ferromagnetic materials to the HOMO and LUMO of the C_{60} molecules is given in figure 2.12. The Schottky barrier height is the difference between the Fermi energy of the ferromagnetic material and the valence band/HOMO of the semiconductor (assuming it is n-type semiconducting). The Schottky barrier height is preferably low so that it is not only thermally excited electrons that are able to overcome the barrier; this would not be desirable as these electrons have a reduced spin polarisation. One way of reducing this barrier height is to have a tunnel barrier such as Al_2O_3 to partially de-pin the Fermi energy of the ferromagnetic material and to provide spin dependent transport [86].

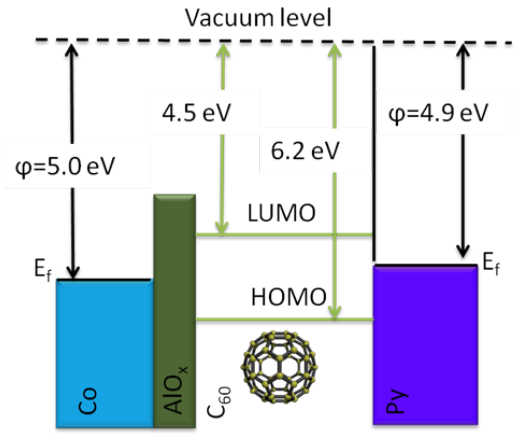

Figure 2.12: *Diagram of a HOMO, LUMO in a hybrid C_{60} junction. Figure based on reference [3] but made by Ms Fatma Al Ma'Mari.*

The mechanism behind spin polarised conduction through organic materials is

poorly understood. Tran et al present an experimental study where the spin behaviour of electrons through C_{60} spin valves in the diffusive regime is described using a multi-step tunnelling model [33]. They show that the MR decreases with the number of localised intermediate tunnel steps through the C_{60} layer despite the large value of spin lifetime in C_{60}. They propose that multi-step tunnelling in organic spin valves is analogous to the conductivity mismatch. They found that inhomogeneous magnetostatic fields as a result of interfacial roughness cause spin relaxation in the C_{60} layer. This process has been overlooked in previous studies of similar devices despite the fact that long spin lifetimes and large spin diffusion lengths in C_{60} would suggest the MR would be maintained with larger spacer layers of C_{60} [18; 85].

Tran et al proposed a model to describe spin polarised tunnelling via intermediate states through a composite Al_2O_3/C_{60} barrier [33]. Here they consider a two-step process where electrons have tunnel spin polarisation (TSP), p_0, as they leave the first ferromagnetic electrode (0) and tunnel into an intermediate state in the C_{60} (1) at a distance d from the Al_2O_3/C_{60} interface. Within the C_{60} layer the electrons have a time averaged occupation number for up and down spins respectively $n_\uparrow$, $n_\downarrow$. As the electrons enter the second ferromagnetic electrode they have TSP p_2. Back tunnelling processes were also considered, and a Fermi-Dirac distribution f(E_F) and a constant density of states for the ferromagnetic electrodes was assumed.

Equation 2.23 shows the dependence of the extinction coefficient of evanescent states through C_{60}, γ, on the effective mass of an electron, m_e, the barrier height, U, and the reduced Planck's constant, $\hbar$. In equations that follow κ represents the extinction coefficient through Al_2O_3. Both γ and κ can also be described by

$$\gamma = 2\sqrt{2m_eU}/\hbar. \tag{2.23}$$

$J_{01\uparrow P}$ is described by equation 2.24 and represents the tunnel current density flowing out of the first ferromagnetic electrode (0) into the intermediate state (1) at a distance d from the Al_2O_3/C_{60} interface when the ferromagnetic electrodes are aligned parallel.

$$J_{01\uparrow P} \propto \frac{1}{2}(1+p_0)(1-n_{\uparrow P})e^{-(\kappa d_A+\gamma d)}f(E_F) - \frac{1}{2}(1+p_0)n_{\uparrow P}e^{-(\kappa d_A+\gamma d)}(1-f(E_F)). \tag{2.24}$$

The forward tunnelling current is proportional to $(1 - n_{\uparrow P})$ and the back tunnelling current is proportional to $n_{\uparrow P}$. $1/2(1 + p_0)$ represents the fraction of the total current that consists of spin up electrons tunnelling out of the first ferromagnetic electrode (0) at the Fermi energy. d_A and d_C represent the thickness of the Al_2O_3 and C_{60} layers respectively. The transmission of electrons through the barrier scales with the extinction coefficients. $J_{12\uparrow P}$ represents the current density of electrons flowing out of the localised site in the C_{60} to the second ferromagnetic electrode and is described by

$$\begin{aligned} J_{12\uparrow P} \quad \propto \quad & \frac{1}{2}(1+p_2)n_{\uparrow P}e^{-(\gamma(d_c-d))}(1-f(E_F+eV)) \\ & -\frac{1}{2}(1+p_2)(1-n_{\uparrow P}e^{-(\gamma d_c-d)}f(E_F+eV)), \end{aligned}$$

where a bias voltage V is applied across the junction so that electrons tunnel from ferromagnetic electrode (0) to the intermediate state and then to ferromagnetic electrode (2). $J_{01\uparrow P} = J_{12\uparrow P} = J_{\uparrow P}$ under steady state conditions and therefore tunnel processes involving intermediate sites can be evaluated. The time averaged occupation number for spin up electrons while the ferromagnetic electrodes are aligned in a parallel orientation can be described by

$$n_{\uparrow P} = \frac{\frac{1}{4}(1+p_0)e^{-(\kappa d_A+\gamma d)} + \frac{1}{2}(1+p_2)e^{-\gamma(d_C-d)}f(E_F+eV)}{\frac{1}{2}(1+p_2)e^{-\gamma(d_C-d)} + \frac{1}{2}(1+p_0)e^{-(\kappa d_A+\gamma d)}}. \tag{2.25}$$

Expressions to describe the minority spin electrons can be obtained by relating $J_{01\downarrow P}$ to $n_{\downarrow}P$ and by replacing p_0 with $-p_0$ and p_2 with $-p_2$. To describe the current density in the antiparallel orientation, set $p_0 = -p_0$ without changing p_2. Therefore the TMR for tunnelling via an intermediate step distance d within the C_{60} layer can be described by

$$TMR(d) = (J_P - J_{AP})/J_{AP} = (J_{\uparrow P} + J_{\downarrow P} - J_{\uparrow AP} - J_{\downarrow AP})/(J_{\uparrow AP} + J_{\downarrow AP}). \tag{2.26}$$

2.7 Magnetisation dynamics

2.7.1 Ferromagnetic resonance

In this section the theory of ferromagnetic resonance will be introduced and the physics that describes this spin resonant behaviour such as the Kittel equation and Landau Lishfitz Gilbert equation will be explained.

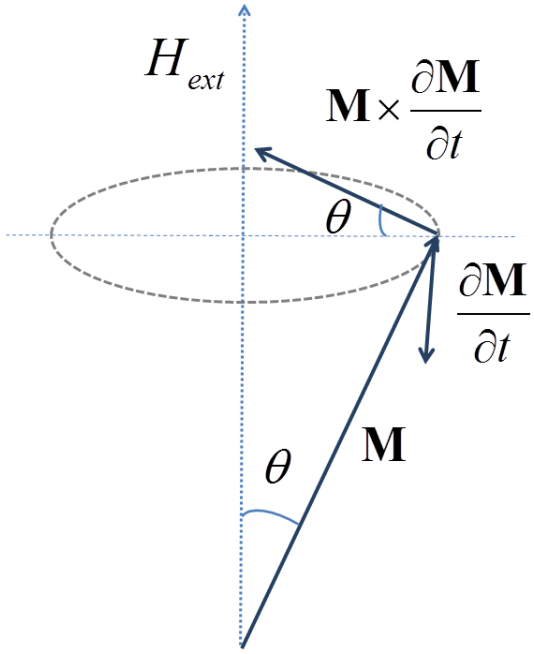

Figure 2.13: *Depiction of the precession of the magnetisation of a ferromagnet in an external magnetic field.*

There is a drive to increase the operational speed of devices, thus the understanding of magnetisation dynamics, particularly in the GHz range, is crucial. In this section, the basic theory behind the motion of magnetisation in an external magnetic field will be introduced. In 1935 Landau and Lifshitz introduced a model to describe the effect an effective magnetic field, H_{eff}, has on magnetisation [87]. The magnetisation dynamics can be described by

$$\frac{\partial M}{\partial t} = -\gamma \vec{M} \times \mu_0 \vec{H}_{eff}, \tag{2.27}$$

where γ is the gyromagnetic ratio, μ_0 is the permeability of free space, t is time and it is assumed the modulus of $\vec{M}$ (magnetisation) is constant in an applied magnetic field. This effective field exerts a torque on the magnetisation, causing the precession of the magnetisation about the effective magnetic field as shown in figure 2.13 at the Larmor frequency $\omega = \gamma\ \mu_0\ H_{eff}$. Without any damping, equation 2.27 does not accurately describe the reality of the magnetisation precession in a magnetic field; if this were the case, the magnetisation would never fully align to the magnetic field. A

phenomenological dissipation term, λ, was added to give

$$\frac{\partial M}{\partial t} = -\gamma \vec{M} \times \mu_0 \vec{H}_{eff} - \frac{\lambda}{M_s}\left[\vec{M} \times \left(\vec{M} \times \mu_0 \vec{H}_{eff}\right)\right]. \tag{2.28}$$

However, in 1955 Gilbert added a different damping term (the Gilbert damping parameter), α, which is similar to a viscous force. This damping parameter is perpendicular to the trajectory of the magnetisation and proportional to the time variation of the magnetisation. With this damping parameter included to take into account energy dissipation, the magnetisation precesses about the effective magnetic field at the Larmor frequency but also spirals inwards, reducing the cone angle, or angle of precession about the effective magnetic field. The LLG (Landau-Lifshitz-Gilbert) equation has been accepted to physically describe the precession and damping of a ferromagnetic system. This can be written as

$$\frac{\partial M}{\partial t} = -\gamma \vec{M} \times \mu_0 \vec{H}_{eff} + \frac{\alpha}{M_s}\left(\vec{M} \times \frac{\partial M}{\partial t}\right). \tag{2.29}$$

The Gilbert damping parameter α is intrinsic and in ultrathin films the mechanism of this damping is dominated by the relaxation of itinerant electrons. At finite temperatures spin waves scatter with electrons and phonons and can either conserve or flip the electron spin.

Ferromagnetic resonance techniques can be used to determine the damping parameter. If the magnetisation precession is excited by a pulse at the same frequency as the Larmor frequency then there is a strong absorption of power. These changes in power can be measured to determine the position in field/frequency of the resonances as well as the width, as discussed in section 3.2.7. One can measure the linewidth, ΔH, in magnetic field of the resonance peaks at different frequencies to extract the damping parameter. From this relationship and

$$\Delta H(f) = \Delta H(0) + \frac{\alpha f}{\gamma}, \tag{2.30}$$

one can extract α. *H(0)* is the extrapolated linewidth at zero frequency. The relationship between the resonant frequency, effective magnetic field and the effective magnetisation, M_{eff}, of a material can be described by the Kittel equation [88]:

$$f = \frac{\gamma}{2\pi}\left(H_{eff}\left(H_{eff} + \mu_0 M_{eff}\right)\right)^{1/2}. \tag{2.31}$$

It is apparent from equation 2.31 that as the magnetic field is increased, so is the resonant frequency because the cone angle of the magnetisation precession is reduced.

2.7.2 Spin pumping

A pure spin current may be driven into a metallic layer as a result of the magnetisation precession of a ferromagnet. In this process there is spin accumulation, which is the diffusion of excess spins into the metal. It decays on the same length scale as the spin diffusion length. There are two key mechanisms introduced in the literature for spin-pumping. Firstly, Berger et al introduced the idea of a spin accumulation resulting from spin flip scattering at the interface between a ferromagnetic material and a normal metal [89]. Secondly, Tserkovnyak et al suggested that [90] in the absence of a voltage bias or an electric field, the charge currents flowing across a ferromagnetic/metal interface are equal and opposite. Even though the current moving from the ferromagnet into the metal is spin polarised, there is no spin accumulation in the metal because of the back flow of spin polarised current, and spin relaxation in the metal balancing the spin current. However, the precession of the magnetisation of the ferromagnet causes an electron that has moved from the ferromagnet into the metal to experience a modified transmission on return to the ferromagnet. This is because the movement of the electron from the metal to the ferromagnet is dependent on the relative spin polarisation. Thus the back flow of spin polarised electrons is reduced and spin accumulation is enhanced.

2.7.3 Spin pumping into organics

Although there has been huge progress in organic spintronics over the past few years there has been little research into the effects of molecules on magnetisation dynamics or vice versa. As the need for speed in devices and recyclable technologies is ever increasing, spin pumping in organics may hold the answer to new technologies. Not only could we modify the magnetisation dynamics of the magnetic material but we also have the opportunity to manipulate molecular vibrations and discover the relationship between vibrational modes, spin pumping and phonon injection. To date, there has been little published with regards to spin pumping into organic materials and nothing

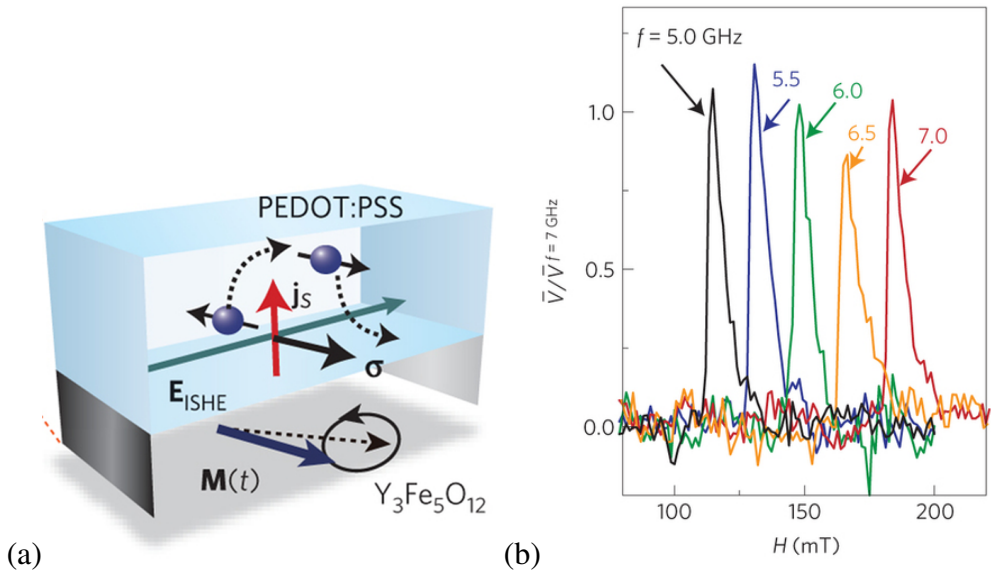

Figure 2.14: *(a) Schematic of $Y_3Fe_2O_{12}$/PEDOT:PSS sample. Here the $Y_3Fe_2O_{12}$ at ferromagnetic resonance pumps spins into the PEDOT:PSS. M(t) is the dynamical magnetisation, E_{ISHE} is the electric field due to the spin charge conversion, σ is the spin polarisation vector and j_s is the flow direction of the spin current. (b) Magnetic field sweep measurements at different frequencies where resonance peaks are measurable in the induced voltage signal. Taken from [40].*

relating to spin pumping into C_{60}.

Ando et al introduced a method to directly convert spin information into an electrical signal [40]. They induced a pure spin current in a solution processed conducting polymer by spin pumping via FMR in an adjacent magnetic insulator and then detected an electrical voltage generated across the polymer using gold electrodes, as shown in the schematic of figure 2.14a [40]. They showed that this generated voltage was consistent with the ISHE in the polymer as discussed in chapter 1. Magnetic field sweep measurements were carried out at different frequencies as shown in figure 2.14b, to show the signal is consistent with spin pumping induced via FMR. A similar experiment was carried out using a semiconducting conjugated polymer, where Hanle precession in the polymer was observed as discussed in chapter 1 [41]. However, in this experiment a Pt film is used a spin sink and the voltage is induced via the ISHE in the Pt film.

CHAPTER 3

Experimental methods

3.1 Deposition methods

In this section, the key concepts involved in the physical vapour deposition techniques used in this project will be outlined: thermal sublimation, sputter deposition and electron beam evaporation. At the start of this research, the samples involving metals and C_{60} were made in separate chambers, ex-situ, leading to oxidation at the interfaces and often producing samples with poor transport properties such as pinholes or high resistances. The C_{60} was initially grown in a separate thermal evaporation chamber attached to a molecular beam epitaxy system and the metallic layers were deposited in a sputter chamber. A key part of achieving high quality samples has been adapting the sputter deposition system so that hybrid metallic-organic samples could be made in-situ. This was achieved by designing and adding a thermal evaporation source to the base plate of the sputter deposition system with a quartz crystal rate monitor and a water-cooled cover.

Some of the samples discussed in chapter 5 and chapter 4 were made during a visit to the Nanodevices group at NanoGune in San Sebastian(Spain). During this visit samples were fabricated using a dual evaporation chamber, in which metals were electron beam evaporated and molecules were thermally sublimated. This system will also be described in this section.

3.1.1 Sputtering process

Sputtering is the growth of high quality thin films via the ejection of atoms from a target due to bombardment with high energy ions. The sputter chamber is pumped down from room pressure to between 20 and 30 mTorr using a roughing pump and then pumped to the order of 10^{-7} Torr using a cryo pump. A Meissner trap is used to draw out the water vapour by creating a low surface temperature of 77 K on the tubing in which liquid nitrogen flows, further reducing the pressure in the chamber to the order of 10^{-8} Torr. The pressure and gas composition/water content in the chamber can be determined using a residual gas analyser (RGA).

A potential difference (approximately 400 V) is applied between the electrodes (the target and the substrate holder are the cathode and anode respectively). Argon is

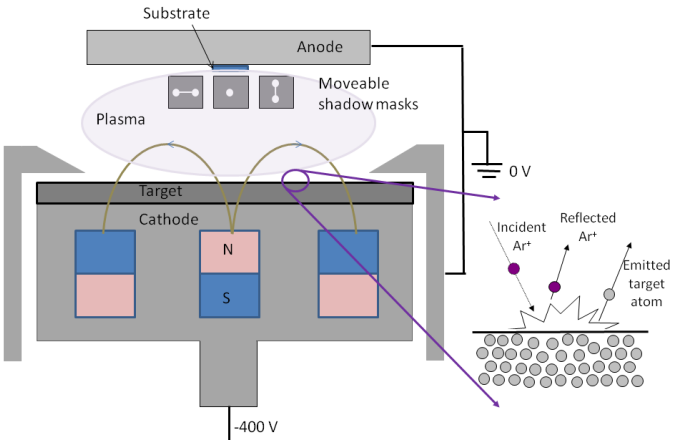

Figure 3.1: *Diagram of DC magnetron sputtering showing the target material with magnets underneath in order to increase the sputtering rate. Figure based on [94].*

introduced into the chamber and is ionised by the potential difference causing a beam of high energy positive argon ions to be accelerated towards the target. The target is bombarded and metal ions are ejected from the surface of the target due to the transfer of momentum from the argon ions and subsequent collisions of atoms. The metal ions then diffuse through the plasma and are deposited on the substrate [91]. In order to increase the sputtering growth rate DC magnetron sputtering is utilised as shown in figure 3.1 [92]. Here the magnetic field is parallel to the target surface. Some electrons are emitted during the collision between the target and the positive ions. The electrons are confined at the target by the Lorentz force because of the magnets beneath the target. The electrons that are confined near the target increase the sputter rate because the rate of ionisation of the argon gas is increased. The atoms ejected have a kinetic energy in the range 1-100 eV, which is two orders of magnitude greater than that of evaporation techniques [93].

The sputter deposition system used in this research consists of 6 non-magnetic guns, 2 magnetic guns, an RF gun and an evaporation source. The sample wheel itself can hold up to 16 different sample holders. There is a shutter system in place so multilayers of different materials can be sputtered or thermally sublimated. The sample wheel and shutter position is controlled remotely using software created within the department.

Before mounting the oxidised silicon substrates into the masks for sputtering, the substrates are cut to appropriate sizes and cleaned with acetone and then isopropanol. As well as cleaning the substrates, this also improves the surface of the substrates for adherence. The magnetron guns are pre-sputtered for 5 minutes before growth in order to clean the targets of unwanted molecules. Movable shadow masks are used to grow samples in a particular shape, for instance the cross hair formation for a tunnel junction or spin valve as shown in figure 3.1. Here three different masks are used: one circular mask for the barrier, one narrow strip with two contact pads for the bottom electrode and another for the top electrode oriented perpendicular to the bottom electrode. There is a mechanical wheel that can be used in the sputter deposition system so that a complete spin valve can be sputtered in-situ.

3.1.2 Plasma oxidation

One method to obtain a thin film insulating barrier is plasma oxidation. First the metal layer is deposited via DC magnetron sputtering. Then both argon and oxygen are introduced into the chamber (with flow rates 16 SCCM (standard cubic centimetres per minute) and 76 SCCM of argon and oxygen respectively in this sputter deposition system) which oxidises the target quickly on ignition of the magnetron gun. This produces a white plasma made up of argon and oxygen ions, mainly the latter. This plasma penetrates the metal layer, reacting with it and thus producing a metal oxide. The oxidation time can be varied depending on the thickness of the initial metal layer.

In order to ensure that this method results in plasma oxidation and not significant reactive sputtering, the level of oxygen added was investigated, where figure 3.2 shows the voltage across the magnetron measured as a function of oxygen flow rate in SCCM. When the oxygen flow rate is below 1 SCCM the Al target is being sputtered normally, in the metallic regime. However once this oxygen flow rate is increased, the Al target becomes oxidised. The change in cathode voltage as a function of oxygen partial pressure is dependent on the target material [95]. For the reactive sputtering of Al in an argon/oxygen mixture, as the oxygen flow is increased, the cathode voltage is decreased. This is a result of the compound on the surface of the target having a

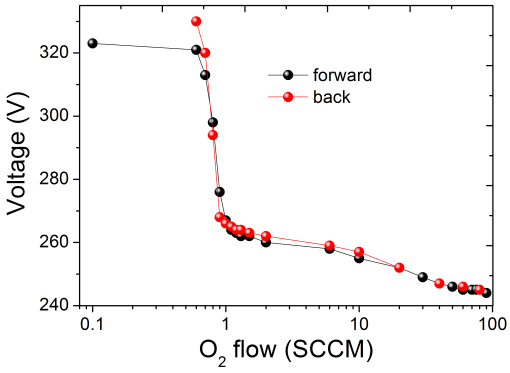

Figure 3.2: *Measurement of the voltage across the magnetron gun with varying oxygen flow rate in SCCM showing below 1 SCCM the Al target is being sputtered normally and beyond 1 SCCM of oxygen the target is being sputtered reactively. As the oxygen flow rate increases, the deposition rate is reduced.*

higher secondary electron emission coefficient than that of Al [95]. With increasing oxygen flow partial pressure, the plasma density is also increased. X-ray reflectivity measurements were performed on samples made using a range of flow rates and the results suggest that the deposition rate decreases with increasing oxygen flow. At 76 SCCM of oxygen, no measurable Al_2O_3 layer was deposited during a 300 s deposition. Therefore, using this method plasma oxidation is being carried out, rather than any significant reactive sputtering.

3.1.3 High vacuum thermal evaporation

Throughout this project C_{60} has been deposited via thermal sublimation in high vacuum where the base pressure in the chamber is approximately 10^{-8} Torr. A high current (typically between 19 and 25 A) is applied to copper electrodes with a tungsten filament attached as shown in figure 3.3. The tungsten filament is very resistive so the high current causes it to heat. A crucible holding the molecules sits in the middle of the filament and heats via Joule heating. This causes the C_{60} molecules inside to thermally sublimate. As a result of the high vacuum conditions the molecules condense on the surrounding surfaces including the substrates positioned above the source. The height of the filament can be varied to change the evaporation throw distance. The

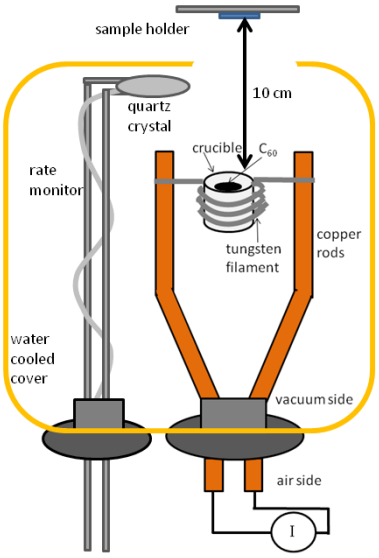

Figure 3.3: *Schematic diagram of the thermal sublimation source added to the base plate of the sputter deposition system. Here there is a power feedthrough on the baseplate of the chamber. A tungsten filament with a crucible filled with C_{60} is attached to the copper rods.*

evaporation source is in a sputter deposition chamber and so the source is encased with a water-cooled copper cover which has a hole in the top to prevent the chamber from being contaminated with C_{60}. The water-cooling was added to prevent heating of the rubber seals in the chamber.

A quartz crystal rate monitor is used to determine the growth rate and the total growth of the C_{60}. The crystals have a resonant frequency in the MHz range which varies because of mass loading by the deposited thin film. As material is deposited the resonant frequency decreases and this change in frequency is used to determine the total growth and thus the growth rate. Owing to space constraints in the chamber, the rate monitor is positioned just a few centimetres above the evaporation source which greatly reduces the quartz crystal life, meaning it gets changed regularly (every few weeks). In order to use the rate monitor, the tooling factor needs to be calibrated by depositing a film and determining the thickness via x-ray reflectivity. The tooling factor compensates for the position of the rate monitor with respect to the evaporation source. The current applied to the tungsten filament can be varied to change the growth rate of the C_{60} as shown in figure 3.4.

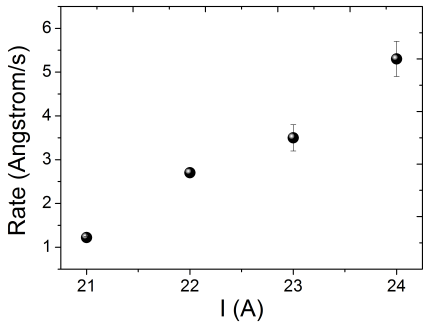

Figure 3.4: *Rate of C_{60} as a function of deposition current determined via x-ray reflectivity.*

3.1.4 Dual chamber evaporator

While working in the Nanodevices group at NanoGune, electron beam evaporation was used to deposit metals, and thermal sublimation was used to deposit C_{60}. A very thorough description of this system is given in the thesis of Dr Marco Gobbi [96]. The system is a dual chamber evaporator, consisting of two separate chambers for organic and metal deposition and a third load lock chamber, where each chamber is equipped with a separate turbo pump. The base pressure is in the range 10^{-10} mbar but it is approximately 10^{-7} mbar during metal deposition. The sample holder is made of copper and can be moved between chambers with a magnetic transfer arm. A shadow masking system was also utilised in order to pattern spin valve devices; the geometry of such devices will be discussed further in chapter 5. To control the thickness of sample layers a thickness monitor and shutter were used. In order to form insulating tunnel barriers a low power plasma treatment in the load lock chamber was used. Here oxygen was introduced into the chamber and a high voltage was used to ignite a white oxygen plasma between the discharge plate and the sample positioned above. A maximum power of 60 W was used with a voltage of 1200 V and 50 mA.

There are 3 effusion cells in the organic chamber. Molecules sit inside a quartz crystal crucible in an effusion cell. A high current can be applied to a small filament which heats the crucible up uniformly until the temperature of the molecules is high enough for sublimation. Then the molecules deposit on the substrate. The dual chamber evaporator can hold multiple organic materials in different cells and the chamber

is rarely vented to atmosphere. The base pressure in the organic chamber is 10^{-9} mbar but it is typically 10^{-8} mbar during deposition.

The electron beam evaporation chamber contains 4 pockets with source materials. A current is passed through a filament to generate an electron beam for thermionic emission. To accelerate the electron beam towards an evaporation pocket, a high voltage is applied and the path of the beam is focused by a magnetic field. The voltage varies the energy of the beam and also its path. The kinetic energy of the electron beam incident on the desired material is converted into heat. If the heating is great enough it causes the metal to sublimate and deposit on a substrate positioned above.

3.2 Measurement Techniques

A range of techniques has been used throughout this research into hybrid magneto-molecular devices which are outlined in this section. X-ray reflectivity was used to characterise the thicknesses and roughness of samples, from single layer thin films to multilayers. Low temperature electron transport measurements have been used to investigate the behaviour of hybrid magneto-molecular devices at a range of temperatures. Magnetometry measurements have been used throughout this research including vibrating sample magnetometry, magneto-optical Kerr effect (MOKE) and Kerr microscopy to measure the magnetic hysteresis loops of hybrid C_{60} magnetic layers, including bilayers and multilayers. Raman spectroscopy and photoluminescence are discussed further in this chapter. In the latter section of this chapter the ferromagnetic resonance measurement technique and data analysis will be discussed thoroughly.

3.2.1 X-ray reflectivity

X-ray reflectivity and x-ray diffraction are techniques that use the coherent interference of scattered x-rays to determine roughness, thickness and/or crystal structure of materials. Bragg's law describes the diffraction between two scattering centres of separation d that have different electron densities written as [97]

$$n\lambda = 2d\sin\theta, \tag{3.1}$$

where n is an integer, λ is the wavelength and θ is the angle of coherent interference. To generate x-rays a tungsten filament is heated up and electrons are emitted via thermionic emission. A voltage is then applied to these electrons to accelerate them into a copper target, which excites electrons in the copper target into higher energy levels. When the excited electrons relax into their ground state photons are emitted of characteristic Cu kα and Cu kβ wavelength. These x-ray photons are directed through slits and filters to collimate the beam and filter out the Cu kβ x-rays.

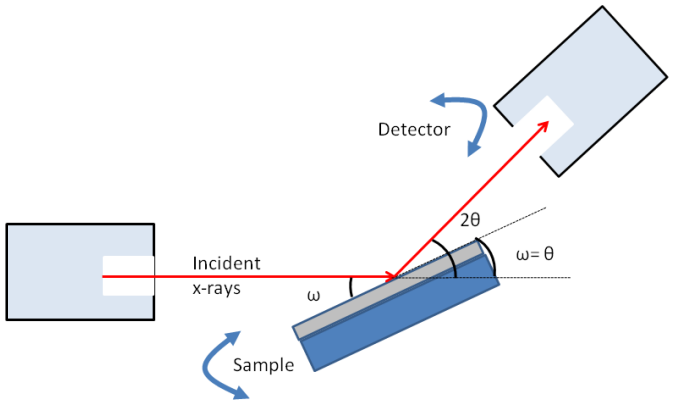

Figure 3.5: *X-ray reflectivity schematic showing x-rays incident on a sample at angle ω and x-rays reflected from this sample reaching a movable detector at angle θ.*

These x-rays can be directed towards a sample at angle ω and reflected x-rays can be detected by a movable detector at angle θ as shown in figure 3.5. Measuring at the specular condition, where $\omega = \theta$, probes coherent scattering of x-rays. In order to maintain specular reflection, the detector moves double the angle the sample moves as shown in figure 3.5. For a thin film of thickness t, at low incident angles, x-rays can reflect off the film/air interface. Beyond the critical angle θ_c for total internal reflection, the x-rays can also reflect off the film/substrate interface. Oscillations in the reflected intensity as a function of angle can be observed as a result of interference between different numbers of internal reflections [98]. These oscillations in reflected intensity are known as Kiessig fringes and they can be used to determine the thickness, t, using the relationship

$$\lambda = 2t\sqrt{\sin^2\theta_m - \sin^2\theta_c}, \tag{3.2}$$

where θ_m is the angular position of constructive peaks is θ_m.

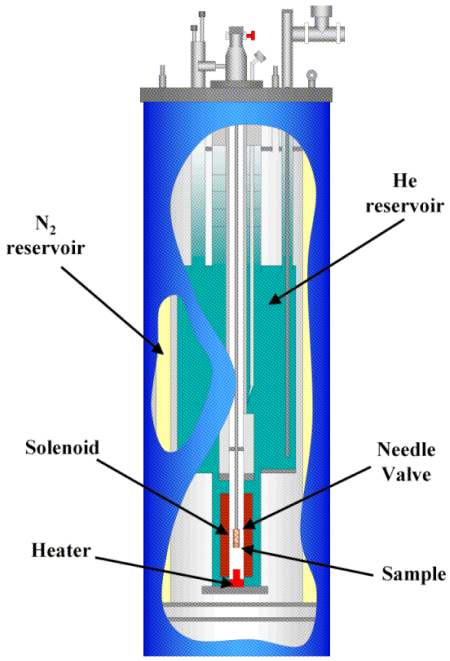

Figure 3.6: *Schematic of the Oxford instruments cryostat with a temperature range of 1.4 to 300 K. Taken from [94].*

3.2.2 Low temperature transport measurements

In order to investigate the effect of temperature on transport properties, low temperature electrical measurement techniques are required. An Oxford instruments cryostat was used to vary the temperature from 1.4 K to 300 K with the capability to perform electrical measurements as shown in the schematic in figure 3.6. A variable temperature insert (VTI) sits inside the cryostat. A sample can be electrically contacted using a variety of sample holders and connected to the end of a wired stick that can be placed inside the VTI. The VTI sits inside a liquid He reservoir at 4.2 K which is used to cool both the sample and the superconducting magnets to below the critical temperature. The superconducting magnets can produce magnetic fields of up to 8 T. The He reservoir is surrounded by an outer jacket filled with liquid nitrogen which shields the He reservoir from the ambient room temperature. The VTI is continuously pumped by an oil free scroll pump to below atmospheric pressure. This lowers the vapour pressure allowing cooling down to 1.4 K. The temperature is controlled using a heater and a needle valve (NV) which allows in He gas.

3.2.3 Vibrating sample magnetometry

The vibrating sample magnetometer is used to perform magnetic hysteresis loop measurements. The sample is mounted onto a detachable tip and secured using PTFE (polytetrafluoroethylene) tape. The detachable tip is made out of a thermal diamagnetic plastic to reduce background signal. The detachable tip is then attached to the end of a rigid PEEK (polyether ether ketone) rod which oscillates vertically in the machine at a frequency range 43-67 Hz and an amplitude range 0.1-1.5 mm. This rod vibrates inside pick up coils while an external magnetic field is applied parallel to the rod by the superconducting magnets which surround the sample chamber. Electromotive force (EMF) is then induced in the coils as a result of time-varied magnetic flux. The alternating voltage produced is detected and converted into a magnetic moment; the magnetic moment is therefore measured while changing the magnetic field. The temperature can be varied from 1.3 K to 300 K using cryogenic gases and a heater. A roughing pump is used to continuously pump out the VTI similarly to the cryostat discussed in section 3.2.2. A needle valve can be controlled to introduce He gas which is also heated by the heating stage in order to control the sample temperature.

3.2.4 Magneto-optical Kerr effect techniques

The magneto-optical Kerr effect (MOKE) is the change in polarisation of the light reflected from a magnetic medium. Plane polarised light can be considered as a combination of right-handed circularly polarised light and left-handed circularly polarised light. These two components have different refractive indices depending on the orientation of the magnetisation. The magnetisation of the ferromagnetic material dictates the phase difference between the two circularly polarised components when they combine upon reflection [99].

The MOKE magnetometer is used to carry out magnetic hysteresis measurements. The MOKE is set up on an optical bench and is made up of a helium-neon (HeNe) laser incident on a lens and a polariser. This polarised beam reflects off the sample which is set on an adjustable mount between electromagnets. The reflected beam passes through an analyser and lens before being detected at the photo diode. The photo diode detects

varying polarisation as the magnetic field is changed and thus the change in magnetisation can be detected as a voltage (Kerr voltage) [99].

There are three orientations in which a MOKE experiment can be carried out. Firstly polar MOKE is when the measurement of the magnetisation is perpendicular to the sample surface and normal to the angle of incidence. Longitudinal MOKE is when the magnetisation is parallel to the sample and transverse MOKE is when the magnetisation of the sample is perpendicular to the optical plane of incidence. For both longitudinal and transverse MOKE the angle of incidence is oblique [100].

Similarly to MOKE magnetometry, Kerr microscopy utilises the Kerr effect in magnetic samples. However, in this set-up a white light source is used rather than a laser and an optical microscope is used to detect the signal. The change in polarisation of the light as a result of the Kerr effect is converted to different light intensities by an analyser. This change in light intensity can be detected by the optical microscope and an image can be created by computer software by measuring the contrast across the surface of a sample [101].

3.2.5 Raman spectroscopy

The Raman spectrometer used in this research is a Horiba-Jobin-Yvon LabRam HR system as shown in figure 3.7. Monochromatic light emitted from a laser is reflected off a mirror and through a number of filters. Firstly the light goes through a line filter which narrows the Gaussian distribution of the photons around the desired wavelength. Then the filtered light is sent through an adjustable intensity filter to control the intensity of light incident on a sample. This filtered light is then reflected off two 2-way mirrors and through a microscope and reflects off a sample placed below the microscope. The microscope has a 20, 50 and 100 $\times$ objective lens. The microscope can be focused on the sample using a white light source and the video that is taken using a USB camera. Light that is scattered off the sample passes through the microscope, reflects off the first 2-way mirror and is transmitted through the second 2-way mirror [69]. A long wave pass filter removes the elastically scattered light leaving the inelastically scattered light to diffract off the diffraction grating. A charge coupled device

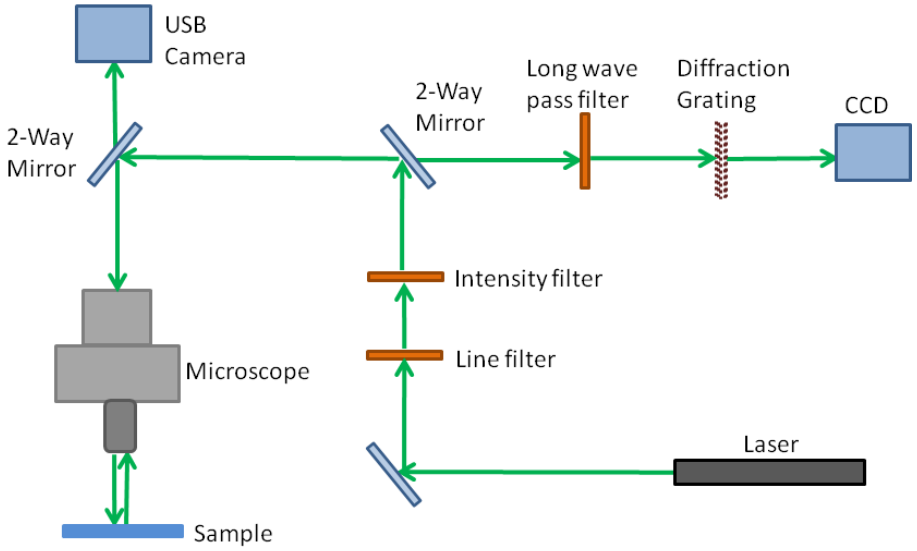

Figure 3.7: *Schematic of the Raman spectrometer. Based on [69].*

(CCD) is used to detect the diffracted light thus measuring the spectra, the intensity of light with varying wavenumber. The diffraction grating is rotated to measure a large range of wavelengths. The diffraction grating size can be varied to change the resolution of the spectra in wavenumber, however an improvement in resolution results in a narrower band of the spectrum being incident on the CCD at any one time.

Three lasers can be used: a red 633 nm HeNe laser, a green 532 nm Nd:YAG and a blue 473 nm diode pumped solid state laser. The green and blue laser were used in this research, whereas the red laser was less desirable when measuring C_{60} as it gave a significant fluorescence signal as shown in figure 3.8a. The sample can be positioned on a movable motorised x-y-z stage allowing Raman maps in position to be performed. The system has been made adaptable to allow simultaneous transport or FMR measurements and to measure samples with a magnetic field if required.

Samples can be cooled or heated in an Oxford Instruments Microstat HiRes II continuous flow liquid He microstat to observe the effect of temperature on Raman spectra or luminescence spectra. The microstat can be pumped by a diffusion pump to avoid condensation when cooling. The microstat has a copper ”cold finger” and is surrounded by coils in which He can flow through in order to cool effectively. Elec-

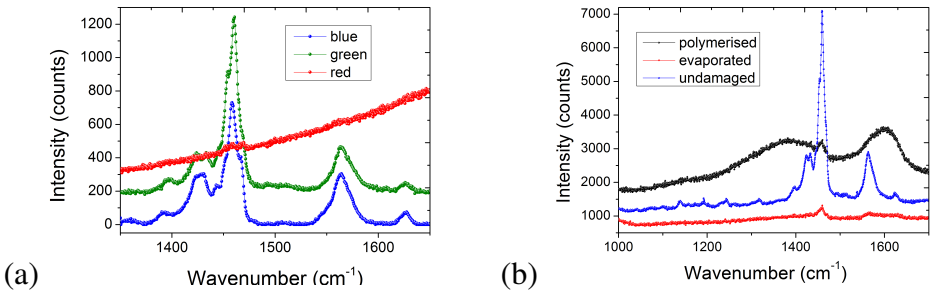

Figure 3.8: *(a)Raman spectra on C_{60} comparing the red, green and blue lasers. This shows that there is significantly more fluorescence when performing Raman spectroscopy using the red laser. (b) Raman spectra showing the polymerisation and evaporation of C_{60}. The first spectrum represents the first measurement of the C_{60} before over-exposure to the laser. The C_{60} Raman peaks are changed after polymerisation of the C_{60} and the peaks are more similar to amorphous carbon. The C_{60} peaks are no longer present when the C_{60} has been evaporated.*

trical contact can also be made to the sample inside the microstat via the electrical feedthrough.

The C_{60} undergoes heat induced polymerisation when it is exposed to the laser of too high an intensity or power. This effect is shown in figure 3.8b where the C_{60} peaks in the first spectra are more intense than in the second spectra. To avoid polymerisation of C_{60} the intensity of the laser incident on the sample can be reduced, for instance typically 0.1 % of the blue laser is used when measuring C_{60}. The Raman spectra can be analysed using LabSpec 6 software. Here, backgrounds can be extracted and a mixture of Lorentzian and Gaussian peaks can be fitted.

3.2.6 Photoluminescence

The Raman spectrometer can also be used to perform photoluminescence measurements. Photoluminescence is a spectroscopic technique utilising the absorption and re-emission of photons. Photons with an energy greater than that of the band gap of a semiconductor are incident on the sample then the photons are absorbed, creating an electron-hole pair. These excited electrons in the lattice then scatter and lose energy, When an electron recombines with a hole in the HOMO (or valence band) then a pho-

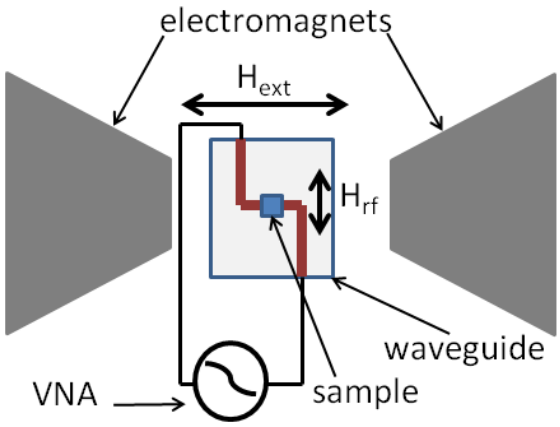

Figure 3.9: *FMR set up schematic. Here a 50 ohm impedance matched waveguide is sitting in a DC magnetic field, H_{ext}. The microwave field, H_{rf}, from the GHz frequency through the waveguide is generated perpendicular to the DC field. A sample can be placed face down on top of the waveguide.*

ton is emitted. Photoluminescence measurements provide information about the film crystallinity and electronic structure.

3.2.7 Ferromagnetic resonance

The ferromagnetic resonance measurement technique discussed in this section was set up as part of my PhD. I developed a LabView plug-in for existing measurement software with the help of Dr Gavin Burnell in order to communicate with the vector network analyser (VNA) to perform ferromagnetic resonance and simultaneous electron transport measurements. Professor Robert Stamps and Francisco Goncalves from the University of Glasgow also helped with advice on experimental set-up and waveguide design. The set-up consists of a VNA to output microwave pulses, using frequencies up to 26.5 GHz, transmitted through a purpose built 50 ohm impedance matched waveguide sitting between magnetic coils. The specific measurement protocol and data analysis will be discussed in this section. Results taken on this set-up will be compared to accepted values for permalloy to show the quality of measurements that can be obtained from this ferromagnetic resonance system.

As discussed in chapter 2, when a ferromagnetic material is placed in a magnetic field, the magnetisation of the ferromagnetic material will precess about the magnetic field. When the microwave frequency applied through the waveguide is at the same frequency as this precessional frequency there is strong power absorption. The effective magnetisation and damping constant/mechanism can be determined from analysing ferromagnetic resonance data as discussed in the following subsections.

3.2.7.1 Measurement protocol

There are a number of methods that can be used to measure FMR, a review of which can be found in reference [102] for a review on the key techniques. In the 1960s a stripline FMR technique was developed [103]. In this method the linewidth is measured by sweeping the magnetic field at a set frequency. Similarly to this the shortened waveguide and microwave cavity techniques were introduced [104; 105]. Typically with VNA-FMR techniques the magnetic field is fixed and the frequency is swept, and the reflection and transmission through a waveguide are measured [106].

The standard FMR set-up used in this research consists of an Agilent N5222A network analyser that can output frequencies up to 26.5 GHz through a waveguide to excite a sample in a DC magnetic field. This technique is widely used and is known as the VNA-FMR technique. The technique chosen for this project is an easily adaptable method to use simultaneously with optical spectroscopy or electron transport. A basic schematic is shown in figure 3.9, where the waveguide is positioned between two magnetic coils. The orientation of the strip line of the waveguide with respect to the magnetic field is important, as the microwave pulse produced by the high frequency current transmitted through the waveguide must be perpendicular to the DC field.

The VNA used to apply high frequencies through the waveguide has two ports that can be used. The S_{11} and S_{22} parameters represent the reflection coefficients at the first and second ports respectively whereas S_{12} and S_{21} represent the transmission coefficients through the waveguide. A variety of methods to allow the high frequency pulses to reach the sample without major power losses were investigated during this research. One method was to use picoprobe micropositioners as shown in figure 3.10 to

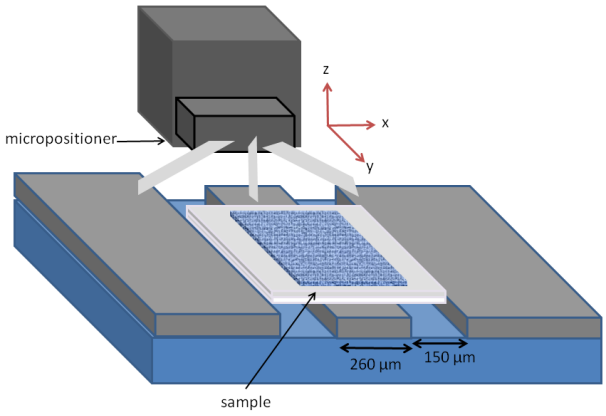

Figure 3.10: *Schematic diagram of micropositioners contacting a co-planar waveguide deposited on silicon. The sample is sitting on top of the strip line.*

contact a gold or aluminium waveguide deposited on a silicon/silicon oxide substrate. It was found that the contact itself was not robust and the power losses would vary from contact to contact. In terms of reproducibility and reliability for a ferromagnetic resonance system to be used simultaneously with Raman, luminescence or electron transport measurements, this method proved to be suboptimal.

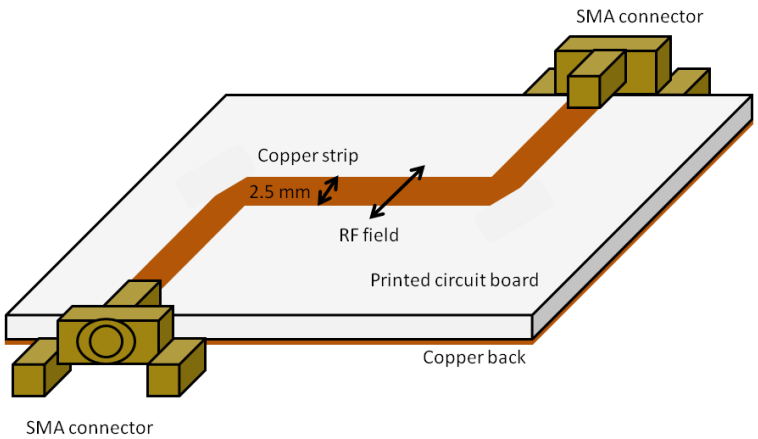

Figure 3.11: *(a) Schematic diagram of the SMA connected PCB waveguide. Here a copper strip on the top side of the waveguide is the microwave stripline. The direction of the RF field produced is labelled.*

The optimum method to excite the ferromagnetic samples to resonance was found

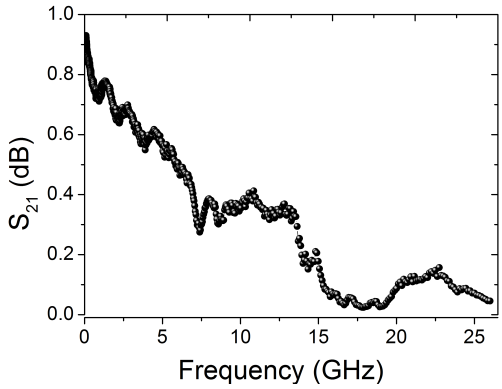

Figure 3.12: *S_{21} transmission through a 50 Ohm impedance matched PCB waveguide, showing the power losses as a function of frequency up to 26.5 GHz.*

to be a printed circuit board (PCB) waveguide etched to have a copper track on the front side but with a full copper back side. This method was the most robust because the connectors were secure ensuring that the power losses through the waveguide do not change significantly from measurement to measurement. SMA connectors attach to the PCB, where the back acts as the ground and the front as the strip line. The SMA connectors are also 50 ohm impedance matched up to 26 GHz and can be attached to high frequency cables using a torque wrench (set to 0.9 N·m) to ensure good contact. A schematic of the waveguide is shown in figure 3.11. The response through such a waveguide is given in figure 3.12 where the scattering parameters reveal significant power losses beyond 14 GHz. There are power losses up to 14 GHz but the power transmission is sufficient for the sensitivity of measurements in this research. A number of waveguide variations have been used, however this section will cover the design of the waveguide guide in the standard FMR measurements.

One can either vary the magnetic field at a set frequency or vary the frequency at a set magnetic field. These two methods will be discussed separately because the data is analysed in different ways to extract the damping parameter and effective magnetisation respectively. Firstly, if the magnetic field is varied at a set frequency, at the resonant frequency a negative peak with a linewidth will be observed in the S_{21} parameter as shown in figure 3.13a. These measurements can be carried out at a range of

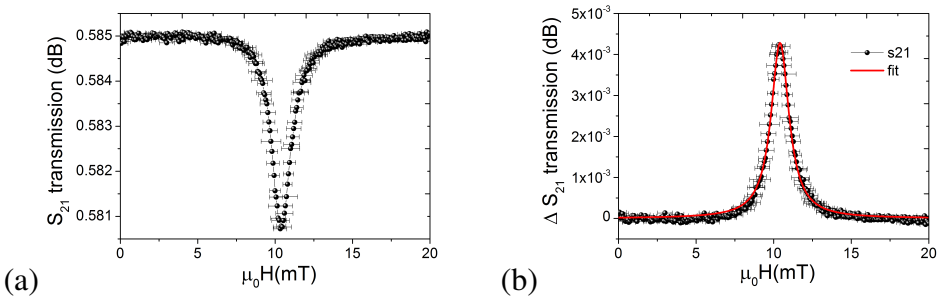

Figure 3.13: *Magnetic field sweep FMR measurement at 3 GHz on 20 nm of Py.(a) Raw S_{21} transmission data. (b) A Lorentzian fit (red) to the change in transmission data through the waveguide.*

magnetic fields in order to determine the dependence of linewidth on magnetic field. The S_{21} signal is a combination of the sample and waveguide response as well as background contributions. The data can be corrected by fitting a polynomial to the background and removing this background. The waveguide and substrate response can be removed from the data by measuring field sweeps of just a substrate (ie glass or silicon) at the same range of frequencies, and dividing the actual data by this. However, for sample thicknesses above 10 nm of materials measured in this research (Co, Py, YIG) the contributions from the substrate response in comparison to the resonance peaks are minimal and so they can be ignored. Using equation 3.3 a Lorentzian function can be fitted to this corrected data in order to extract the relevant parameters as shown in figure 3.13b. The Lorentzian function can be written as

$$S_{21}(H) = \frac{(\Delta H)^2}{(\Delta H)^2 + (H - H_{res})^2}, \tag{3.3}$$

where S_{21} is the transmission through the waveguide as a function of magnetic field. H_{res} is the resonant field, H is the applied magnetic field and ΔH is the linewidth.

Field sweep measurements can be carried out for a range of frequencies, where the linewidth increases with increasing frequency, as is evident in figure 3.14. The dependence of the linewidth, ΔH, on frequency is related to the Gilbert damping parameter, α, as shown in figure 3.15. The relationship between α and the change in linewidth with frequency can be written as

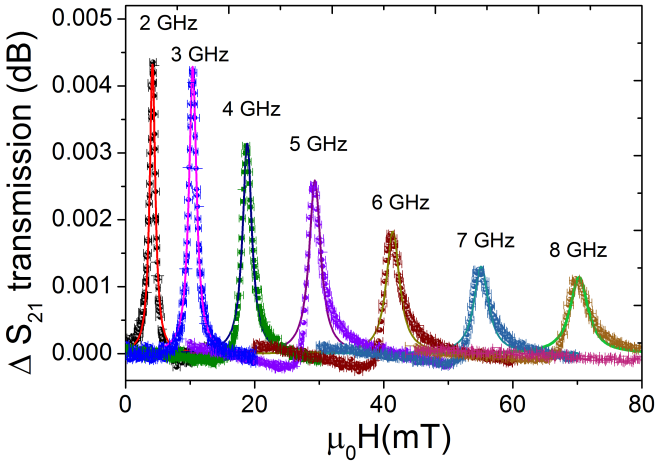

Figure 3.14: *Multiple magnetic field sweep data for 20 nm Py sample showing data (points) and Lorentzian fits (lines) at different frequencies.*

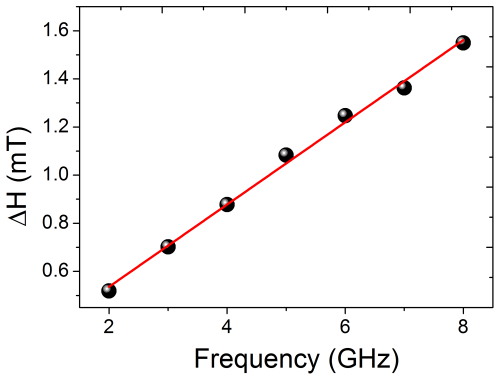

Figure 3.15: *Change in linewidth with frequency for a Py film. A linear fit is used to determine the gradient so that the Gilbert damping parameter can be extracted.*

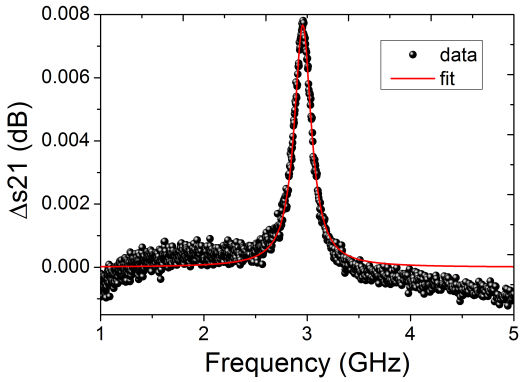

Figure 3.16: *Example of Lorentzian fit to frequency sweep data with an external magnetic field of 10 mT for a Py film.*

$$\Delta H_{HWHM} = \Delta H(0) + \frac{\alpha f}{\gamma}, \tag{3.4}$$

where γ is the gyromagnetic ratio and $\Delta H(0)$ is the extrapolated linewidth at zero frequency. Using equation 3.4 α was determined for a 20 nm Py film to be 0.0090 $\pm$ 0.0005. This is in relatively good agreement with typical literature values of 0.008 [107].

The analysis of the frequency sweep measurements at different fields is somewhat more complicated and the peak can not simply be observed in the raw data because the change in the transmission through the waveguide due to the sample is masked by the power loss profile through the waveguide. One can use a zero field normalising method, where subsequent frequency sweep data can be divided by the zero field frequency data. The very low field/frequency measurements can be ignored when analysing the data. The frequency sweep data is used to extract the peak positions in terms of field and frequency by first normalising the data (dividing through by a zero field sweep), then extracting a background and fitting Lorentzians to the corrected data to extract the relevant parameters. Figure 3.16 shows an example normalised frequency sweep measurement with an applied field of 10 mT for a Py film with a Lorentzian fit.

The position of the resonant peaks in terms of frequency can be extracted for a range of magnetic fields and then fitted to the Kittel equation, which describes the

relationship between magnetic field, *H*, and the resonant frequencies, f, is given in equation 2.31 [88]. However, there is typically a field offset in the measurements as a result of remnance in the coils. Therefore the Kittel equation in the fit is modified to take into account such an offset and can be written as

$$f = \gamma/2\pi(|H - H_{off}|\,(|H - H_{off}| + \mu_0 M_{eff}))^{1/2}, \tag{3.5}$$

where H_{off} is the magnetic field offset. It is reasonable to remove this field offset for a standard ferromagnetic sample, if there is no physical reason for the ferromagnetic resonance frequencies to be offset in magnetic field (such as exchange bias as discussed in chapters 4 and 5). One must however be careful when measuring an exchange biased system, where this offset may actually be real rather than simply a feature of the measurement protocol. Figure 3.17 shows the Kittel fit for a Py film, where the effective magnetisation was extracted from the fit to be (1.098 $\pm$ 0.004) T and the magnetic field offset was found to be (1.6 $\pm$ 0.1) mT. This value for the effective magnetisation is comparable to literature values of approximately 1.01 T [108]. Thus, the ferromagnetic resonance system is reliable and sensitive enough to measure the samples in this research.

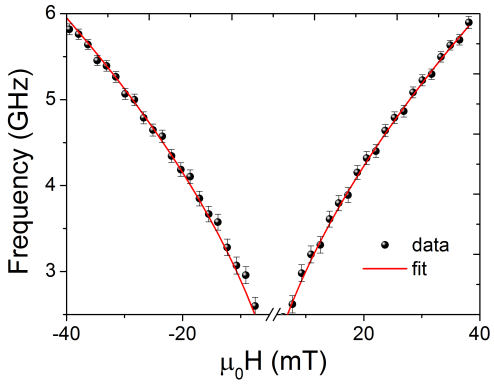

Figure 3.17: *Position of resonant peaks in frequency and field fitted to the Kittel equation for a 20 nm Py film.*

CHAPTER 4

Properties of magneto-molecular interfaces

4.1 Introduction

The hybrid interfacial states between organic and inorganic layers are of utmost importance in the functionality of devices [79; 80]. Three key requirements for working hybrid-organic magnetic devices such as organic spin valves are: good spin injection, spin diffusion and spin detection. The interfacial region is very important for good spin injection and spin detection. The term spinterface was coined by Sanvito to describe the broadening and shifts in the density of states of a molecule and a metal as they are brought into contact [79]. This hybrid interfacial state may have different properties from the rest of the material, for instance the organic layer at the interface may become metallic or even magnetic. In order to successfully fabricate functional hybrid organic magnetic devices, an understanding of interfacial effects is crucial.

There is expertise in sputter deposition of normal metals and ferromagnetic materials within the Condensed Matter group in Leeds, thus growing such materials is well known and reproducible. Therefore, the characterisation and results discussed in this chapter are focussed on C_{60} and the C_{60}/metallic interfaces which were relatively new areas of research for the group. Magnetic/C_{60} multilayers and bilayers were deposited and characterised in order to fully understand interfacial effects and to assure the deposition of reproducible samples in-situ. These multilayer structures deposited via sputtering and thermal sublimation have been investigated using XRR, TEM and VSM. These samples have been compared to samples I made during my secondment in the Nanodevices group in NanoGune via electron beam evaporation and thermal sublimation. The aim was to make progress towards fabricating hybrid organic spin valves with C_{60} as the active spacer layer, the results of which are shown in chapter 5, by first understanding the interaction between C_{60} and ferromagnetic materials. The first step we took towards doing this was to characterise multilayer and bilayer C_{60}/ferromagnetic samples as well as depositing copper based exchange biased spin valves on top of C_{60} under layers to check the functionality of such devices. This chapter will discuss these results, including the effect of C_{60} on the magnetic properties of the devices through MOKE and current-in-plane electron transport measurements.

4.2 Characterisation of hybrid C_{60} magnetic multilayers

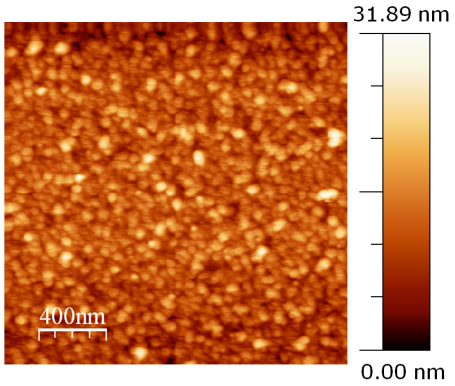

Figure 4.1: *AFM image of C_{60} showing the root mean squared roughness to be 3.8 nm for a 50 nm film. The candidate's data published in reference [47]* © *2012 IEEE.*

In order to further investigate interfacial effects between Co and C_{60}, repeated multilayers of these materials have been deposited and measured using XRD, TEM and VSM. The effect of this organic/inorganic interface has been studied in samples with nominal thicknesses (C_{60}(10 nm)/Co(3.5 nm)) $\times$ 5 repeated layers deposited on oxidised silicon substrates and capped with Al. The deposition of magnetic multilayers between the system used in the Nanodevices group at NanoGune and the Condensed Matter department at the University of Leeds were compared. A typical AFM measurement for C_{60} is given in figure 4.1, revealing the RMS roughness to be 4 nm for a 50 nm C_{60} film. The sputter deposited Co was grown at 25 mA instead of 100 mA (approximately 10 W instead of 40 W), which is the deposition current typically used for Co in the sputtering chamber. This was to make the Co deposition less energetic to avoid damage or diffusion of the Co into the C_{60}. XRR measurements were performed on these magnetic multilayer samples as shown in figure 4.2 for the electron beam deposited Co (a) and the sputter deposited Co sample (b). The XRR data was fitted using Bede REFS software package which can simulate grazing incidence XRR profiles from thin film structures [109]. The thickness of each layer and root mean square roughness R_{RMS} can be extracted from the fit. The electron beam evaporated sample is confirmed to be (C_{60}(12.5 $\pm$ 0.9 nm)/Co(3.2 $\pm$ 0.2 nm)) $\times$ 5 multilayer and

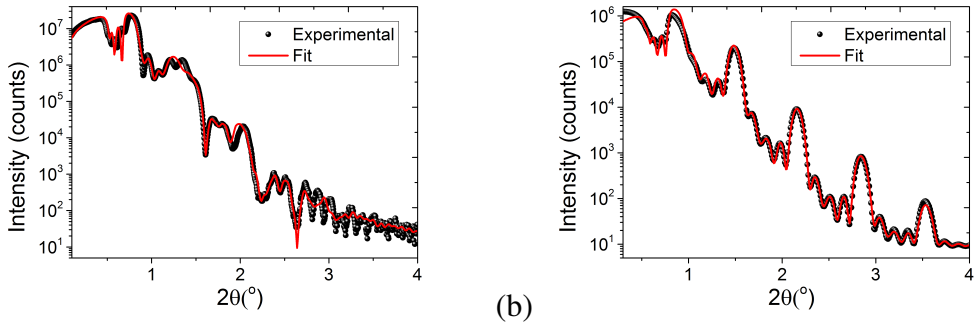

Figure 4.2: *X-ray reflectivity measurements of (a) an electron beam evaporated (C_{60}(12.5 ± 0.9 nm)/Co(3.2 ± 0.2 nm)) × 5 multilayer, and (b) a sputter deposited (C_{60}(9.0 ± 0.2 nm)/Co(3.6 ± 0.1 nm)) × 5 multilayer. Both samples were capped with 5 nm of Al.*

the sputter deposited sample is confirmed to be (C_{60}(9.0 ± 0.2 nm)/Co(3.6 ± 0.1 nm)) × 5 multilayer.

Each layer was fitted separately and the results revealed there was more variation in the thicknesses of each layer for the electron beam evaporated sample as shown in table 4.1. One possible reason for the greater variation in thickness in the electron beam evaporated sample is the delay between the deposition of each layer on the order of 20 minutes because the sample has to be moved between the organic chamber and the metal chamber. To move from one chamber to another, the current to the thermal evaporation source or electron beam evaporation was reduced to below a deposition current. The current would then be increased again to deposit the subsequent layer, which may lead to inconsistencies between layers. However, during the deposition of the sputter deposited sample, there is just a number of seconds between the deposition of each layer. This will also mean there is less contamination for example from oxygen.

R_{RMS} can also be extracted from the fits and is defined by a combination of the interdiffusion and roughness of layers as shown by

$$R_{RMS} = \sqrt{roughness^2 + interdiffusion^2}. \tag{4.1}$$

R_{RMS} of the electron beam evaporated Co sample was found to have a roughness of 1.7 nm and the sputter deposited Co to have a roughness of 1.3 nm. This initially came as

a surprise because electron beam evaporation is a less energetic process so one would expect sharper interfaces than the sputter deposited Co sample, rather than comparable roughness. This result in itself implies that there is little interdiffusion of Co into C_{60} or vice versa in either sample. However, the electron beam evaporated sample has an increased R_{RMS} which could be a result of more interdiffusion of layers or roughness.

Table 4.1: Thicknesses of each layer in nm for the C_{60}/Co $\times$ 5 multilayer samples prepared by electron beam evaporation or sputter deposition of Co..

Layer	C_{60} (e beam)	Co (e beam)	C_{60} (sputter)	Co (sputter)
1	15.4	3.15	9.26	3.50
2	14.4	2.97	8.88	3.71
3	11.1	3.09	8.87	3.73
4	10.7	3.91	8.88	3.73
5	11.1	2.90	8.81	3.50

TEM measurements were carried out on the same C_{60}/Co $\times$ 5 multilayer samples to further characterise the interfaces between the C_{60} and Co as well as to compare the electron beam evaporated and sputter deposited Co samples. Smooth and sharp interfaces, with no interdiffusion between the Co and C_{60} would be ideal for devices. The intensity profile of the samples made via electron beam evaporation and sputter deposition are given in figure 4.3a and figure 4.3b respectively. The derivative of the intensity profile can give an idea of the sharpness of the interface, revealing the sputter deposited sample to have a sharper and smoother interface than the electron beam deposited sample. This was unexpected because the sputter deposition process is more energetic than electron beam evaporation, so one would expect the interfaces to be worse. Furthermore, it can be seen in the TEM images shown in figure 4.3 that the sputter deposited sample has smoother interfaces than the electron beam deposited sample. These results led us to conclude that C_{60} is robust enough to withstand the sputter deposition of metals on top and suggests that this deposition technique is suitable for C_{60} spintronic devices. It was already known that C_{60} could withstand deposition of metals on top via electron beam evaporation [18].

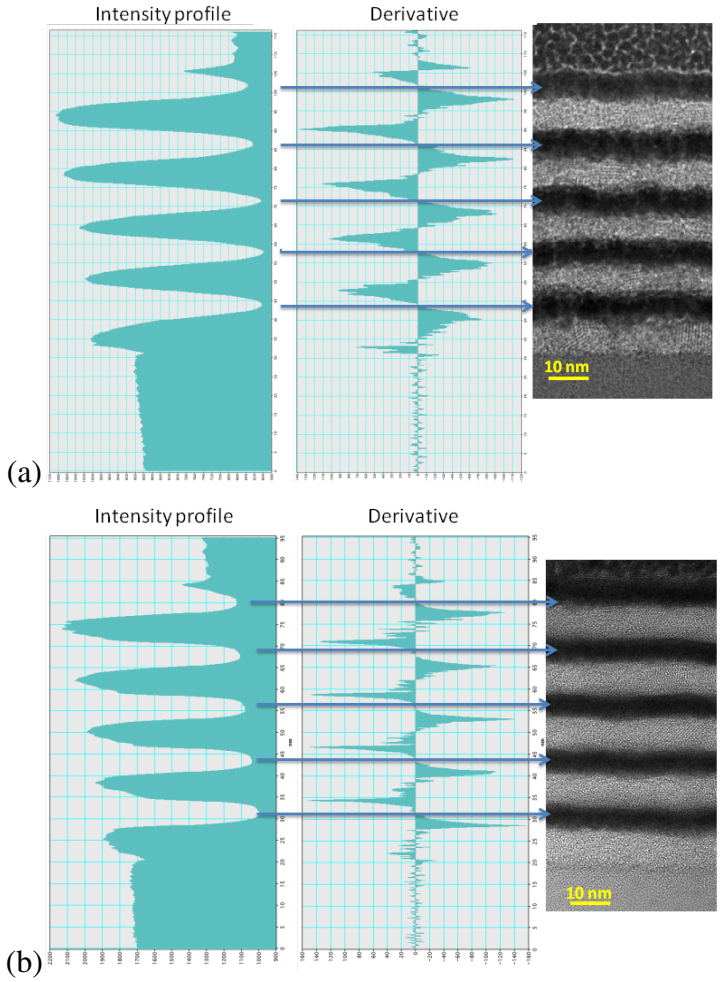

Figure 4.3: *Intensity profile, derivative and TEM image of a C_{60}/Co $\times$ 5 multilayer where the Co is (a) deposited via electron beam evaporation. The derivative of the intensity profile shows the interfaces are not very sharp. The TEM measurement shows rough interfaces. (b) deposited via sputter deposition. The derivative of the intensity profile shows the interfaces are sharp. The TEM measurements show smooth interfaces and no interdiffusion. TEM measurements were done at NanoGune.*

Figure 4.4 shows the VSM data of (C_{60}(9.0 nm)/Co(3.6 nm)) and Ta(10 nm)/Co(3 nm) multilayers at 100 K. The latter sample was deposited and measured as a control sample. Here it is evident that the shape of the magnetic hysteresis loops are different when comparing the control and the C_{60} sample. The Co/C_{60} multilayers require a greater field in order to saturate the Co in comparison to the Co/Ta multilayers. The overall magnetic moment is also greater for the Co/Ta multilayers than the Co/C_{60} multilayers even though there is the same amount of magnetic material in the samples. This suggests that interfacial effects between the Co and C_{60} are affecting the magnetic properties of the Co. The thickness of the Co layers in these samples are less than that of the exchange length of Co so the interfacial effects will extend into the whole of the Co layer [110]. Increased saturation fields can be attributed to pinning and antiferromagnetic interactions. It has been proposed that this reduction in the overall magnetic moment for the sample containing C_{60} is a result of hybridisation and spin doping in the C_{60} [46]. Charge transfer occurs when two materials of different chemical potentials are in contact. If one of the materials is ferromagnetic then this charge transfer may be spin polarised, leading to a spin doping effect. It has been shown in bilayer Co/C_{60} samples that the C_{60} becomes doped with spin polarised electrons when in contact with Co and it can also reduce the net spin polarisation of the Co by up to 21 % [46].

One could suggest that the reduction in magnetisation of the C_{60} sample in figure 4.4a is a result of one Co layer being significantly magnetically harder than the other layers. This could arise from oxidation of the top layer forming Co oxide, which is antiferromagnetic, which would also act to reduce the net magnetisation [111]. However, this is doubtful because the sample was capped with 5 nm of Al, similarly to the control sample, where this effect is not observed. However, as a result of roughness in the layers, there is a possibility that the 5 nm Al cap is not continuous and therefore allows oxidation of the adjacent Co layer. If this were the case we would also expect there to be exchange bias and therefore the hysteresis loop shifted away from zero which was not observed.

The unusual shape of the Co/C_{60} multilayer hysteresis loop can be explained by roughness in the C_{60} causing nucleation of the magnetic domains at the interface. A

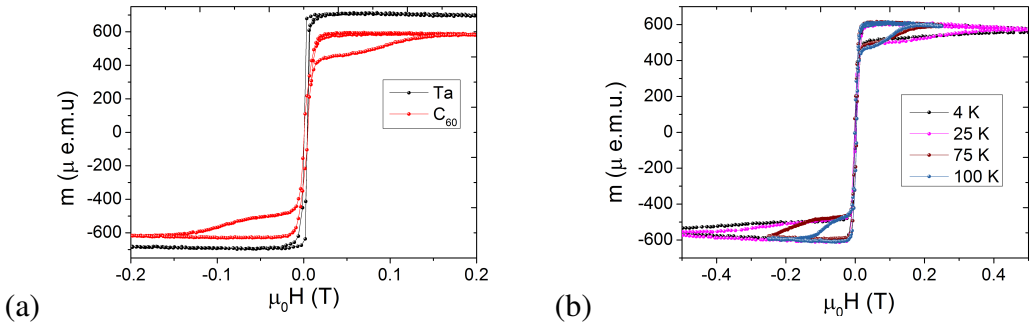

Figure 4.4: *(a) VSM data comparing the magnetic properties of (C_{60}(9.0 nm)/Co(3.6 nm)) × 5 multilayers and Ta(10 nm)/Co(3 nm) × 5 multilayers at 100 K. (b) VSM data showing the temperature dependence of the magnetic properties of (C_{60}(9.0 nm)/Co(3.6 nm)) with 5 repeats.*

greater roughness leads to a larger contact area which increases the spin dispersion at the interface leading to an increased magnetic coercivity [112]. However, this explanation is not sufficient to explain all of the effects of the hybrid interfacial state. Figure 4.4b shows the temperature dependence of the magnetic properties of the Co/C_{60} multilayers. At lower temperatures it takes a greater magnetic field in order to saturate the nucleated magnetic domains. Polarised neutron reflectivity (PNR) was performed by Moorsom et al on Co/C_{60} multilayers to determine the induced moment in C_{60}, which was found to be 1.2 μ_B per C_{60} molecule [46].

To simplify the interpretation of magnetic characterisation, bilayer Co/C_{60} samples were also measured so that only one hybrid interfacial state need be considered as shown by Moorsom et al [46]. Figure 4.5a shows the sample schematic for the Co/C_{60} bilayer samples as well as an arrow representing the transfer of spin polarised electrons from the Co into the C_{60}. The samples have a Ta under layer and an Al protective capping layer. Figure 4.5b shows VSM data carried out at 100 K on a Co/C_{60} bilayer sample and Co/Cu/C_{60} samples with Cu thickness of 1 nm and 5 nm in the respective samples. From this data it is apparent that the coercivity of the Co/C_{60} bilayer sample is greatly enhanced in comparison to the samples with a Cu layer separating the Co and C_{60} interface. This enhancement in coercivity can be related to an antiferromagnetic coupling at the Co/C_{60} interface. The magnetic moment of the Co is reduced when

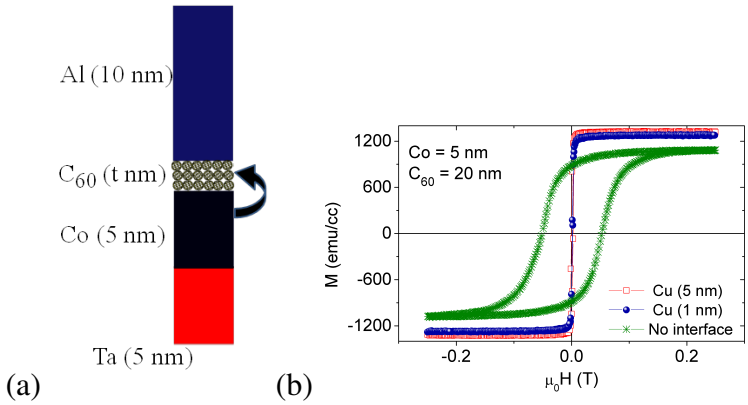

Figure 4.5: *(a) Schematic for a Co/C_{60} bilayer showing the direction of spin polarised electron transfer from the Co into the C_{60}. (b) VSM data at 100 K comparing a Co(5 nm)/C_{60}(20 nm) bilayer to Co(5 nm)/Cu(1 or 5 nm)/C_{60}(20 nm) samples. An enhancement in the coercivity and reduction in the saturation magnetisation is observed when Co is directly in contact with C_{60} compared to when there is a copper spacer layer. Work by Mr Timothy Moorsom, adapted from [46].*

Co is directly in contact with C_{60} compared to when the Cu interlayer is present. This suggests the spin doping effect is interfacial and an increase in thickness of the Cu interlayer further quenches this effect [46].

4.3 C_{60} as an under layer for spin valves

In this section, results on the use of C_{60} as an under layer for Cu based spin valves will be presented and analysed. The samples in this section of the chapter were made ex-situ, before the thermal evaporation source was added to the sputter deposition system. In this case, the C_{60} layers were deposited via thermal sublimation in an evaporation chamber and then moved to a separate sputter deposition system to deposit the metallic layers. At this point in the research no other groups had published results on organic spin valves where the metal layers were sputter deposited, so we were unsure whether this technique would lead to success or whether the C_{60} would be damaged by such an energetic deposition of top electrodes. Since then, C_{60} based spin valves have been successfully deposited by myself [34] and by Zhang et al [3]. Another motivation was to determine how suitable C_{60} was in a wider range of spintronic devices, so we inves-

tigated its use as an under layer for exchange biased spin valves. It was found that C_{60} is indeed a good candidate as an under layer for exchanged bias spin valves [47].

The exchange bias effect is a result of an exchange coupling interaction between the electron spins of ferromagnetic and antiferromagnetic layers [111; 113] as discussed in section 2.1.2. One result of this effect is the shifted hysteresis loop (or the exchange bias field) of the pinned ferromagnetic layer and also an enhancement in coercivity of this layer. This effect has been the basis of many spintronic devices such as spin valves, where the direction of magnetisation of the free and pinned layers can be controlled individually by the application of an external field [113]. A stronger magnetic field and thus more energy is required to reverse the spin orientation in the pinned layer because the antiferromagnetic spins at the interface exert a torque on the ferromagnetic spins [58]. In this research IrMn is used as the antiferromagnetic pinning layer as it is well characterised for these exchange bias systems [114].

The exchange bias effect is dependent on the spin structure of the system. The interfacial spin structure is responsible for the coercivity enhancement and the unidirectional anisotropy [115]. Seed layers are used in spintronic devices in order to facilitate the growth of a particular texture, in this case a face-centred-cubic (fcc) (111) orientation in subsequent Co and IrMn layers and thus the desired magnetic properties. There has been research in recent years into different seed layers (such as Ta, Cu, Cr and CrRu) and varying the thicknesses [116–118]. Some research has investigated using C_{60} as an under layer for NiFe films [19]. Using C_{60} first as a under layer is important if it will work as an effective spacer layer. The magnetic properties must be maintained in the subsequent layers in spin valves and MTJs.

C_{60} films, FeC_{60} films and Ta were deposited as the under layer for spin valves with a Cu spacer layer, with the structure Si/SiOx/under layer/Co/Cu/Co/IrMn/Ta. The C_{60} and Fe were co-evaporated in an evaporation chamber to form FeC_{60} films. Figure 4.6a shows the XRD measurements of films of C_{60} and FeC_{60} of the same thickness (85 nm). Several interference peaks are observed clearly showing small roughness, thus making C_{60} and FeC_{60} suitable as an under layer for spintronic devices. The C_{60} film is smoother than the FeC_{60} film, as shown by the intensity decreasing more rapidly

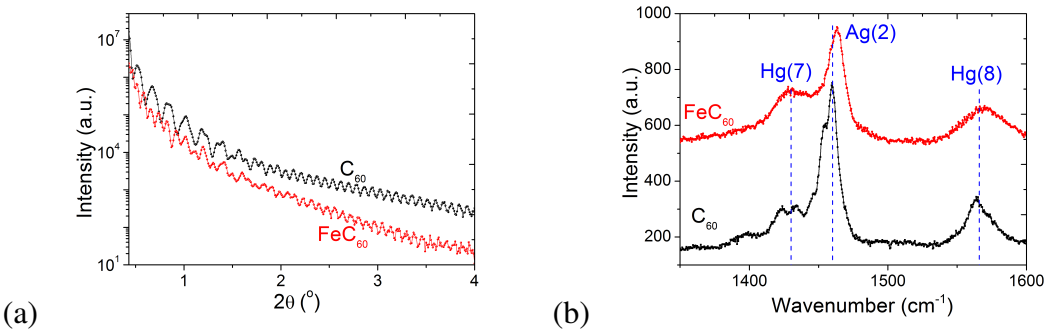

Figure 4.6: *(a) XRR of C_{60} and co-evaporated FeC_{60} 85 nm films showing the intensity of reflected x-rays as a function of detector angle. The drop off in intensity for the FeC_{60} film is greater with increasing detector angle than the C_{60} film implying the FeC_{60} is rougher. (b) Raman spectroscopy of the same C_{60} and FeC_{60} thin films where the peaks shown are characteristic of the C_{60} breathing and pinching vibrational modes; Hg(7), Ag(2) and Hg(8). The candidate's data published in [47]* © *2012 IEEE.*

for the FeC_{60}.

Figure 4.6b shows the Raman spectra of C_{60} compared to the FeC_{60} to characterise the films. The Hg(7), Ag(2) and Hg(8) peaks have different relative intensities and shifts in wavenumber for the C_{60} compared to the FeC_{60} [119]. A shift in the Ag(2) peak of 4 cm^{-1} for the FeC_{60} compared to the C_{60} film may be a result of interfacial interactions and change transfer from the Fe to the C_{60} [120; 121]. Assuming a 6 cm^{-1} shift in the Ag mode per electron transfer to each C_{60} molecule [121], one can approximate on average 0.67 of an electron present on each C_{60} molecule. This suggests that not all the C_{60} molecules experience charge transfer.

MOKE magnetometry measurements were carried out on spin valves with different under layers and the data was analysed. Figure 4.7 shows a normalised MOKE measurement on C_{60}/Co(3 nm)/Cu(2 nm)/Co(3 nm)/IrMn(6 nm)/Ta(5 nm) exchange biased spin valves. The coercivity of the free and pinned layer, and the exchange bias field are labelled for the C_{60}-seeded spin valve measurement. It is apparent from figure 4.8a that the coercivity of the pinned Co layer generally decreases with increasing thickness. This is because the thinner the layer the less energy required to overcome

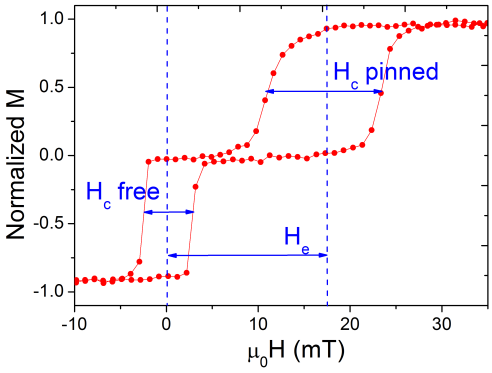

Figure 4.7: *Normalised MOKE magnetometry measurements on a C_{60}(85 nm)/Co(3 nm)/Cu(2 nm)/Co(3 nm)/IrMn(6 nm)/Ta(5 nm) exchange biased spin valve. Here the coercivity of the free and pinned layers, as well as the exchange field are labelled for the C_{60} under layer sample.*

the microscopic torque exerted on the spins of the ferromagnetic layer by the antiferromagnetic layer. The pinned layer coercivity is greater for the C_{60}-seeded spin valves than the Ta-seeded spin valves because there is an enhanced exchange interaction. The observed trend is also different, and it is clear that C_{60}-seeded spin valves can be used to successfully pin thicker Co layers than Ta-seeded spin valves [47].

The exchange field is defined here as the centre magnetic field strength of the pinned magnetisation loop. The exchange field decreases with increasing pinned Co layer thickness. Even for a thick pinned Co layer thickness, the C_{60}-seeded spin valves still exhibit a large exchange field and thus good pinning. Figure 4.8b shows that the exchange field decreases for increased pinned layer thickness which is to be expected. It is proposed that the enhanced exchange bias in the C_{60}-seeded device is not just a result of roughness causing an increase in pinning sites. Instead we suggest the spin structure in the device enhances the exchange bias from 12.5 ± 0.5 mT for a Ta-seeded device to 19.5 ± 0.5 mT for C_{60}-seeded device [47].

C_{60} is beneficial as a under layer because it reduces the amount of non-magnetic metal in the device so the MR could be increased as a result of no current being shunted through this insulating layer. As well as this, carbon bonds with Co and the electrons

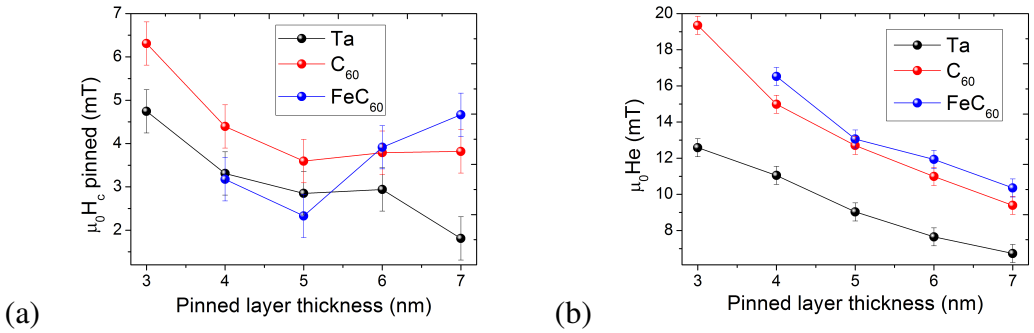

Figure 4.8: *(a) Graph showing the coercivity of the pinned ferromagnetic layer with its thickness for spin valves with either Ta, C_{60} or FeC_{60} as the under layer. (b) Graph showing the exchange field as a function of pinned ferromagnetic layer thickness for spin valves with either Ta, C_{60} or FeC_{60} as the under layer. The device structure is; seed/Co/Cu/Co/IrMn/Ta. The candidate's data published in reference [47] © 2012 IEEE.*

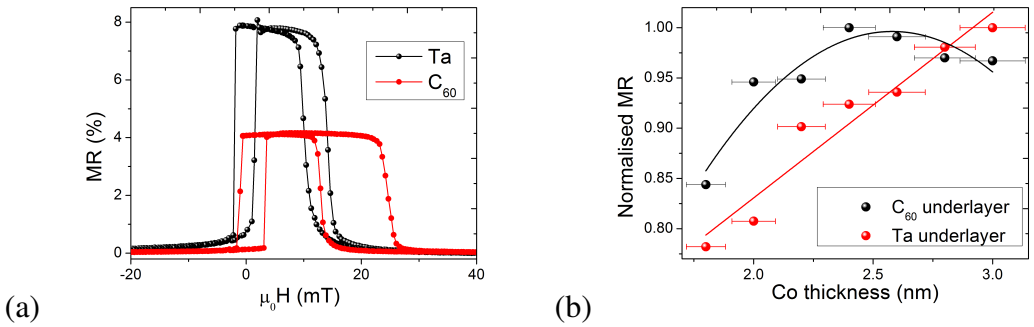

Figure 4.9: *(a) Typical MR measurements through Cu-based spin valves comparing devices deposited on either a Ta under layer, and a C_{60} under layer. (b) Comparison of normalised MR with varied Co free layer thickness for Ta and C_{60} seeded spin valves in order to determine how interfacial effects between Co and C_{60} effect the MR. The lines are to guide the eye.*

hybridise, reducing the number of Co electrons contributing to the current. If this bonding is preferential to unpolarised s electrons, then the total spin polarisation would be increased, further enhancing the MR [122].

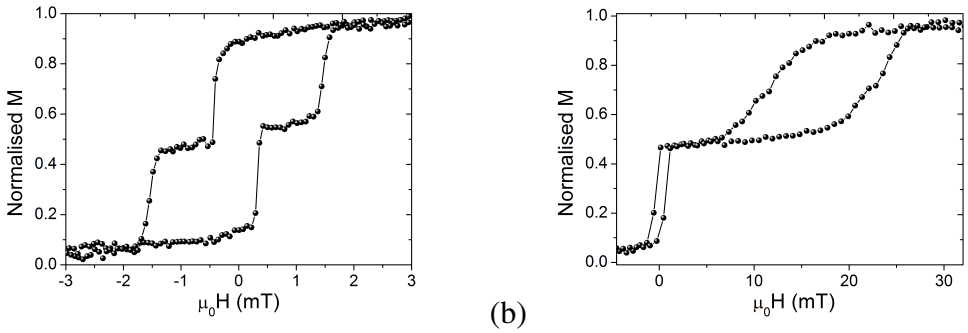

(a) (b)

Figure 4.10: *MOKE data showing the magnetic properties of a C_{60} spin valve with spacer thickness 15 nm with the sample structure (a) Co/Al_2O_3/C_{60}/Py for a spin valve with free ferromagnetic electrodes. (b) Co/Al_2O_3/C_{60}/Co/IrMn for a spin valve with one free and one pinned ferromagnetic electrode.*

Figure 4.9 shows typical current-in-plane MR measurements comparing a Ta and a C_{60} under layer spin valve. These measurements were carried out at room temperature using a current-in-plane four point contact technique. This device shows MR on the same order of magnitude as devices with a Ta under layer. The MR may be reduced for C_{60} under layer spin valves in comparison to Ta under layer spin valves because of increased roughness causing inhomogeneous magnetostatic fields resulting in spin relaxation. It is clear that the relative orientations of the free and pinned ferromagnetic layer switch sharply for both devices with well defined parallel and antiparallel orientations. The thickness of the Co free layer was varied for spin valves with Ta and C_{60} under layers in order to compare the trend of the normalised MR. The MR for the Ta seeded spin valve increases with increasing free layer thickness whereas for the C_{60} seeded spin valve, the MR increases with free layer thickness up to 2.4 nm and then decreases with increasing Co thickness. This suggests interfacial effects between the Co and C_{60} are affecting the spin transport and spin structure in the devices.

Work has been done towards fabricating the first C_{60} spin valve with pinned electrodes with C_{60} spacer layer 15 nm. No MR has been observed in such a stack ($Co/Al_2O_3/C_{60}$ /Co/IrMn) to date, but the MOKE data shows promise. Figure 4.10a shows a C_{60} spin valve with free Co and Py layers as the electrodes ($Co/Al_2O_3/C_{60}/Py$), whereas figure 4.10b shows pinned Co and free Py electrodes where the switching between relative magnetisation states is also clear but not as sharp.

4.4 Conclusion

Hybrid-C_{60} magnetic interfaces have been investigated and characterised. It has been shown that the C_{60} at the interface forms a hybridised state and that there is a transfer of spin polarised electrons from the ferromagnet into the C_{60}. Multilayer samples of C_{60}/Co were deposited in Leeds via thermal sublimation and sputter deposition for the organic and metallic layers respectively, and compared to equivalent samples deposited in the Nanodevices group in NanoGune, where the metallic layers were deposited via electron beam evaporation. One would expect a higher quality of sample when using electron beam evaporation because it is a less energetic process than sputter deposition. However, it was found that the quality of samples is comparable with these deposition techniques, suggesting sputter deposition is indeed a reliable way to deposit such samples. VSM measurements on C_{60}/Co multilayers reveal a transfer of spin polarised electrons from the Co into the C_{60}, thus reducing the magnetic moment of the Co. Functioning exchange biased Cu spin valves have been successfully deposited on top of C_{60} and an enhancement in the exchange bias has been shown. Finally, MOKE measurements on free spin valves and exchange bias spin valves reveal clean switching of ferromagnetic electrodes with a C_{60} spacer layer present. These results lead on to successfully fabricating and measuring spin valves with C_{60} as the spacer layer as shown in chapter 5.

CHAPTER 5

Hybrid-organic spin valves

5.1 Introduction

One of the key areas of interest in spintronics is organic spintronic devices and in particular organic based spin valves. These have successfully been deposited using a range of organic materials as the spacer layer, in which spin polarised electrons can be injected into or tunnel across. Molecules used for this purpose include sexithienyl (T6), CVB (a light emitting π conjugated oligomer $C_{44}H_{36}N_2$), Alq3 (8-hydoxy-quinoline aluminium), rubrene ($C_{42}H_{28}$) and C_{60} [18; 81; 83; 123; 124]. These molecules all possess weak spin orbit interaction and therefore have long spin lifetimes making them beneficial in organic spin valves [1]. In addition to a weak spin orbit interaction, C_{60} also has a weak hyperfine interaction because it does not contain hydrogen [3].

After having successfully deposited functioning copper based spin valves on top of C_{60} underlayers as discussed in chapter 4, the next step was to fully characterise standard Al_2O_3 based magnetic tunnel junctions in order to perfect the insulating barrier layer required for good spin injection into C_{60} [33]. The fabrication procedure for C_{60} based spin valves was then investigated and optimised. In this chapter there will be a comparison of the C_{60} spin valves deposited and measured in Leeds to those produced on my secondment Nanodevices group in NanoGune where the metal layers are deposited by a less energetic process than sputter deposition: electron beam evaporation. TEM on these multilayer samples were shown in chapter 4, and revealed the high quality and lack of interdiffusion in the sputter deposited samples, suggesting this deposition method would be suitable for the deposition of spin valve devices. In the latter part of this chapter C_{60} spin valves which showed asymmetric MR will be analysed. The role of the Al_2O_3 barrier will also be discussed and studied through leaky junctions via point contact Andreev reflection measurements.

5.2 Anisotropic magnetoresistance

The anisotropic magnetoresistance (AMR) effect is the dependence of the resistivity of a ferromagnetic material on the angle between the direction of the magnetisation and the direction of the current flow. This effect was discovered in 1857 by William Thompson [125]. The maximum resistivity occurs when the current flows parallel to

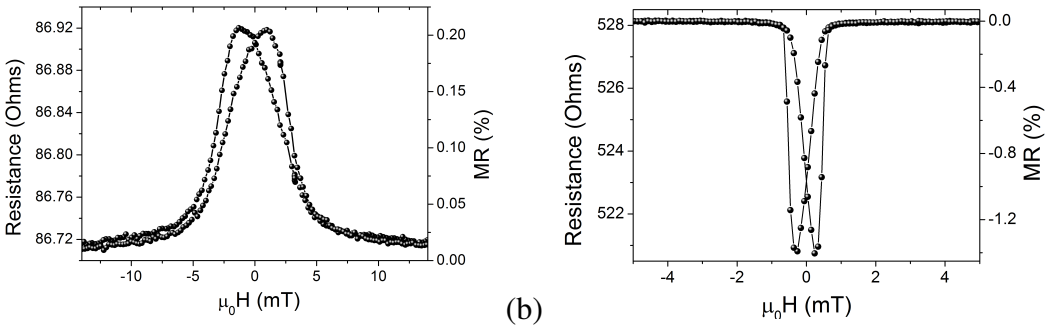

Figure 5.1: *Example resistance with magnetic field measurements at room temperature on (a) a 10 nm Co electrode showing 0.2% AMR where the current direction is parallel to the magnetic field. (b) a 20 nm Py electrode showing 1.4% AMR where the current direction is perpendicular to the magnetic field. The AMR is measured in the same orientation the electrodes would be aligned in a magnetic field during a standard MTJ or spin valve measurement.*

the direction of the magnetisation of the ferromagnet. The magnitude of the AMR can be written as

$$\frac{\Delta\rho}{\rho} = \frac{\rho_{||} - \rho_{\perp}}{\rho_0}, \tag{5.1}$$

where $\rho_{||}$, $\rho_{\perp}$ and ρ_0 represent the resistivity when the magnetisation is parallel to the current, perpendicular to the current and in the demagnetised state respectively. AMR is a result of the spin-orbit interaction between the spin of electrons and the magnetic field of the nuclei [126]. This effect is apparent in some ferromagnetic materials as there is likely to be more s-d scattering for electrons when they travel parallel to the direction of magnetisation [127]. In this process the 4s electrons are scattered by a small unquenched 3d orbital angular momentum. Generally the AMR effect is smaller than GMR or TMR, as shown in figure 5.1a which is an example of a resistance with magnetic field measurement on a Co electrode showing 0.2% AMR. The sign of the AMR is positive for Co when the magnetic field is parallel to current direction (in the transverse orientation). However, the sign of the AMR is reversed when the magnetic field is perpendicular to the current direction across the ferromagnet as shown for Py in figure 5.1b (in the longitudinal orientation). When measuring standard Al_2O_3 MTJs and hybrid organic spin valves one measures the electrodes individually as shown in figure 5.1. This is to ensure the magnetic electrodes are of high quality and the magnetic properties such as the coercivity are as expected. Sometimes a change in the

AMR of an electrode is observed when in contact with C_{60} as shown in section 5.4.

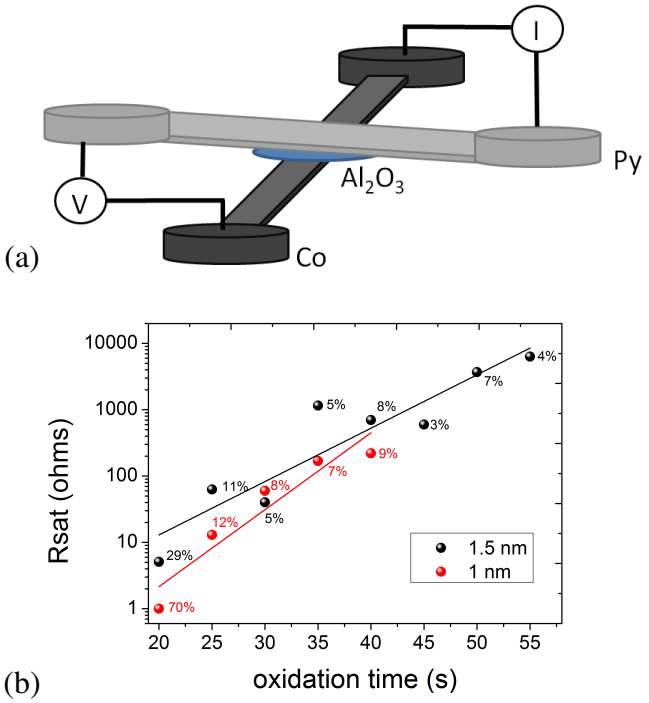

Figure 5.2: *(a) Schematic of an Al_2O_3 magnetic tunnel junction. An Al_2O_3 barrier is sandwiched between a Co(20 nm) and Py(20 nm) electrode. The shadow masking allows a four point measurement in the current perpendicular to plane (CPP) geometry to be utilised. Here either pogo pins, probes or wire bonds can be used to attach to the contact pads. (b) Graph showing the saturation resistance against oxidation time for the Al_2O_3-based tunnel junctions for Al thicknesses of 1 nm and 1.5 nm. Here it is evident that the resistance increases almost exponentially with oxidation time. The percentages marked on the graph refer to the MR value.*

5.3 Al_2O_3 based magnetic tunnel junctions

Although the idea of spin dependent tunnelling was first introduced and measured almost 40 years ago by Julliere [51], the field really began to advance quickly in the 1990s. This advancement was accelerated by improvements in fabrication technology so that routinely depositing good and reproducible tunnel barriers without pinholes became a possibility. One such material used for this purpose is Al_2O_3, and it can be deposited in a variety of ways. Al_2O_3 is beneficial as a tunnel barrier because high

TMR values can be observed [53] and it is relatively easy to make barriers without pinholes as first shown by Moodera et al in 1995 because it is smooth and amorphous [50]. There have been a number of papers studying Al_2O_3 barriers deposited through different methods as discussed in the review in reference [128]. It has also been shown that Al_2O_3 is a good candidate for spin injection into inorganic semiconductors [129] as well as into C_{60} [18]. In this research the Al layer is first grown by DC magnetron sputtering and then oxidised in a mixed O_2 and Ar plasma as discussed in chapter 3.

Al_2O_3 based tunnel junctions were deposited via sputter deposition in a cross hair

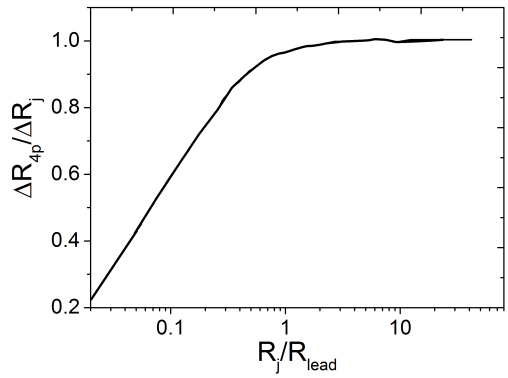

Figure 5.3: *Data taken from [130] showing the scaled resistance change for a magnetic tunnel junction as a function of the ratio of the expected resistance to the lead resistance.*

formation in-situ as shown in figure 5.2a wit h the structure Co/Al_2O_3/Py. The Al thickness and oxidation times were optimised. Other variables include the Ar pressure and O_2 pressure which were kept consistent with previously produced working Al_2O_3 tunnel junctions (by Dr Nick Porter) using the same sputter deposition system. The oxidation time was varied for different Al thicknesses of 1 nm and 1.5 nm. The oxidation time was increased until eventually the MR dropped off, suggesting that the bottom electrode was being oxidised. Ideally the whole Al layer would be oxidised but the electrode would not be. For instance Co oxide is an antiferromagnetic material [111] so the Co becoming oxidised during the fabrication procedure could change the entire functionality of the device. The resistance and therefore RA product increased exponentially with oxidation time. This is to be expected because the oxidation time effectively controls the insulating tunnel barrier height.

The Al_2O_3 MTJs with 25 seconds and lower oxidation time showed particularly large MR values. For instance approximately 70% MR, as shown in figure 5.2b for the 1 nm Al with 20 s oxidation. When the resistance of the barrier is significantly greater than that of the leads and electrodes then the MR will be an accurate measure of the transport through the device. However, for a low resistance junction, when the barrier resistance is comparable or less than the lead resistance, the current distribution is inhomogeneous. There can be current crowding in one corner of the junction giving a false junction resistance. MR is therefore exaggerated in the measurement and this is known as geometrically enhanced MR. In order to correct for this effect one can model the system using finite element analysis approach to determine the current density distribution in a cross-strip geometry [130].

Table 5.1: Estimated corrections for geometrically enhanced MR determined using figure 5.3 [130]. Resistances given are measured in ohms.

Measured MR (%)	R_{4p}	ΔR_{4p}	R_j	ΔR_j	Corrected MR (%)
70	1.0	0.7	20	2.9	15
29	5.3	1.5	39	2.8	7
12	13.0	1.6	36	4.3	12
11	61.0	6.7	82	8.9	11

Here R_{4p} is the measured four probe resistance, ΔR_{4p} is the measured change in four probe resistance between the parallel and antiparallel magnetisation state of the tunnel junction. R_j is the expected resistance of devices below 30 s oxidation time which has been extrapolated from a linear fit to the data above 30 s oxidation time using figure 5.2b. An estimate for the real change in resistance between the parallel and anitparallel magnetisation state of the tunnel junction, ΔR_j, can therefore be extracted from figure 5.3. The MR quoted in figure 5.2b is corrected in table 5.1. It is apparent that the devices with 20 s oxidation time showed a geometrical enhancement in the MR. Here the measured 70% MR is corrected to be 15% and the measured 29% is corrected to be 7%. However, for devices with 25 s oxidation time, the calculated corrected value of MR is the same as the measured, suggesting there is minimal geometrical enhancement once the oxidation time exceeds 25 s.

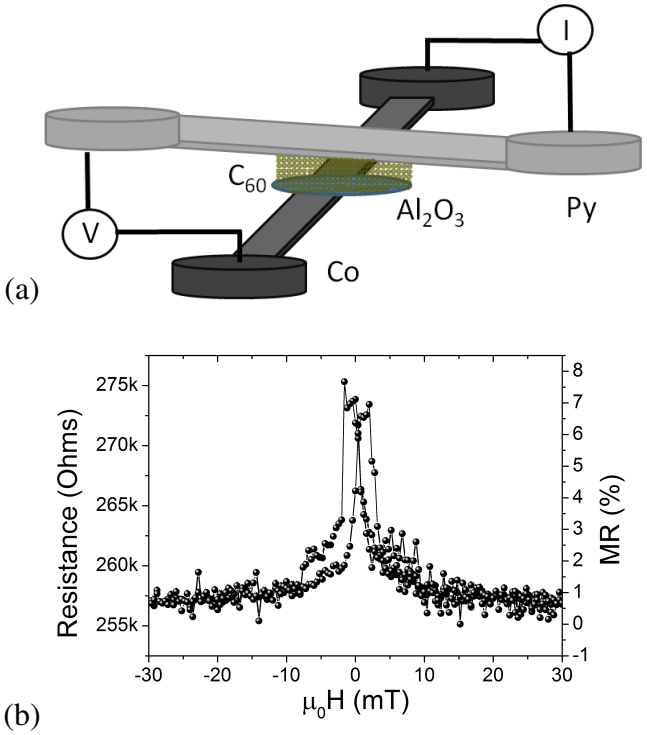

Figure 5.4: *(a) Schematic of a hybrid C_{60} spin valve made using the shadow masking system to form a 100 μm × 100 μm barrier area. Here the C_{60} is sandwiched between a Co(20 nm) and Py(20 nm) electrode. (b) Resistance with magnetic field measurement of a C_{60} spin valve with 20 nm C_{60} spacer layer at room temperature with a 1.2 nm Al_2O_3 barrier.*

5.4 Sputter deposited magnetic electrodes in hybrid C_{60} organic spin valves

Once Al_2O_3 MTJs had successfully been deposited, C_{60} was added between the Al_2O_3 and Py layers. The C_{60} was deposited via thermal sublimation through a 2 mm circular shadow mask to ensure full coverage of the barrier as shown in the sample schematic in figure 5.4a with the structure Co/Al_2O_3/C_{60}/Py. Both the Al_2O_3 barrier and C_{60} have been investigated at length. Figure 5.4b shows a typical MR measurement through a C_{60} spin valve with 20 nm of C_{60}. Here 8% MR is measured at room temperature which is approximately 3% higher than the values seen in similar device structures [18]. This result indicates that the sputter deposition of ferromagnetic electrodes onto C_{60} is a suitable technique for the fabrication of C_{60} based devices.

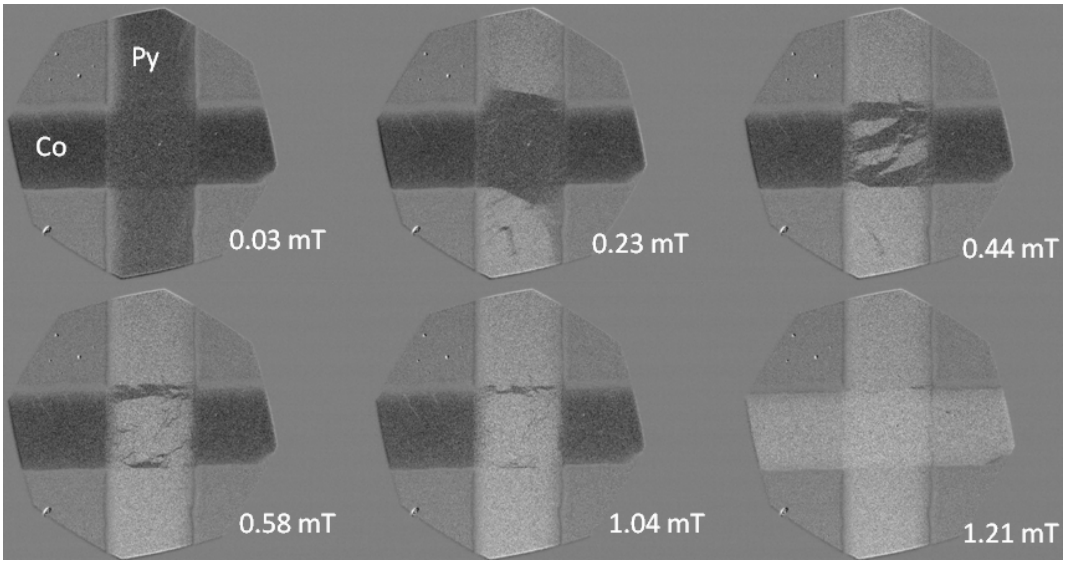

Figure 5.5: *Kerr microscopy images of a C_{60} spin valve. The C_{60}(60 nm) is between the Co(20 nm) and Py(20 nm) electrodes, covering the whole Co electrode observable in these images. Images are taken at a range of magnetic fields to show the parallel and anti-parallel states of the Co and Py electrodes.*

Figure 5.5 shows Kerr microscopy images of a hybrid C_{60} spin valve at different magnetic fields, where the Co and Py electrodes have an overlap of 100 μm $\times$ 100 μm at the barrier. The contrast in the images is related to the change in the orientation of the magnetisation so one can even observe magnetic domains. With increasing magnetic field it is evident that the Py electrode starts to switch first. Parts of the Py electrode switch by 0.23 mT, however at the barrier more field is required to fully switch. By 0.58 mT most of the Py electrode has switched. As the field is increased further the Co electrode switches by 1.21 mT, which happens more quickly, without observable nucleation of magnetic domains. In such measurements there were no noteworthy differences between a standard Al_2O_3 tunnel junction and a a hybrid C_{60} spin valve. This implies that any interesting behaviour in the transport is a result of interfacial effects such as hybridisation and spin filtering. Pinning sites are apparent in the images as a result of structural defects in the sample.

Figure 5.6 shows typical IV measurements through a spin valve with 20 nm of

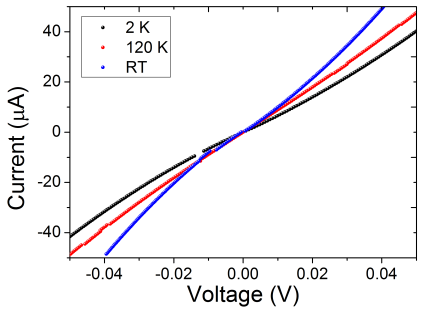

Figure 5.6: *Typical non-linear current voltage characteristics for a hybrid C_{60} spin valve at 2 K, 120 K and room temperature with C_{60} thickness of 20 nm with Py and Co electrodes 20 nm thick.*

C_{60} at 2 K and 120 K. These measurements show non-linear and slightly asymmetric IV characteristics to be expected of such a sample structure. IV measurements were performed with the magnetic electrodes of the device aligned parallel and then anti-parallel so that the MR as a function of current bias can be calculated. Figure 5.7a shows such a measurement, where the MR is higher at lower biases as expected. Standard MTJs have a similar TMR bias dependence and Zhang et al introduced a model to explain it [131]. It was proposed that magnon excitations scatter inelastically at the FM/barrier interface and this determines the voltage dependence. When the voltage bias is greater than zero, the electrons that tunnel across the barrier to the other FM electrode have an energy higher than the Fermi energy of the electrode, assuming no inelastic scattering events have occurred. These electrons lose their energy by emitting a magnon and thus flipping the spin of the electron. Therefore, the greater the voltage bias the more magnons are emitted, thus reducing the MR because more spin flipping processes occur [131; 132]. However, for an organic spacer layer, phonons have an impact on the bias dependence as well as magnons which can be related to the quicker drop off in MR with bias [80]. Figure 5.7b shows data for a C_{60} spin valve with an asymmetric behaviour of the MR with current bias.

Typical resistance as a function of temperature measurements were carried out on a C_{60} spin valve with a thickness of 20 nm as shown in figure 5.8a. The resistance increases as the temperature is reduced which correlates well to the expected phonon-

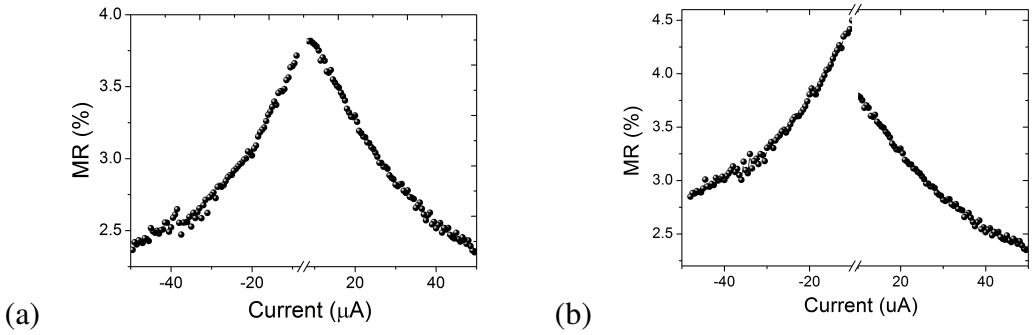

(a) (b)

Figure 5.7: *MR dependence on current bias, showing higher MR at low bias for C_{60} spin valves with Co(20 nm) and Py(20 nm) electrodes and (a) with 20 nm of C_{60}. (b) with 15 nm of C_{60} showing a strong asymmetric dependence of MR on bias. Candidate's data published in reference [34]* © *2014 IEEE.*

assisted tunnelling transport mechanism in the C_{60}. At approximately 90 K there is a change in the gradient of the R vs T measurement as a result of a vibrational mode of the C_{60} being frozen at this temperature. This vibrational mode is the rotational mode of the C_{60} molecule [133].

The MR as a function of temperature was also measured by carrying out resistance with magnetic field measurements at each temperature as shown in figure 5.8b. The MR decreases as the temperature is increased which is typical of such devices with a tunnelling or hopping transport mechanism. The temperature dependence of the MR and resistance cannot simply be attributed to the loss of spin polarisation of the ferromagnetic electrodes with temperature but also resulting from the loss of spin polarisation during transport across the barrier. This is shown by the dependence of the resistance and MR on temperature following the same trend as shown in figure 5.8b. Such a dependence is also observed in other organic spin valve systems, for instance in work by Barraud et al [80].

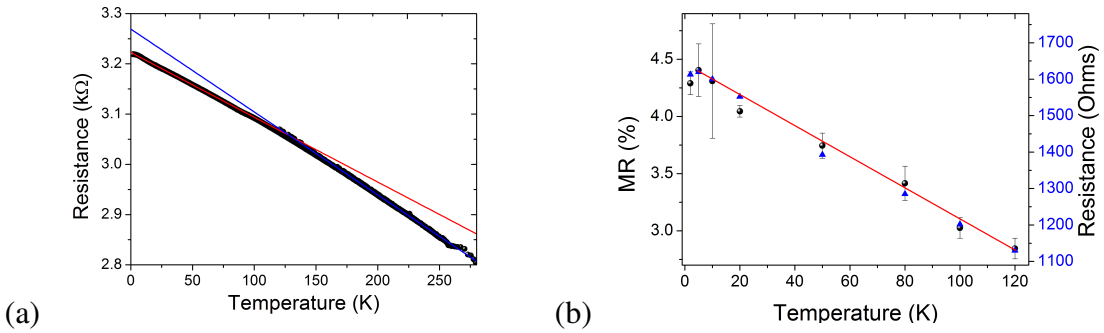

Figure 5.8: *(a) Normalised resistance versus temperature measurement showing the increase in resistance as the temperature is reduced. This is characteristic of tunnelling-like behaviour. A change in temperature dependence at approximately 90 K is observed and may be due to a transition in C_{60}(20 nm) when the rotational vibrational modes become frozen. (b) MR and resistance as a function of temperature for a C_{60}(20 nm) spin valve with 20 nm thick Co and Py electrodes where the line is to guide the eye.*

5.5 Electron beam evaporated metals in hybrid C_{60} spin valves

Figure 5.9a and b shows the MR measurements of a spin valve with 60 nm of C_{60} as the spacer layer. Here an asymmetry in magnetic field is observed, where the resistance is higher in the negative field parallel alignment of ferromagnetic electrodes compared to the positive field parallel alignment. These measurements were carried out at 10 K in a cryostat filled with liquid He. This asymmetry in magnetic field cannot be explained without considering interfacial effects. The hybridisation of the C_{60} with the ferromagnetic electrodes is perhaps coupling antiferromagnetically creating an additional layer of magnetic material which requires an extraordinarily large magnetic field to switch. The field required to switch this layer is beyond 6 T, the field which can be applied during the measurement. This asymmetry varies with bias direction across the junction, for instance on application of a positive bias to the top electrode one observes a depletion in the spin injection. This increases the MR because the interface scattering events are lowered. Higher MR is observed when electrons flow from the bottom electrode with the Al_2O_3 barrier. The spin injection also changes the spin polarisation of the ferromagnet which will affect the MR [34].

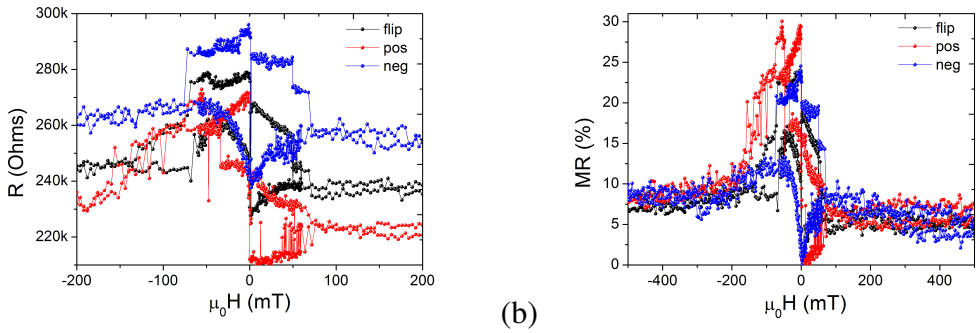

Figure 5.9: *Magnetotransport measurements of a C_{60} spin valve with 60 nm of C_{60} measured at 10 K. Here the current bias is either reversed, positive or negative. (a) Resistance with magnetic field measurement. (b) MR with magnetic field. There is asymmetry observed in the positive and negative saturated magnetic fields as well as a function of bias direction. Candidate's data published in reference [34]* © *2014 IEEE.*

Hybrid organic spin valves with the structure Co/Al_2O_3/C_{60}/Py were deposited in the Nanodevices group at NanoGune in Spain, where the metals were deposited via electron beam evaporation and the C_{60} deposited via thermal sublimation. The samples were deposited in an ultra high vacuum (UHV) dual chamber evaporator with a base pressure of 10^{-9} mbar. The Al was first deposited via electron beam evaporation and then oxidised in the load lock chamber in an O_2 plasma at 10 mA and at 10^{-1} mbar for a range of times. Figure 5.10 shows the device geometry of the C_{60} spin valves and reference magnetic tunnel junctions. Here there are five Co strips, an Al_2O_3 barrier covering the whole device and C_{60} covering three of the Co strips. The Py top electrode is deposited in a strip perpendicular to the Co electrodes. Here there are five devices that can be measured individually. The two devices without C_{60} can act as reference junctions.

Organic spin valves with 20 nm of C_{60} and 0.9 nm of Al were deposited in which the Al was oxidised to form Al_2O_3. The times used were 20, 50 and 100 seconds. Samples with 100 s oxidation time showed no MR in the C_{60} devices and less than 1% in the reference devices suggesting the Co electrode beneath the barrier was oxidised at the interface thus greatly reducing spin transport. The C_{60} MTJs with 20 s oxidation

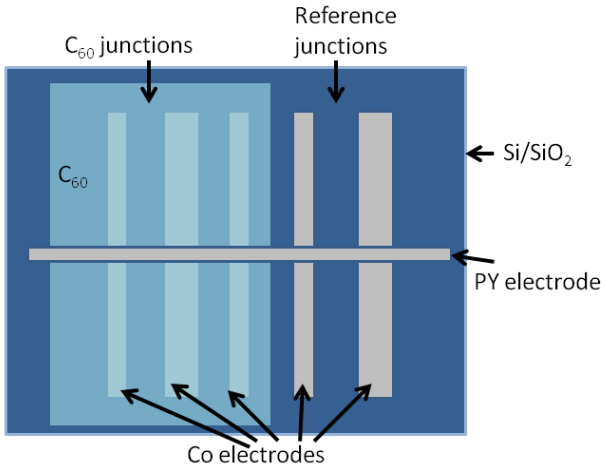

Figure 5.10: *Device geometry for C_{60} magnetic tunnel junctions and reference junctions. The device has five bottom Co electrodes. An Al layer was deposited all over and then plasma oxidised to form Al_2O_3. C_{60} was deposited on three of the electrodes so the other two are reference devices. A Py top electrode was then deposited in a strip perpendicular to the Co electrodes. The junction areas range from 200 x 200 μm to 200 x 500 μm.*

time showed approximately 2% MR but no MR was observed through the reference junction suggesting a very leaky Al_2O_3 barrier. In an attempt to further optimise these devices an oxidation time of 50 s was used and the MR through 20 nm of C_{60} was found to be 12% at room temperature. The reference junctions showed different characteristics even with the same oxidation recipe, some showed no MR and others with up to 5.5% MR with a range of resistances from one device to another. This suggests the oxidation method is not reproducible and can vary even on the same substrate where there are 2 reference junctions and three C_{60} junctions grown in-situ.

Figure 5.11 shows a typical magnetotransport measurement on a reference device with no C_{60}. Here 5.5 % MR is observed but it is to be noted that the equivalent C_{60} junction on this device showed approximately 15 % MR. If the Al_2O_3 barrier was not leaky then one would expect the MR to be reduced only due to the presence of C_{60}. However, it almost triples in this case when there is 20 nm of C_{60} present. A possible explanation for this is that the C_{60} hybridises with the ferromagnetic electrode and acts as a spin filter, thus enhancing the MR.

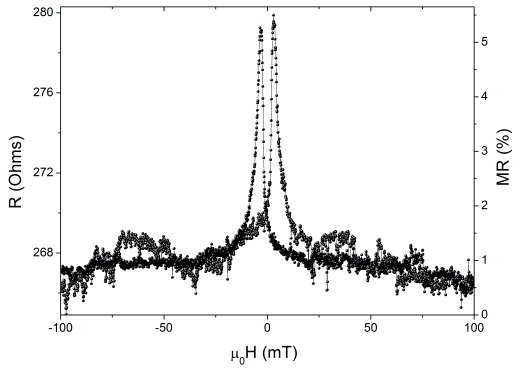

Figure 5.11: *Room temperature magneto-transport measurement on a reference tunnel junction with the structure Co(20 nm)/Al_2O_3/Py(20 nm) (with no C_{60}) where 5.5 % MR is observed. Here the metallic materials were deposited via electron beam evaporation.*

Figure 5.12 shows the resistance with magnetic field characteristics through the C_{60} spin valves. It is evident for both 10 nm and 20 nm of C_{60} that the resistance increases with decreasing temperature which is indicative of tunnelling-like or hopping transport and there is a broadening of the antiparallel state related to an increase in magnetic coercivity with decreasing temperature.

Figure 5.12c and d show MR measurements at a range of temperatures through C_{60} spin valves with 10 nm and 20 nm thickness. Here the MR at room temperature is 9 % for the spin valve with 10 nm of C_{60} and 11 % for the spin valve with 20 nm of C_{60}. The shape of the MR measurements for the C_{60} spin valve with 10 nm of C_{60} is smooth, implying a lack of pinning sites. In contrast the C_{60} spin valve with 20 nm of C_{60} shows stochastic or step-like RH characteristics similar to measurements by Gobbi et al from NanoGune [18]. One explanation for this is an increase in magnetic pinning sites as a result of increased roughness with more C_{60}.

Figure 5.13 shows the MR as a function of current bias, determined by carrying out I-V measurements in the parallel and antiparallel orientations of the magnetic electrodes. Similar characteristics are observed for the 10 nm C_{60} sample and the 20 nm

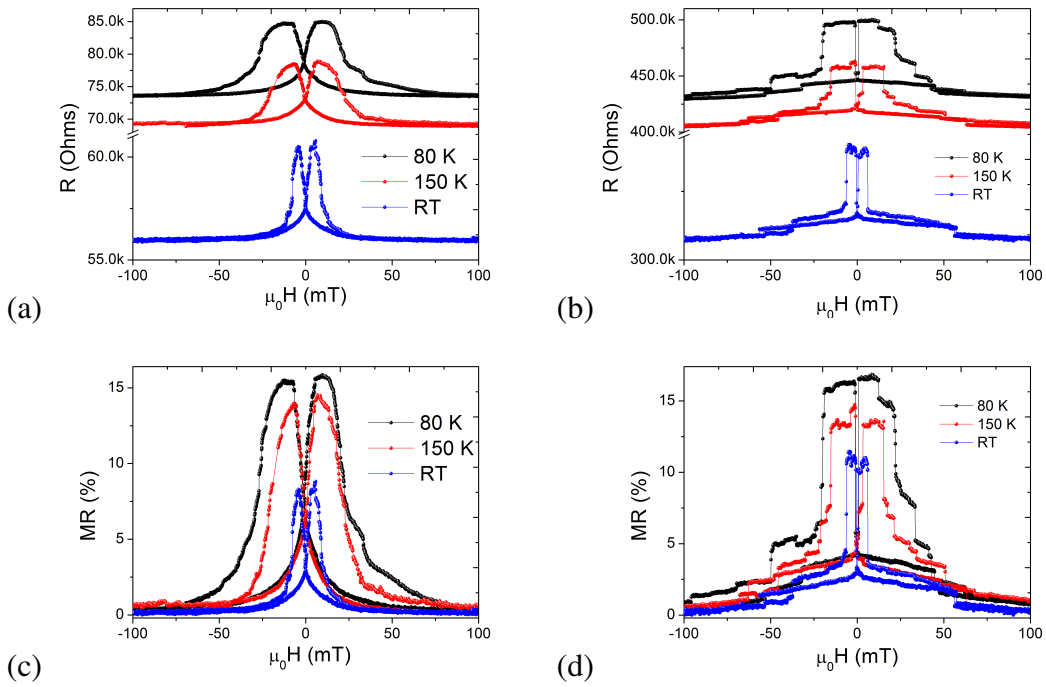

Figure 5.12: *Magnetotransport measurements on C_{60} spin valves at a range of temperatures for (a) 10 nm of C_{60} and (b) 20 nm of C_{60}. Here the structure is Co(20 nm)/Al_2O_3/C_{60}/Py(20 nm). It is apparent that the resistance across the devices increases as the temperature is reduced, as expected from tunnelling-like behaviour. MR as a function of magnetic field at different temperatures on C_{60} spin valves with the structure Co(20 nm)/Al_2O_3/C_{60}/Py(20 nm) for (c) 10 nm of C_{60}. (d) 20 nm of C_{60}. The MR values are similar for the samples of different C_{60} thickness, however the 20 nm C_{60} sample shows stochastic or step-like changes in resistance, unlike the 10 nm C_{60} sample.*

C_{60} sample. At low bias (0.01 V) the MR is about 15% and reduces by a few percent by 0.1 V. The MR dependence on voltage bias is asymmetric because of the asymmetric structure of the sample. The MR is higher when the electrons move from the Co electrode through the Al_2O_3 barrier and into the C_{60} rather than the other way round. This suggests the Al_2O_3 barrier is present to allow easy spin injection into the C_{60}.

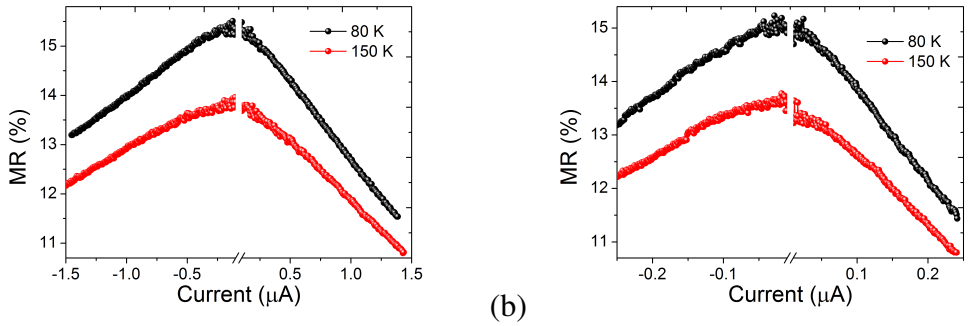

Figure 5.13: *MR as a function of voltage bias at different temperatures on C_{60} spin valves with (a) 10 nm of C_{60}. (b) 20 nm of C_{60}.*

5.6 Point contact Andreev reflection experiments on C_{60}

In this section there will be a discussion of the methods developed to investigate the spin polarisation of C_{60} or a ferromagnetic material in contact with C_{60}. The first of which is the PCAR technique using a leaky junction, where there are pinholes through the barrier, to measure the spin polarisation of a ferromagnetic electrode adjacent to thin layers of C_{60}. Secondly, the standard PCAR technique in which a superconducting tip can be moved into contact with a thin ferromagnetic film with C_{60} on top. This tip penetrates through the C_{60} layer to measure the spin polarisation of the ferromagnetic material. Finally I will briefly show results working towards carrying out Meservey-Tedrow measurements in a superconducting/insulating/C_{60}/ ferromagnetic (S/I/C_{60}/FM) junction in which the spin polarisation in the C_{60} can be measured directly. However, this final method requires temperatures well below the critical temperature of the superconductor (in this case AlSi), and for the samples to remain pinhole free after loading process into the adiabatic demagnetisation refrigerator, which turns out to be a significant challenge. Improvements to this final technique are a work in progress. An additional motivation for this work is that the mechanism behind spin injection into C_{60} remains elusive and the role of the insulating Al_2O_3 barrier, whether the devices are optimised with a leaky [18] or a good tunnel barrier [33], is yet to be fully understood.

The superconducting properties of $Al_{0.98}Si_{0.02}$ thin films were characterised as

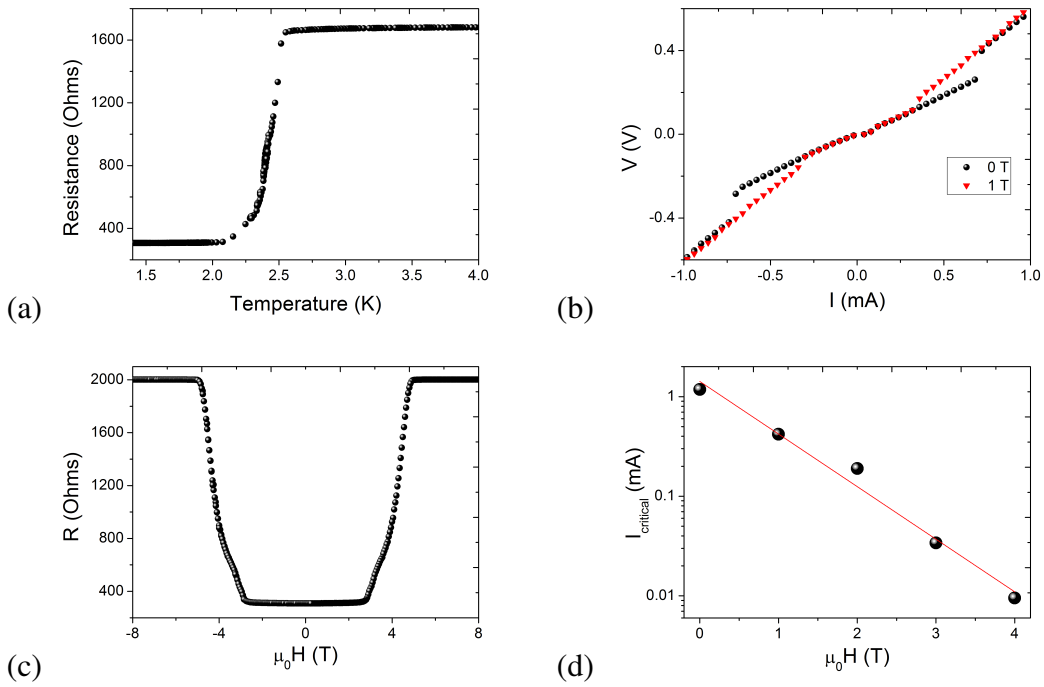

Figure 5.14: *Transport measurements on an AlSi electrode (8 nm) where (a) shows typical resistance with temperature measurement, here the superconducting critical temperature is 2.4 K. (b) shows typical current-voltage characteristics to show the critical current at 0 T to be 0.8 mA and reduced to 0.3 mA at 1 T. (c) Resistance with magnetic field showing AlSi (8 nm) to be fully superconducting up to 2.5 T. (d) Relationship between critical current and critical magnetic field.*

shown in figure 5.14 where we present typical critical temperature, magnetic field and current measurements in $Al_{0.98}Si_{0.02}$. $Al_{0.98}Si_{0.02}$ is a type II superconductor so it has a higher critical temperature than typical type I superconductors. Type I superconductors are perfect diamagnets and therefore expel any external magnetic field. However, type II superconductors allow the penetration of magnetic field which is required for Meservey-Tedrow measurements as discussed later in this section. The superconducting critical temperature lies between 2.2 and 2.4 K as shown in figure 5.14a. The resistance below the critical temperature is non-zero because of the resistance of the measurement leads. At 0 T the critical current is 1.0 mA as shown in figure 5.14d. The critical field at low bias is approximately 4 T. The metallic layers were deposited via DC magnetron sputtering and the $Al_{0.98}Si_{0.02}$ was plasma oxidised partially to form an

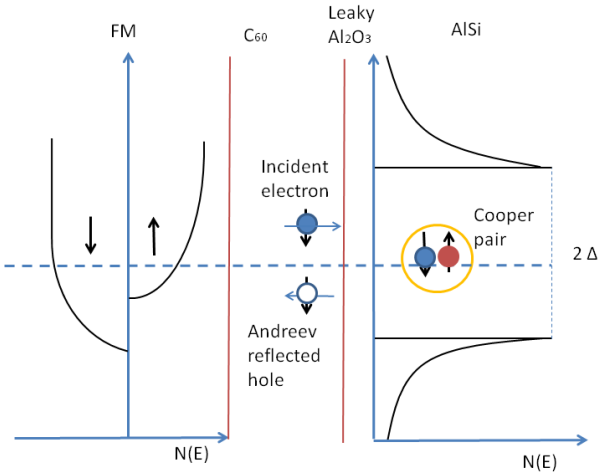

Figure 5.15: *Schematic diagram representing the Andreev reflection process on conversion of a normal current into a superconducting current at the AlSi. The sample structure is FM/C_{60}/leaky Al_2O_3/AlSi.*

Al_2O_3 barrier.

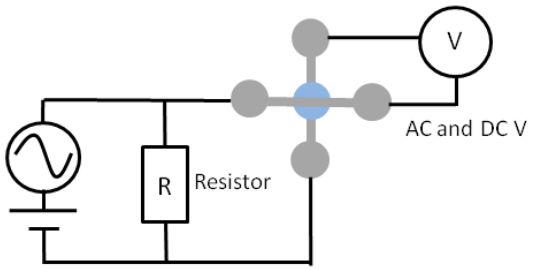

Figure 5.16: *Circuit diagram of AC/DC four point contact differential conductance measurements on a junction for PCAR measurements. Here an AC signal is superimposed on a DC signal. The AC and DC signal can be measured back using a lock-in amplifier and a voltmeter to determine the differential conductance measurement as a function of voltage bias across the device.*

In order to fully understand the transport through devices in the literature where the Al_2O_3 layer is leaky we deposited an insulating layer with pinholes. Thus Andreev reflection is observed at biases within the superconducting energy gap and below the superconducting critical temperature [61]. Figure 5.15 is a visual representation of the

energy levels of the samples with the leaky tunnel barrier and C_{60} adjacent to it. This schematic diagram shows the Andreev reflection mechanism at the AlSi layer on conversion of normal to supercurrent. The formation of Cooper pairs in the AlSi is limited by the spin polarisation of the normal current at the interface. In these samples, the spin polarisation in the ferromagnet is the limiting factor because the C_{60} is discontinuous at the thicknesses used. Spin doping occurs from the ferromagnet into the C_{60} and the aim of these measurements is to further quantify the spin doping effect.

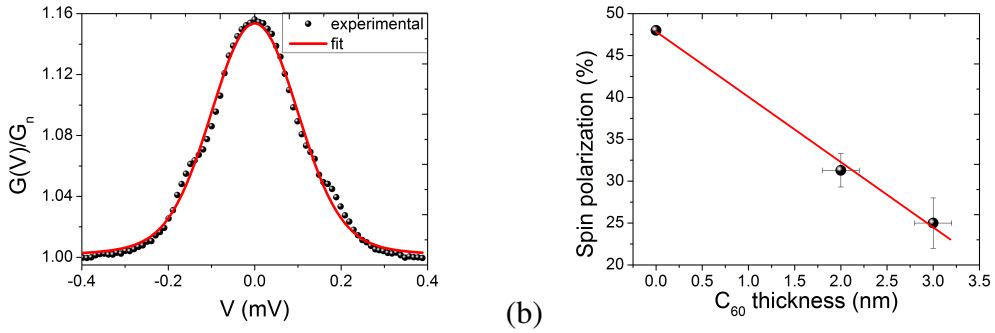

Figure 5.17: *(a) PCAR measurement in an AlSi(8 nm)/C_{60}/Py junction with 2 nm of C_{60}. Here the differential conductance is measured as a function of voltage bias. (b) Spin polarisation as a function of C_{60} thickness showing the spin polarisation in the Py reduce as the C_{60} thickness is increased.*

To measure this limitation on the Cooper pair formation, the differential conductance across the junction is measured as shown in the circuit diagram figure 5.16. An AC/DC lock-in technique is required. An AC signal is superimposed on a DC bias using a Keithley 6221 source meter. A Keithley 2182a nanovoltmeter is used to detect a DC voltage and a lock-in is used to detect the AC voltage. A standard resistor can be added and selected such that a high percentage of the current is shunted through the resistor rather than the sample. This allows us to use the Keithley 6221 as a current source for smaller step sizes.

Point contact Andreev reflection data was taken at 1.4 K and fitted to extract the spin polarisation of the Py in contact with C_{60} as shown in figure 5.17. The parameters used in this fitting are the superconducting energy gap of AlSi, the smearing parameter

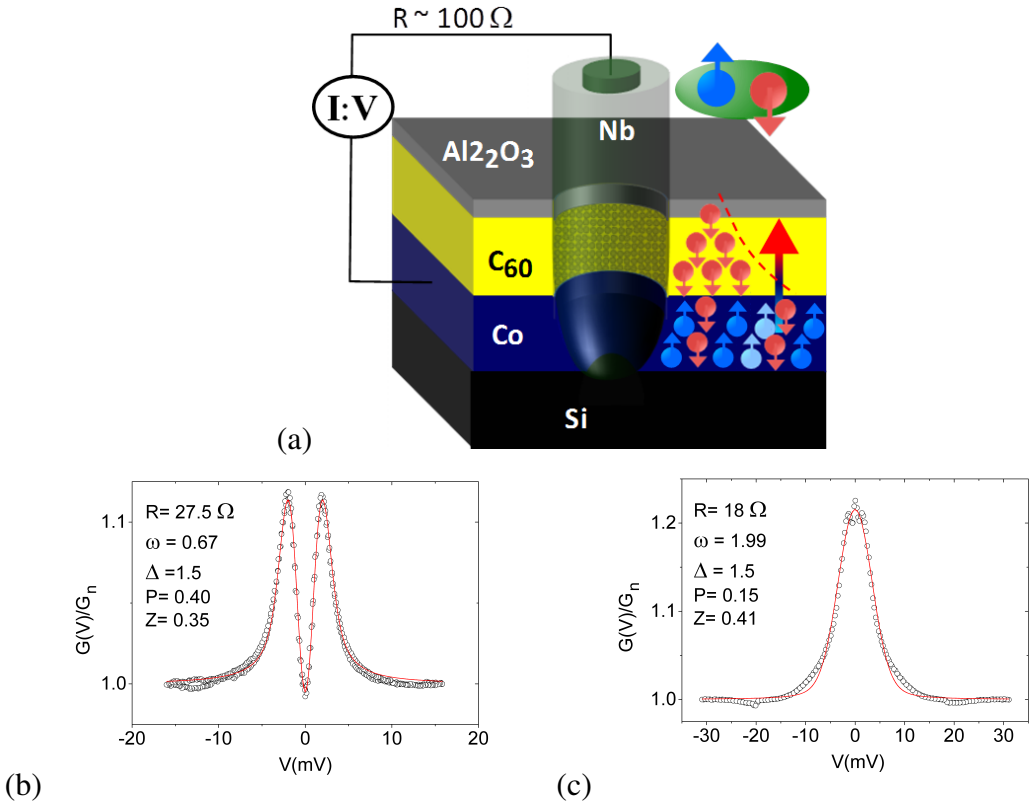

Figure 5.18: *(a) Schematic diagram of a superconducting Niobium tip being moved into contact with C_{60}/Py. Example normalised PCAR data with BTK model fit to extract the spin polarisation for (b) Co and (c) Co/C_{60}. Fitting parameters are included on the graphs. Work by Ms Fatma Al Ma'Mari taken from reference [34]* © *2014 IEEE.*

and the barrier parameter. The data has been fitted using the modified BTK model as discussed in chapter 2 and the spin polarisation of the Py in contact with 2 nm of C_{60} was extracted to be $(31 \pm 2)\%$ from the measurement shown in figure 5.17a. An AlSi/Al_2O_3/C_{60}/Py junction with 3 nm of C_{60} was also measured and fitted giving a spin polarisation of $(25 \pm 3)\%$. The spin polarisation in a Py thin film without C_{60} is 48% [134]. This result shows a significant reduction in the spin polarisation of Py as shown by its dependence on C_{60} thickness from figure 5.17b, suggesting spin polarised electrons are being transferred into the C_{60}. Such thicknesses of C_{60} will be discontinous and therefore leaky allowing this PCAR technique to be utilised. C_{60} of greater thicknesses may not be leaky, thus these measurements were not carried

out for thicker samples. This leads towards work on performing Meservey-Tedrow measurements where the barrier is pinhole free.

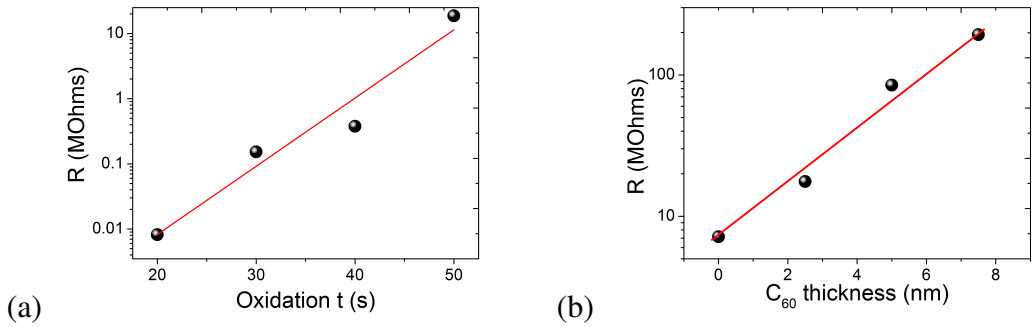

Figure 5.19: *(a) Resistance with oxidation time through AlSi/Al_2O_3/Py junctions. (b) Resistance as a function of C_{60} thickness through AlSi/Al_2O_3/C_{60}/Py junctions. The resistance increases exponentially as a function of oxidation time and C_{60} thickness.*

To confirm the reduction in magnetic moment of Co when in contact with C_{60} as discussed in chapter 4, other techniques were utilised. For instance PCAR can be used to measure the spin polarisation of a material using a superconducting point contact as shown in the schematic in figure 5.18a. The limitation on Cooper pair formation due to an imbalance of up and down spin electrons can be measured via conductance measurements at the point contact [61]. These measurements were performed in a cryostat filled with liquid He by moving a superconducting wire (a thinly cut tip of Nb) into contact with a ferromagnetic thin film.

A large number of measurements were carried out to build up a reliable statistical average of the spin polarisation as presented by Al Ma'Mari et al [34]. Figure 5.18b and c shows example PCAR data with fits to the BTK model for Co and Co/C_{60} respectively. The spin polarisation for Co was found to be $40 \pm 1\%$ whereas the spin polarisation for Co in contact with C_{60} was found to be $30 \pm 1\%$. Thus a reduction of 10% spin polarisation was observed in Co as a result of the transfer of spin polarised electrons from the Co into the C_{60}. These results correlate well with the conclusions drawn from magnetometry, PNR and XMCD measurements [46].

The next plan was to perform Meservey-Tedrow measurements on AlSi/Al_2O_3/C_{60}/ Py junctions in order to directly measure the spin polarisation in the C_{60}. This technique utilises splitting of quasi-particle states of AlSi (type II superconductor) in the presence of a magnetic field to determine the spin polarisation of the metal in a superconducting -insulating-metallic junction [135–138]. The conductance characteristics as a function of voltage bias in a large magnetic field (typically 2 T) can be used to determine the spin polarisation. The resistance of devices with varying oxidation time and C_{60} thicknesses were measured and characterised as shown in figure 5.19.

Figure 5.20 can be used to understand the Meservey-Tedrow technique for measuring the spin polarisation [138]. Here a superconducting-ferromagnetic tunnel junction can be considered where (a) shows the density of states of the superconductor in relation to voltage and how it is modified in a magnetic field. The conductance is modified differently depending on whether the electrons are up spin or down spin as apparent in figure 5.20b. Figure 5.20c reveals a theoretical conductance measurement to show the up spin, down spin and total conductance across a superconducting-ferromagnetic-metal tunnel junction. The spin polarisation of the ferromagnetic material or whatever material is on the other side of the barrier, i.e. superconductor/barrier/X, can be determined from the total conductance measurement.

The aim was to use this Meservey-Tedrow method to reveal the tunnelling spin polarisation in different thicknesses of C_{60}, where preliminary data is shown in figure 5.21. Here the normalised conductance is measured as a function of voltage to reveal tunnelling-like characteristics up to 4.5 T. These measurements were carried out at 1.4 K, which is too close to the critical temperature of the AlSi to observe change in conductance as a result of the quasiparticle splitting. A number of samples were measured in an adiabatic demagnetisation refrigerator that can be cooled and stabilised to 80 mK. However, these samples did not survive the process of loading. The resistance of the devices would drop, suggesting pinholes in the samples. To solve this problem the electronics of the sample stick are being improved.

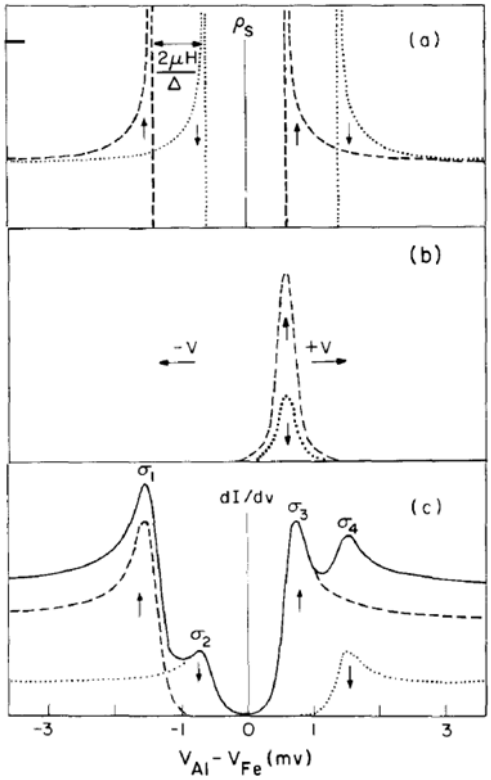

Figure 5.20: *Superconducting-ferromagnetic tunnel junction. (a) BCS density of states of a superconductor with voltage and its modification in a magnetic field. (b) Temperature dependent kernels for up spin and down spin electrons in the integral expressions for conductance. (c) Normalised theoretical conductance for up spin and down spin electrons (dotted and dashed curves) and the total conductance (solid line). Taken from [138].*

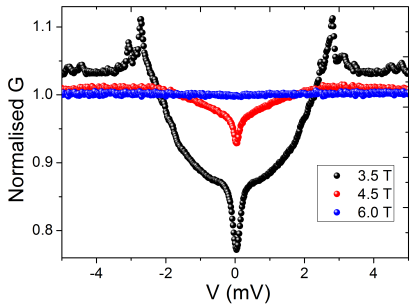

Figure 5.21: *Normalised conductance with bias through a AlSi/Al_2O_3/C_{60}/Py junction showing tunnelling-like characteristics up to 4.5 T.*

5.7 Conclusion

We have been able to deposit and measure hybrid organic spin valves with C_{60} as the active spacer layer that show MR. This was done by first optimising standard tunnel junctions with an Al_2O_3 tunnel barrier before adding a C_{60} layer. Devices made in Leeds were compared to those deposited in the Nanodevices group in NanoGune where the key difference between devices is that the metallic layers are deposited by electron beam evaporation rather than sputter deposition. The samples from both yielded some similar results although the role of the Al_2O_3 layer in such junctions was not certain. It was however found that these devices are particularly unstable and degrade with the application of large bias currents. This degradation under bias stress is well known in organics and has been discussed by Sirringhaus in relation to organic field effect transistors [9]. Therefore, rather than continuing to investigate and perfect these devices we studied the barrier and spin polarisation in the C_{60} layer as well as the affect the C_{60} has on the spin polarisation of the magnetic layer. Through PCAR measurements we found that spin doping occurs in the C_{60}: the movement of spin polarised electrons from the ferromagnetic material into the C_{60}. The mechanisms behind spin transport and spin injection into organics are not fully understood, and perhaps further research in such devices could lead to advances in the field in general. One such method that will be used in the future to measure the spin polarisation in the C_{60} is the Meservey-Tedrow technique.

CHAPTER 6

Ferromagnetic resonance on C_{60}/magnetic bilayers

6.1 Introduction

Ferromagnetic resonance is a useful tool to understand magnetic properties of materials, in particular magnetisation dynamics as discussed in sections 2.7 and 3.2.7. The parameters one can extract from such measurements are the resonant frequencies, linewidths, effective magnetisation and damping parameter. The continuing drive for smaller, more efficient and faster systems, particularly the latter, leads to an increasing interest in techniques such as ferromagnetic resonance which probes systems in the GHz scale. In this chapter the magnetisation dynamics will be determined and compared for a range of samples, namely C_{60}/Py, C_{60}/Co and C_{60}/YIG systems. Here it is evident that the presence of C_{60} impacts the magnetic properties of the ferromagnetic materials.

6.2 Effect of a C_{60} interface on the effective magnetisation of ferromagnetic materials

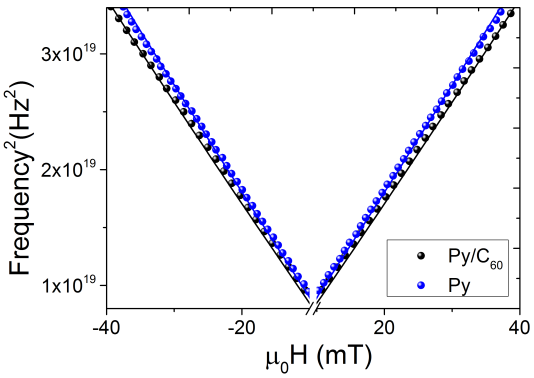

Figure 6.1: *Position of resonance peaks in frequency as a function of magnetic field, extracted from Lorentzian fits to the power absorption through the waveguide. The Kittel equation has been fitted to the data for Py compared to C_{60}/Py.*

The effective saturation magnetisation M_{eff} can be extracted from the fit of ferromagnetic resonance data to the Kittel equation (equation 3.5) as described in section 3.2.7. Frequency sweep measurements were carried out at each magnetic field step

and Lorentzian peaks were fitted to the resonance peaks. From the fit one can extract the peak position in frequency as a function of field. This was performed for a range of samples deposited on oxidised silicon substrates: C_{60}(30 nm)/Py(20 nm)/Al(5 nm), C_{60}(30 nm)/Al(3 or 5 nm)/Py(20 nm)/Al(5 nm), C_{60}(30 nm)/Al_2O_3(2 nm)/Py(20 nm)/Al(5 nm) and Py(20 nm)/Al(5 nm). The Kittel equation (equation 3.5) can then be fitted to the resonant frequency position as a function of field, as shown in figure 6.1, to extract the M_{eff} where the line is the Kittel fit.

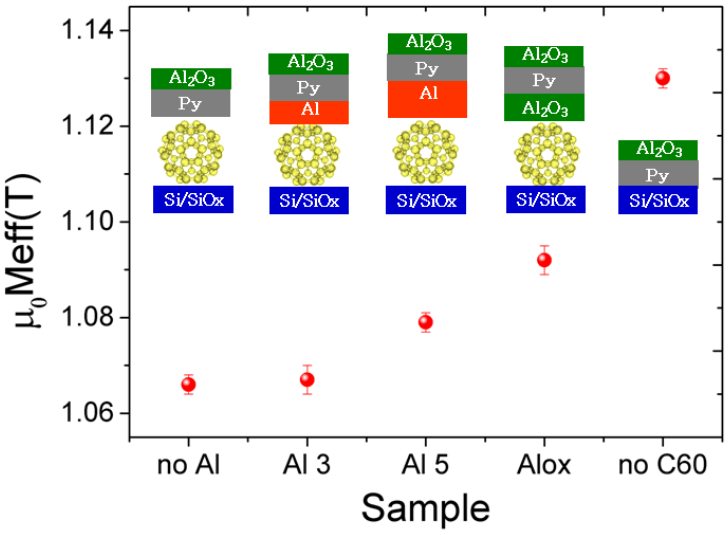

Figure 6.2: *Change in effective magnetisation taken from the fit to the Kittel equation for Py compared to Py in contact with C_{60}, as well as with Al or AlOx between the Py and C_{60}. The thickness of the Al is given in nm. Al(3-5 nm) or AlOx between the Py and C_{60}. Sample schematics are given on the figure. All samples are then capped with 3 nm of Al that will oxidise to form AlOx.*

The sample structure was designed so that one could compare the M_{eff} of Py to that of Py with a C_{60} interfacial layer, and whether adding a metallic or insulating spacer between the Py and C_{60} would quench any effects. It was found that M_{eff} is reduced for Py when in contact with C_{60}, which is apparent in figure 6.2. This is related to the spin doping effect, where there is spin polarised charge transfer from the Py to the C_{60} resulting from the differences in chemical potential and orbital hybridisation as shown by Moorsom et al [46]. When comparing Py to C_{60}/Py, an 8% reduction in M_{eff} is

observed. This percentage change is comparable to the change in spin polarisation observed in PCAR data of leaky junctions as shown in chapter 5. Figure 6.2 shows that the addition of an Al or Al_2O_3 layer between the C_{60} and Py reduces this spin doping effect. The effective magnetisation is a volume property but is clearly affected by the presence of C_{60} which is an interfacial effect that extends some distance into the on the same order as the exchange length. One would therefore expect the effective magnetisation of thinner Py to be reduced further. Unfortunately this dependence on thickness is yet to be studied thoroughly.

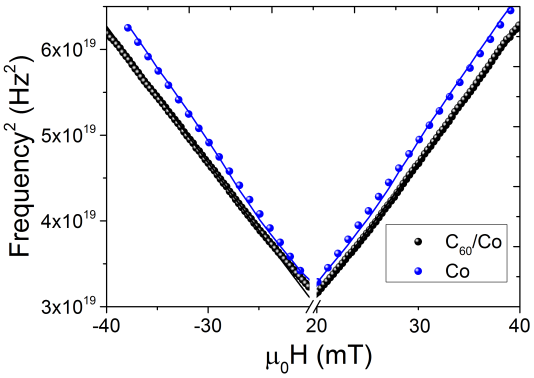

Figure 6.3: *Position of resonance peaks in frequency as a function of magnetic field, extracted from Lorentzian fits to the power absorption through the waveguide. The Kittel equation has been fitted to the data for Co compared to C_{60}/Co.*

Similarly to Py, these frequency sweep FMR measurements were carried out on Co(20 nm)/Al(5 nm) and C_{60}(30 nm)/Co(20 nm)/Al(5 nm) as shown in figure 6.3. M_{eff} was found to be 2.06 T for Co and 1.96 T for C_{60}/Co, thus a 5% reduction with the addition of a C_{60} layer. This suggests there is spin doping from the Co into the C_{60}, in good agreement with the observations made in Py.

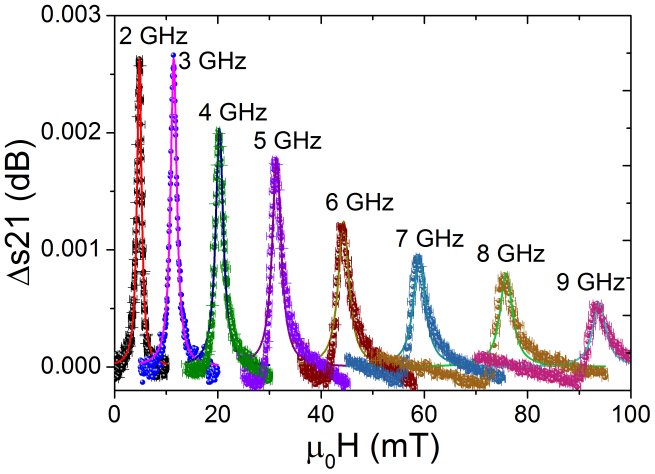

Figure 6.4: *Magnetic field sweeps at different frequencies on a C_{60}(30 nm)/Py(20 nm)/Al(5 nm) sample. The change in transmission through the waveguide is measured (Δ s21) and this parameter has been fitted with a Lorentzian function (lines) to extract peak position and linewidth.*

6.3 Effect of a C_{60} interface on the damping of ferromagnetic materials

A key area of interest in this research is the mechanism in which power from a ferromagnetic material at FMR dissipates into an adjacent C_{60} layer. To understand this mechanism, the energy damping occurring at the interface between the ferromagnet and C_{60} during ferromagnetic resonance must be investigated. The Gilbert damping (as discussed in sections 2.7 and 3.2.7) determines the change in linewidth as a function of resonant frequency and can thus be extracted from such measurements.

To determine the damping parameter, magnetic field sweep measurements were performed at different frequencies. Lorentzian peaks were then fitted to this data to extract the full width half maximum or linewidth of the resonant peaks. Figure 6.4 shows the field sweep measurements at different frequencies for the sample C_{60}(30 nm)/Py(20 nm)/Al(5 nm) and it is apparent that the linewidth increases with increasing frequency. It should be noted that the change in amplitude of the resonant peaks at

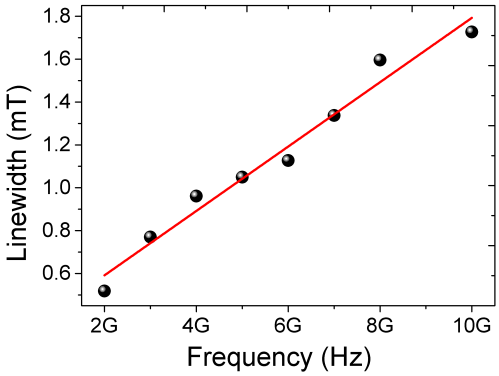

Figure 6.5: *Variation of the linewidth of C_{60}(30 nm)/Py(20 nm)/Al(5 nm) sample as a function of frequency, with a linear fit (red line). The linewidth increases with increasing frequency.*

different frequencies is dominated by the power losses through the waveguide. Figure 6.5 shows the linewidth as a function of frequency with a linear fit. From the gradient of this fit, the damping parameter is extracted using equation 3.4.

To determine the power dissipation mechanism from the Py into the C_{60}, a range of samples with different interfacial coupling can be measured. Similar magnetic field sweep measurements were performed at different frequencies for the C_{60}/Py, Py and C_{60}/Al(X)/Py samples to compare the linewidths and damping parameter. Introducing an Al or Al_2O_3 layer between the Py and C_{60} will quench the spin wave propagation as well as the spin dependent electron transfer into the C_{60}. With the presence of these interfacial layers, the power dissipation of the ferromagnet is dominated by injection and propagation of phonons into the C_{60}.

Figure 6.6 shows the change in the damping parameter for the different Py and C_{60}/Py samples extracted by fitting equation 3.4 to the linewidth as a function of frequency data. On comparison of the Py and C_{60}/Py sample directly, the Gilbert damping is enhanced by 50% with the addition of the C_{60} layer, implying that spin waves and phonons are being transferred into the C_{60}. The damping parameter enhancement is reduced on addition of the Al_2O_3 interfacial layers by approximately 30% as a result of the injection of spin waves being quenched. This suggests that more than just spin

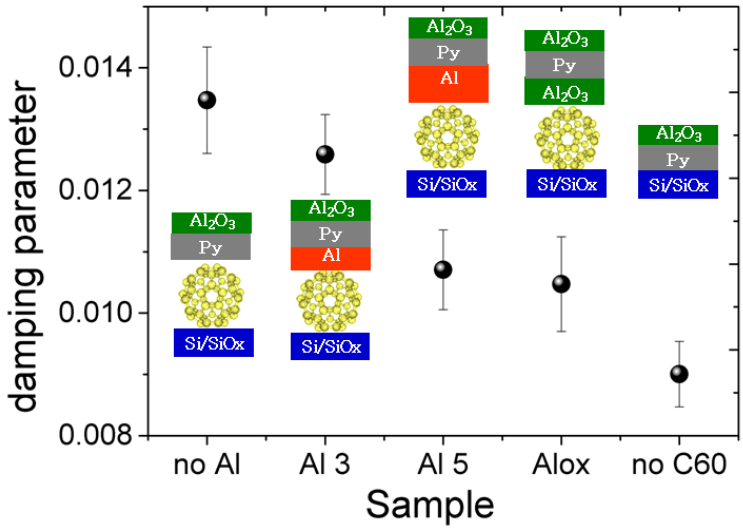

Figure 6.6: *Change in Gilbert damping of Py(20 nm) compared to Py(20 nm) in contact with C_{60}(30 nm) and with Al(3-5 nm) or AlOx between the Py and C_{60}. Sample schematics are given on the figure. Here the damping is enhanced by 50% when Py is in contact with C_{60}.*

pumping is responsible for the enhancement in damping. This could be attributed to phonon injection as discussed in chapter 7.

One can directly compare the linewidth at a particular frequency of different samples in order to determine the nature of the dissipation or the spin pumping. For instance, figure 6.7 shows field sweep data at 3 GHz comparing a Py(20 nm) sample to two different C_{60}/Py(20 nm) samples with 15 nm and 30 nm of C_{60} respectively. From the Lorentzian fit to this data the linewidth can be extracted and it is shown to be 1.46 mT for Py and 1.51 and 1.50 mT for the C_{60}/Py samples with 15 and 30 nm of C_{60} respectively. This is a 3% increase in the linewidth, suggesting that there is spin pumping from the Py into the C_{60}.

Typically the transfer of angular momentum from a ferromagnet to a normal metal generates a spin current. Additional damping is exerted on the magnetisation precession of the ferromagnet as a result of the coupling between the ferromagnet and normal metal. Thus the linewidth is enhanced, and this enhancement determines the spin mixing conductance at the interface [139]. The spin pumping can be considered

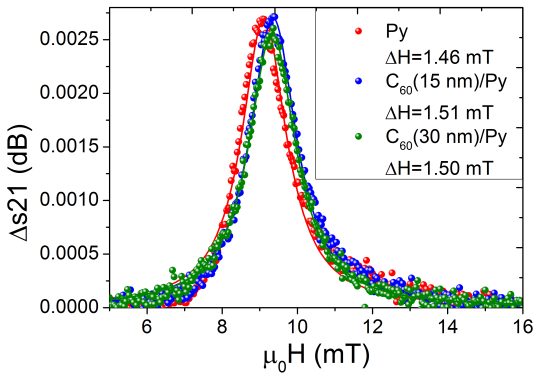

Figure 6.7: *Field sweep measurements at 3 GHz comparing the linewidth of Py(20 nm) and C_{60}(15 or 30 nm)/Py(20 nm) samples.*

in a similar way for a ferromagnetic/organic interface. The spin mixing conductance $g_{eff}^{\uparrow\downarrow}$ can be determined using

$$g_{eff}^{\uparrow\downarrow} = \frac{4\pi M_{eff} t_F \Delta\alpha}{g\mu_B}, \tag{6.1}$$

where t_F is the thickness of the ferromagnetic material and $\Delta\alpha$ is the change in damping parameter between the ferromagnetic material with and without the adjacent C_{60} layer. From the spin mixing conductance one can determine the efficiency in which spins are pumped into the C_{60}. The spin mixing conductance was found to be 5.49 $\times$ 10^{19} m^{-2} for a C_{60}/Py interface using the FMR measurements from a C_{60}/Py/Al sample and a Py/Al sample. This value for the spin mixing conductance are on the same order of magnitude in comparison to typical magnetic/normal metal interfaces [140; 141].

Field sweep measurements were also carried out on Co(20 nm) and C_{60}(30 nm)/Co(20 nm) samples as shown in figure 6.8 and 6.9. The Lorentzian function can be fitted to each peak in order to extract the linewidth as a function of frequency as shown in figure 6.10.

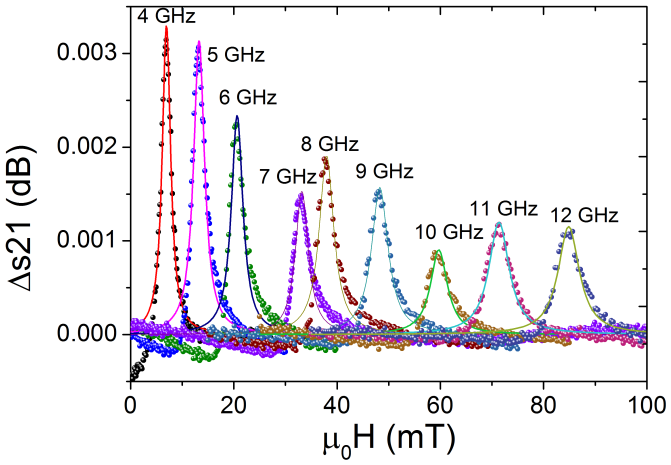

Figure 6.8: *Magnetic field sweep measurements at different frequencies for Co (20 nm)/Al(5 nm). The change in transmission through the waveguide is measured (Δ s21) and this parameter has been fitted with a Lorentzian function (lines) to extract peak position and linewidth.*

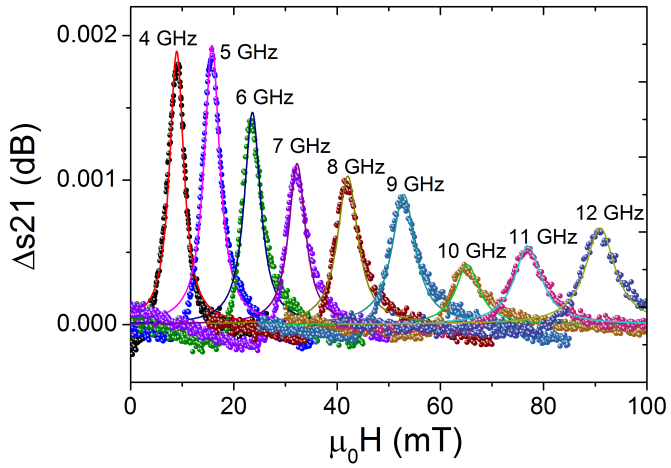

Figure 6.9: *Magnetic field sweep measurements at different frequencies for C_{60}(30 nm)/Co(20 nm)/Al(5 nm). The change in transmission through the waveguide is measured (Δ s21) and this parameter has been fitted with a Lorentzian function (lines) to extract peak position and linewidth.*

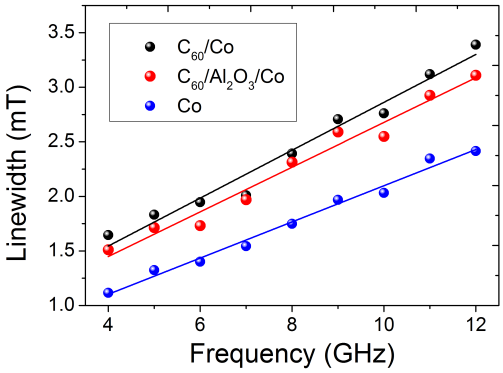

Figure 6.10: *Linewidth as a function of frequency comparing Co(20 nm), C_{60}(30 nm)/Co(20 nm) and C_{60}(30 nm)/Al_2O_3/Co(20 nm). The data has been fitted to extract the damping parameter.*

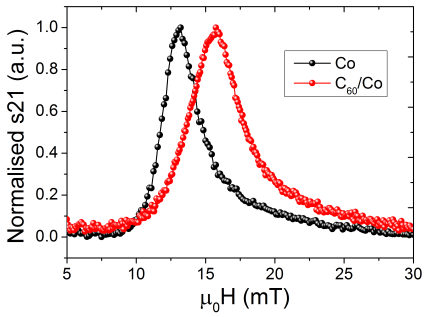

Figure 6.11: *Field sweep measurements at 5 GHz on Co(20 nm) and C_{60}(30 nm)/Co(20 nm) samples to show the increased linewidth in the C_{60}/Co sample.*

The linewidths of Co and C_{60}/Co samples have been compared at a range of frequencies. Figure 6.11 shows field sweep measurements at 5 GHz where the linewidth for the Co sample is 1.3 mT, whereas the C_{60}/Co sample is 1.8 mT. This is a 38% enhancement in the linewidth at this frequency. This change is significantly larger than when comparing the Py and C_{60}/Py samples, perhaps suggesting greater coupling between C_{60} and Co and more spin pumping in comparison to phonon-injection.

Equation 3.4 was used to determine the damping parameter of the Co from the gradient of the linewidth with frequency data. Similarly to the Py samples, the Gilbert

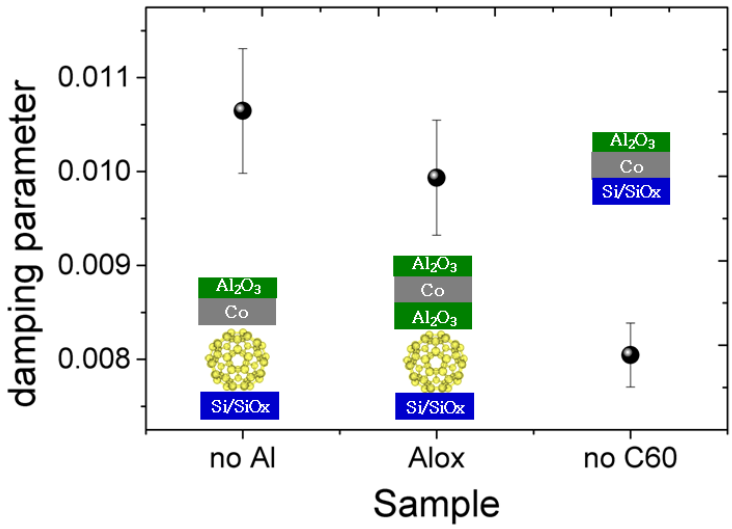

Figure 6.12: *Change in Gilbert damping of Co(20 nm) compared to Co(20 nm) in contact with C_{60}(30 nm) and with Al or AlOx between the Co and C_{60}. Here the damping is enhanced by 35% when Co is in contact with C_{60}.*

damping of the Co is enhanced by 35% with the addition of a C_{60} layer as shown in figure 6.12. Adding an Al_2O_3 layer between the Co and C_{60} reduced this effect. Using equation 6.1, the spin mixing conductance was found to be $5.81\times\ 10^{19}$ m^{-2} for a C_{60}/Co interface, which is on the same order of magnitude in comparison to typical magnetic/normal metal interfaces [141].

The enhancement in damping of both Py and Co when in contact with C_{60} indicates that there is spin pumping into the C_{60} when these ferromagnetic materials are at FMR. There have been no published reports of this in the literature to date so this is a significant result.

6.4 Magnetisation dynamics of YIG with a C_{60} interface

Yttrium iron garnet (YIG) is of great interest in this research because it has very small magnetic damping and it is an insulating ferrimagnetic material so one can expect

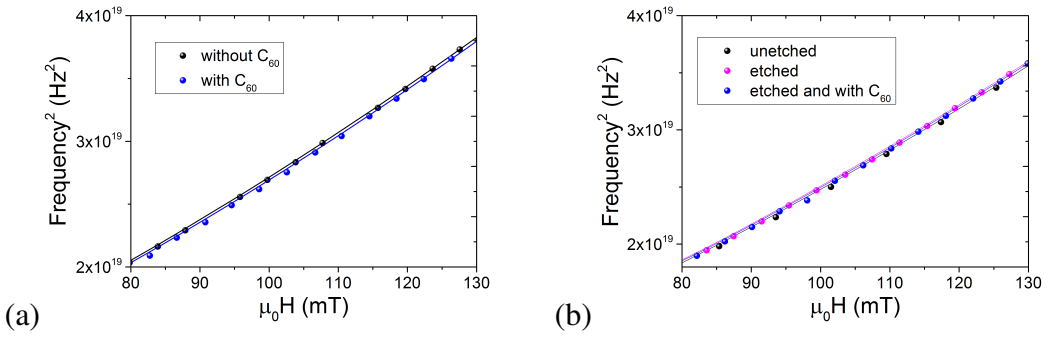

Figure 6.13: *Frequency of resonant peaks as a function of magnetic field with the Kittel fit (lines) comparing (a) unetched YIG with and without C_{60} (b) unetched YIG, etched YIG and etched YIG with C_{60} deposited on top.*

there to be no charge transfer but still spin pumping effects [48]. The YIG used in this research was grown by Mr Scott Marmion, Dr Mannan Ali and Ms Arpita Mitra via RF sputtering in a mixed argon/oxygen atmosphere in a pressure of 2.4 mTorr as described in reference [142]. The YIG was deposited onto (111) gadolinium gallium garnet (GGG) substrates, because they have similar lattice constants of 12.38 Å the same crystal structure and similar thermal expansion coefficients [143; 144]. The as-deposited YIG was not magnetic, however after annealing for 2 hours at 850 °C the YIG becomes ferrimagnetic. FMR measurements were carried out before the annealing process and no signal was observed, however after the annealing process resonance peaks were measurable.

Frequency sweep measurements were carried out at different magnetic fields and Lorentzian peaks were fitted to extract the peak position in frequency. These peak positions in frequency were plotted against the corresponding magnetic field as shown in figure 6.13 to compare YIG with and without C_{60}. YIG of 40 nm thickness was measured before and after etching as well as with and without the deposition of C_{60} and the effective magnetisation was extracted for each. Figure 6.13b is the measurement of the YIG before and after ”piranha” (a mixture of hydrogen peroxide and sulphuric acid) etching to remove a possible ”dead layer”. It is uncertain what this ”dead layer” consists of but it could be an oxidised layer or an Fe rich layer. This measurement shows a small enhancement in the effective magnetisation after this etching process as

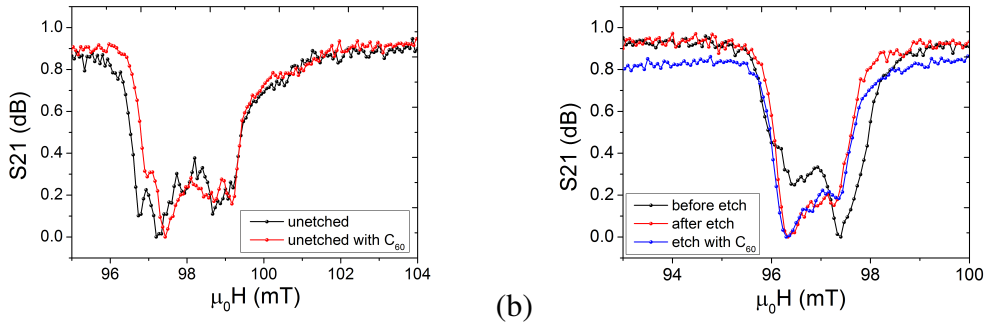

(a) (b)

Figure 6.14: *Field sweep measurements at 5 GHz for (a) unetched YIG(40 nm) with and without C_{60}(30 nm) (b) YIG(40 nm) before etching, YIG after etching and YIG after etching with C_{60}(30 nm).*

given in table 6.1. Perhaps this etching process removes magnetic inhomogeneities at the interface, however, the change is relatively small (1.6%). When C_{60} is deposited on top of this etched YIG the effective magnetisation is reduced by 0.8%. The effective magnetisation is also reduced by 1.2% for the unetched YIG when C_{60} is deposited on it. A change in effective magnetisation for YIG with/without an adjacent C_{60} layer had not been expected because there should not be charge transfer or spin doping from the YIG into the C_{60} as YIG is an insulator. One explanation could be oxidation when the YIG is exposed to atmospheric conditions and dead layer formation at the YIG interface causing changes in effective magnetisation. There could be conducting Fe impurities at the interface and therefore spin polarised charge transfer from the YIG into the C_{60}. This would explain why there is a larger change in effective magnetisation on addition of the C_{60} for the unetched YIG.

Multiple resonances have been observed in the YIG films as shown in figure 6.14, similar to those observed in YIG films grown by pulsed laser deposition [145]. These additional resonance modes can be attributed to inhomogeneities in the film or to standing spin wave resonances (SSWR). The fact that these additional resonances have not disappeared when the YIG was etched suggests if there are inhomogeneities, that they either may not all be at the interface, or that the etching process has not been fully optimised. The addition of C_{60} to the YIG films does appear to affect the field sweep measurements, although not significantly, for instance in figure 6.14a and 6.14b. The

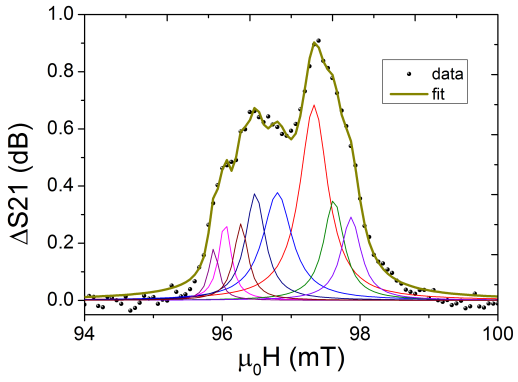

Figure 6.15: *Change in transmission through the waveguide (Δ s21) as a function of magnetic field at 5 GHz on 40 nm of unetched YIG showing multiple Lorentzian fits to the multiple resonance peaks. Here there are up to 8 apparent resonance peaks.*

etching process appears to affect the position of the multiple resonances as is apparent in figures 6.14 and 6.15 which perhaps implies some of the inhomogeneities at least lie at the interface. The inhomogeneities could be across the area of the film as a result of varying thickness or roughness. The change in shape of resonances appears to be impacted more on deposition of C_{60} for the unetched sample compared to the etched sample as shown in figure 6.14. These changes could suggest conducting Fe impurities at the interface because they are more pronounced for the unetched YIG which is likely to have more of a ”dead layer” than the etched YIG.

Field sweep measurements were carried out at a range of frequencies on the unetched and etched YIG with and without C_{60} deposited on top. The multiple peaks made the linewidth analysis particularly difficult. To achieve a good fit to the data, one had to assume the presence of up to 8 different peaks as shown in figure 6.15. Figure 6.16 shows the linewidth found by fitting a single peak to each field sweep measurement as a function of frequency. This clearly is not a fair representation of the damping but can give some indication of it. Figure 6.16a shows the unetched YIG measurement with and without C_{60} whereas figure 6.16b shows YIG before and after etching and with C_{60} on the etched YIG. The damping parameter was found from the gradient of figures 6.16a and 6.16b. The biggest change in the damping is between

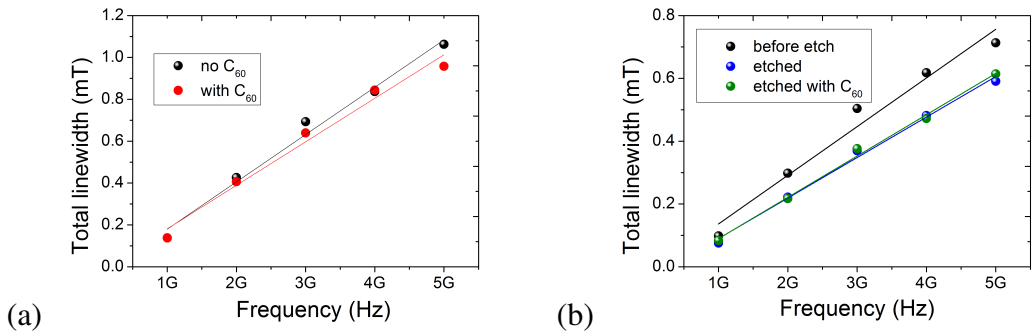

Figure 6.16: *Total linewidth as a function of frequency for (a) unetched YIG(40 nm) with and without C_{60}(30 nm) (b) YIG(40 nm) before and after etching and with C_{60}(30 nm) on etched YIG.*

the unetched and etched YIG as given in table 6.1. There is a very small change observed in the damping of the YIG with C_{60} added which could mean there is no spin pumping into the C_{60} from the YIG, suggesting the damping mechanism is different at the insulator/C_{60} interface. Perhaps there is some spin pumping but it is too small to observe clearly. The same experiment could be carried out on thinner YIG and maybe we would observe more of an impact on the damping from the interface. The other reason for no change in the damping could be because the total linewidth is not a true representation of the damping and that the multiple peaks must be considered individually. To further understand the YIG/C_{60} samples these experiments would need to be repeated on YIG where there are no multiple peaks.

Table 6.1: Effective magnetisation and damping parameter comparing YIG samples before and after etching as well as with and without C_{60}.

Sample	μ_0 Meff (T)	Error (T)	Damping parameter	Error
unetched 1	0.2385	0.0002	0.011	0.001
unetched 1 with C_{60}	0.2357	0.0002	0.010	0.001
unetched 2	0.2415	0.0006	0.0075	0.0007
etched 2	0.2455	0.0003	0.0063	0.0003
etched 2 with C_{60}	0.2436	0.0003	0.0064	0.0002

6.5 Conclusion

It was shown via FMR that the effective magnetisation of Py and Co is reduced when directly in contact with C_{60} by 8% and 5% respectively. This implies that spin polarised electrons are being transferred from the C_{60} into the ferromagnet as a result of charge transfer because of different chemical potentials. This result is corroborated by PCAR and VSM data as discussed in chapter 4. As well as this, a change in the damping parameter of Py and Co when in contact with C_{60} has been observed. The damping parameter is enhanced by 50% and 35% respectively for Py and Co which implies there is spin pumping from the ferromagnet into the C_{60}. Not only do we propose that there is spin doping and spin pumping, but that there is also phonon injection from the ferromagnet into the C_{60}. This is suggested because the addition of an interfacial Al_2O_3 layer should hinder the spin pumping significantly, yet the damping parameter of C_{60}/AlOx/Py is larger than that of Py. This leads us to believe there is more than standard spin pumping contributing to the enhancement in damping. It is not clear whether spin pumping into C_{60} via FMR follows typical accepted theories of spin pumping into metals. To determine the mechanism of damping, we use electron transport, Raman spectroscopy and photoluminescence simultaneously with FMR to probe the C_{60} as shown in chapter 7. To separate effects of spin polarised charge transfer from spin pumping we also deposited C_{60} on YIG and performed FMR measurements with/without C_{60}. There was little change in the effective magnetisation of the YIG which was to be expected because it is insulating so that there should be no charge transfer from the YIG into the C_{60}. There was also little change in the damping, however the data was difficult to analyse properly because there were many multiple resonance peaks probably resulting from inhomogeneities. To continue with such experiments and reliably determine the changes in damping parameter, the YIG quality must be reproducibly good, with significantly less inhomogeneities.

CHAPTER 7

Vibrational manipulation of C_{60}

7.1 Introduction

An enhancement in the damping of the precession of the magnetisation of Py during FMR when in contact with C_{60} compared to that of Py on its own was observed, as discussed in chapter 6. In order to determine the nature of the damping mechanism and what is responsible for such an enhancement, one must probe the C_{60} layer to observe transport, vibrational and photoluminescent properties. Firstly, simultaneous FMR-transport measurements have been used to determine whether the conductivity through C_{60} could be manipulated by an adjacent electrode at resonance. Enhancement in the conductivity of C_{60} could be attributed to phonon injection or heating because the transport mechanism through C_{60} is phonon-assisted hopping as discussed in section 2.5. Simultaneous FMR-Raman spectroscopy measurements have been carried out in order to determine whether the Raman active molecular vibrations were being modified. Splitting of peaks, shifts in position or changes in relative intensity would suggest a modification of the molecular vibrations from spin pumping or phonon injection. Finally photoluminescence (PL) measurements have been carried out simultaneously with FMR to determine the effect of spin pumping and phonon injection on the exciton recombination in C_{60}.

7.2 Simultaneous ferromagnetic resonance-transport through C_{60}-based junctions

To perform FMR simultaneously with electron transport is a non-trivial technical problem. The difficulty lies in successfully making electrical contact with a device while also exciting the ferromagnetic electrode to resonance. One route would be to fabricate devices directly on a waveguide [146; 147], however this would involve in-depth lithographic fabrication procedures, so a simpler solution is desirable. A range of techniques were experimented with until the most successful method was found, taking into account the device geometry (cross-hair junction) used in this research. Wire bonding to the contact pads and making contact with silver conducting paint to Al wires were tried, but in both of these methods, either the wire would become detached and therefore lose contact, or the sample would be raised significantly away from the

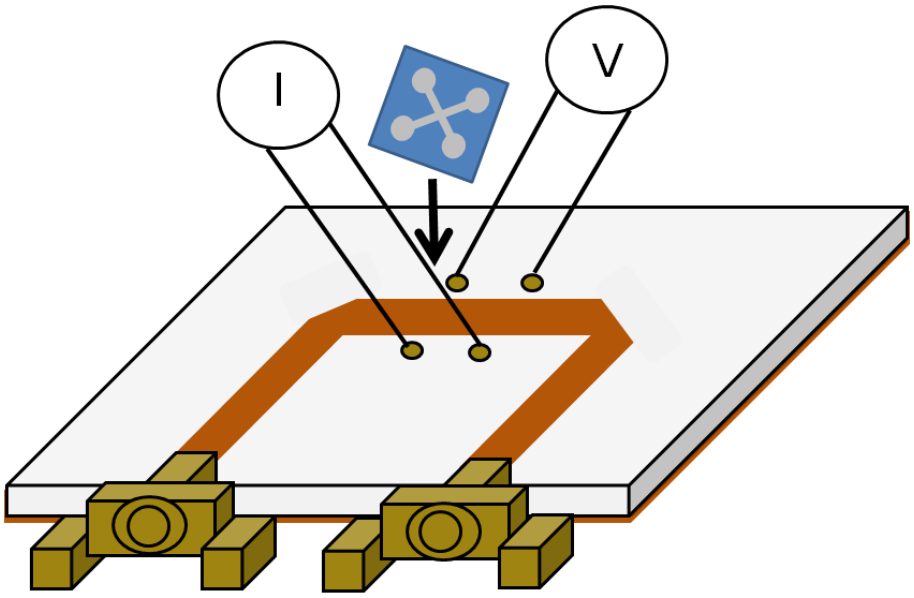

Figure 7.1: *Waveguide for simultaneous FMR transport. Here four pogo pins have been drilled around the copper stripline on the printed circuit board so that the contact pads of the C_{60} junction can be contacted while allowing the sample to be in contact with the waveguide itself.*

waveguide because of silver paint, resulting in less power transmission to the sample. The best method was found to be designing a waveguide so that pogo pins could be drilled just outside of the stripline to make electrical contact with the junction contact pads as shown in figure 7.1. The sample can then be clipped on, making good electrical contact while still being very close/in contact with the waveguide because of the retractable pogo pins. This system was also modified with high vacuum feedthroughs and connectors so that the transport measurements can be carried out under vacuum to prevent the deterioration of devices in atmospheric conditions.

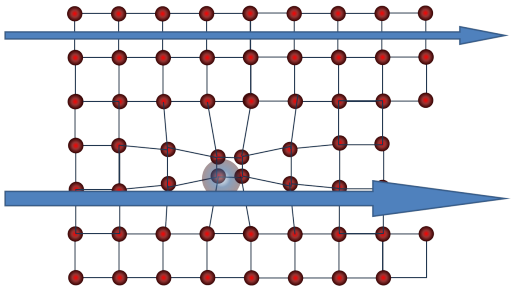

Figure 7.2: *Interpretation of phonon assisted tunnelling and how this can enhance the conductivity. The red circles represent molecules and the blue arrows represent conduction of electrons. The distortion in the lattice is a phonon. Figure was modified from reference [148].*

The resistance can be measured as a function of bias through a device and the results compared when the ferromagnetic electrode is on and off FMR. One may expect that any phonon injection into the C_{60} would result in an overall reduction in resistance because the transport mechanism in C_{60} is phonon-assisted hopping. To help picture this mechanism, figure 7.2 is a representation of phonons reducing the resistance. Here the red circles represent the C_{60} molecules and the blue arrows represent the electrons conducting. The phonon is visualised by the distortion of the lattice and this diagram shows the larger conduction of electrons occurring when there is a phonon present.

Figure 7.3 shows simultaneous FMR-transport measurements comparing a reference Al_2O_3 junction with the structure Py/Al_2O_3/Au and a C_{60} junction with the structure Py/Al_2O_3/C_{60}(10 nm)/Au. For the reference junctions with just the Al_2O_3 tunnel barrier, the resistance through the device only revealed a very small change of less

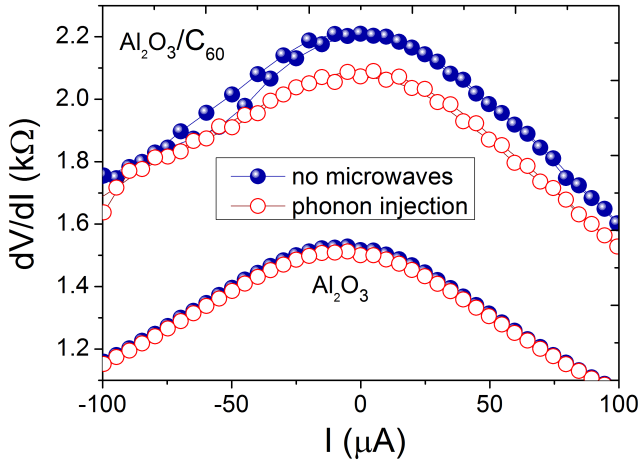

Figure 7.3: *Simultaneous FMR-transport measurements with and without microwave irradiation for an Al_2O_3 MTJ with the structure Py/Al_2O_3/Au and a C_{60} junction with the structure Py/Al_2O_3/C_{60}(10 nm)/Au.*

than 0.5% when comparing the on and off FMR state. This is a result of the tunnelling mechanism through this layer and the large energy barrier on the order of eV for Al_2O_3 which is a wide band-gap insulator. For the device with a C_{60} spacer layer, the change in resistance is more apparent, approximately 5% with a few μA bias. The electrons in the C_{60} see an effective barrier on the order of 10 meV. The dissipation of phonons into the C_{60} gives rise to inelastic scattering events between localised electrons and phonons, giving the electrons more energy to overcome the barrier and thus reduces the resistance of the C_{60} [78]. Therefore, the phonon dissipation does not significantly affect the resistance of the wide band-gap insulator but it does reduce the resistance of C_{60}.

The difference between an increase in temperature and phonon injection must be considered. The phonon injection can be localised and anisotropic. One would expect the resistance across a C_{60} film to be reduced as temperature is increased because of the hopping mechanism though C_{60} as discussed in section 2.5. An increase in temperature would cause an enhancement in electron-phonon scattering, giving the electrons more energy to overcome the energy barrier for a hopping step. There is no preferential

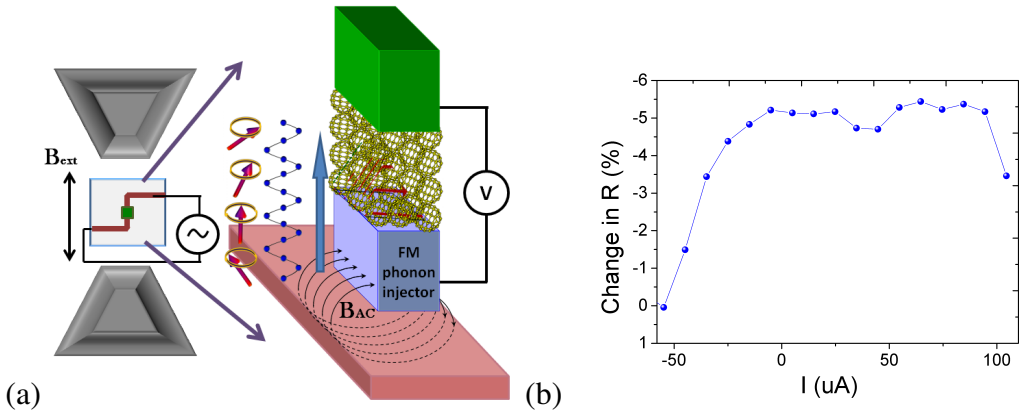

Figure 7.4: *(a) Simultaneous FMR-transport schematic showing the direction of phonon injection through the C_{60} in relation to the electron bias direction. (b) Change in resistance as a percentage between the on and off FMR state through the C_{60} junction as a function of current bias. The sample structure is Py/Al_2O_3/C_{60}/Au. The change in resistance is asymmetric as a function of bias so that the resistance change is the greatest when the electrons bias is in the same direction as the phonon injection direction.*

direction for the hopping steps with regards to positive/negative current bias in the case of an increase in temperature. For phonon injection one may expect the change in conductivity to be asymmetric dependent of the bias direction in relation to the direction of phonon injection as shown in figure 7.4a. The phonons are injected from the ferromagnetic electrode into the C_{60}. The electrons travelling in the same direction as the injected phonons experience a lower effective energy barrier compared to the electrons travelling in the opposite direction and thus the change in resistance between the on and off FMR state is maximised with positive bias as shown in figure 7.4b. This is a significant result because it agrees with the suggestion in the previous chapter, that the damping mechanism of a ferromagnetic material at FMR into adjacent C_{60} is not only spin pumping but also phonon injection. The asymmetric dependence allows one to differentiate between phonon injection and heating.

7.3 Spin pumping and phonon injection effect on C_{60} vibrational modes

In this section simultaneous Raman-FMR measurements will be presented and discussed. Changes in Raman active vibrational modes of C_{60} can be probed via Raman spectroscopy to determine changes in frequency and relative intensity of molecular vibrations. To perform these measurements simultaneously, the samples were deposited on glass. This allowed the laser to penetrate the C_{60} while the ferromagnetic material is face down on the waveguide, as shown in figure 7.5.

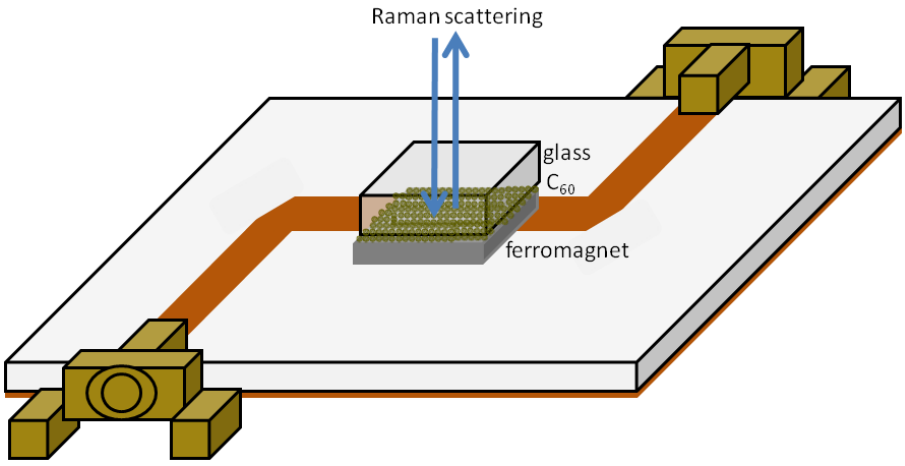

Figure 7.5: *Schematic diagram of a 50 ohm impedance matched waveguide. A C_{60} sample can be deposited on glass with the ferromagnetic material on top. This sample can be placed face down onto the waveguide so that the ferromagnetic material is close to the waveguide while the laser can probe through the glass to the C_{60}.*

Raman-FMR measurements were carried out on glass/C_{60}/Py samples, where figure 7.6a shows Raman spectra on and off the FMR state. The strongest Raman signal is due to the Ag(2) vibrational mode, which is a pinch mode of the C_{60}. For a neutral C_{60} molecule this Ag(2) mode should be at 1471 cm^{-1} as given in table 2.3. The Ag(2) mode is extremely sensitive to intermolecular interactions and it can be shifted in wavenumber or split/duplicated multiple times. When the C_{60} molecules are charged, triplet states are formed which result in an additional vibration of C_{60} at 1458 cm^{-1}

as well as a red shift in the Ag(2) mode to lower frequencies [49; 149; 150]. When the Py electrode adjacent to the C_{60} is at FMR, the normal Ag(2) mode is reduced and the energy or vibrations are transferred to the replica modes at 1444, 1452 and 1458 cm^{-1}. The replica mode at 1458 cm^{-1} is shifted to a lower frequency by 0.6 cm^{-1}, suggesting there is a charge transfer onto the C_{60} molecule [120; 121]. This charge transfer may be spin polarised and can lead to the formation of spin triplets and thus enhanced intramolecular interactions [49].

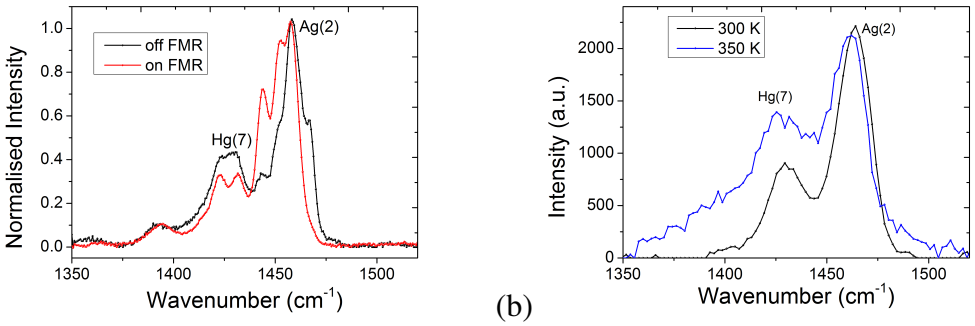

Figure 7.6: *(a) Simultaneous FMR-Raman measurements of a C_{60} film deposited on Py in the on and off FMR state. There are clear changes in relative intensity of the Ag(2) degenerate modes. This can be related to the presence of spin polarised electrons in the C_{60}. In addition to this the Hg(7) peak splits. There is a change in the relative intensity between the Ag(2) and Hg(7) modes. (b) Raman spectroscopy measurements with and without heat. This shows clear broadening of the Ag(2) and Hg(7) but no apparent splitting of the Ag(2) or Hg(7) peak.*

These changes in the Ag(2) mode are comparable to those observed when a spin current propagates into the C_{60}. The Raman spectrometer has been set up so that simultaneous Raman-transport measurements can be carried out. The metallic electrodes can be wire bonded to make electrical contact and different currents can be applied while performing Raman spectra. Shifts or changes in intensity of Raman peaks as a result of an applied current may then be detected. Figure 7.7a compares Raman spectroscopy measurements on C_{60} without an applied current, with an applied current from a gold electrode and an applied current from a cobalt electrode, as shown by Moorsom et al [49]. The presence and spin polarisation of electrons on the C_{60} molecules is shown in

figure 7.7b.

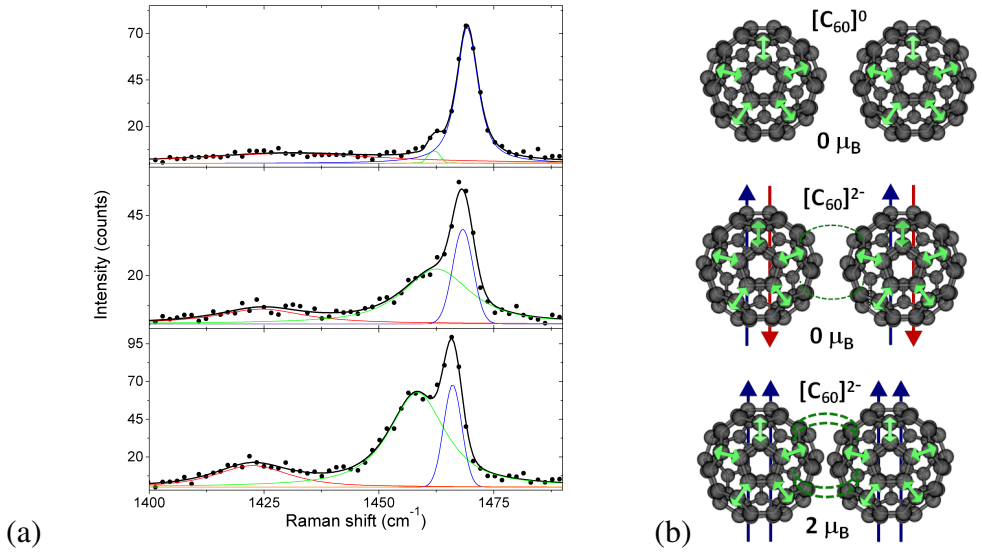

Figure 7.7: *(a) Raman spectroscopy measurement on C_{60} (top) without a current applied (middle) with a current applied across a gold electrode (not spin polarised) (bottom) with a current applied across a cobalt electrode (spin polarised). (b) C_{60} molecules (top) without additional electrons (middle) with electrons (bottom) with spin polarised electrons. Work by Mr Timothy Moorsom taken from reference [49].*

On the addition of a non-spin polarised current from the gold electrode, one observes a small shift in the Ag(2) peak of 1 cm^{-1}. When a spin polarised current from a cobalt electrode is applied the Ag(2) peak is further shifted, but 3-4 cm^{-1}. In addition to the changes in the Ag(2) peak one also observe an enhancement in the Hg(7) peak by a factor of 5 on application of the spin polarised current. This can be explained by more charged states in the C_{60} and the spin polarised electrons on the C_{60} leading to a preferred alignment of $[C_{60}]^{2-}$ triplets. This strengthens intermolecular electromagnetic interactions and thus leads to the splitting of the Ag(2) peak at 1460 cm^{-1} as shown by Moorsom et al [49].

As well as the changes in the Ag(2) pinch mode, changes have also been observed in the Hg(7) breathing mode. During FMR the intensity of the Hg(7) mode is reduced

as shown in figure 7.6. This mode is also split into two which suggests there is a Jahn-Teller distortion of the C_{60} as a result of spin polarised current. Raman spectroscopy measurements were also carried out during heating of the sample on a hot plate to ensure the changes in vibrational modes were not simply a result of heating a shown in figure 7.6b. The Ag(2) and Hg(7) peaks clearly broaden as the temperature is increased to 350 K from 300 K. These peaks do not split during heating, suggesting the splitting observed in the on FMR state is not a result of heating.

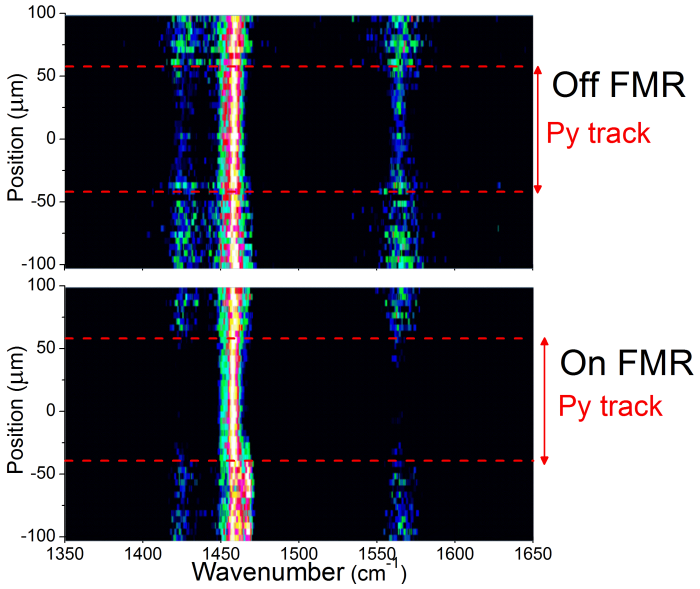

Figure 7.8: *Raman spectroscopy map on glass/C_{60}/Al_2O_3/Py. The map is in position on and off an Al_2O_3/Py track. Off the track, the C_{60} is only in contact with the glass substrate. The top figure is the control measurement, in the off FMR state whereas the bottom figure is in the on FMR state.*

The ferromagnetic material during FMR may inject phonons into the C_{60} molecules via intramolecular vibrations of the C_{60} lattice as discussed in section 2.5. To test this theory, simultaneous Raman-FMR measurements were carried out on C_{60}/Al_2O_3/Py, where the Al_2O_3 barrier should quench the spin wave propagation at the interface but not the phonon injection. Figure 7.8 shows simultaneous FMR-Raman measurements of C_{60} on and off a Al_2O_3/Py track which is between the red dashed line on map be-

tween 50 and - 50 μm. The C_{60} without the Al_2O_3/Py on top acts as the control sample. The top figure is in the off FMR state whereas the bottom figure is in the on FMR state. It is apparent from the comparison of these two maps that on top of the Al_2O_3/Py track, the Hg(7) and Hg(8) breathing modes are reduced during FMR or in other words during phonon injection. The Ag(2) pinch mode is reduced and the Ag(2) replicas at 1445-1464 cm^{-1} are enhanced during FMR on top of the Al_2O_3/Py track. This change suggests that enhanced intramolecular interactions due to phonon injection cause the Ag(2) pinch mode to be displaced.

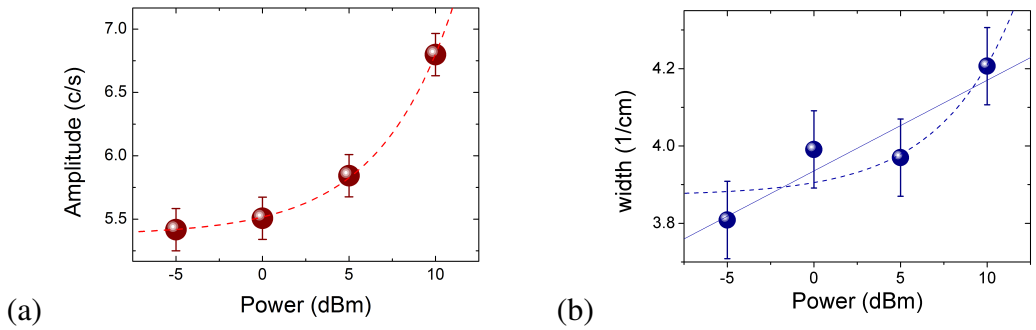

Figure 7.9: *Simultaneous FMR-Raman measurements of a C_{60} film deposited on Py. (a) Here the amplitude of the Ag(2) mode is extracted from Lorentzian fits and is shown to increase with increasing power of the RF signal. The dotted line is an exponential fit. (note that power is in dBm so this would be a linear fir to power in mW)(b) Similarly the width of the Ag(2) increases with increasing power suggesting an increase in phonon-injection. The straight line is a linear fit whereas the dotted line is an exponential fit.*

Figure 7.9 shows data extracted from Lorentzian fits to simultaneous FMR-Raman measurements of glass/C_{60}/Py. In figure 7.9a the amplitude of the Ag(2) peak has been determined as a function of power through the waveguide. The microwave power in dBm is a logarithmic scale so the exponential fit to the power in dBm means the amplitude is linearly proportional to the microwave power as shown in figure 7.9a. Figure 7.9b shows the width of the Ag(2) peak as a function of power through the waveguide. Similarly, the width increases with increasing microwave power which implies phonon-injection in the C_{60}. It is unclear whether a linear or exponential fit is the most

appropriate in this case. Therefore, the GHz resonances cause changes in the THz regime of molecular optical vibrons. This again suggests that there is an interaction between the ferromagnetic material at FMR and the vibrational modes of the adjacent C_{60}. The population of the vibrational modes can be manipulated by FMR. As future work, measurements in the anti-Stokes region would allow one to investigate the vibrational modes that are already excited rather than the vibrational modes that are excited by the laser.

7.4 Photoluminescence

C_{60} is a photoluminescent molecule and as such the optical emission can be measured to determine properties of a C_{60} film. The PL of C_{60} is dependent on temperature, defects and the charge state as well as phonon injection. The photoemission of polar semiconductors is enhanced as a result of phonon-exciton coupling via Fröhlich coupling and deformation potential scattering. When the momentum transfer is relatively small the deformation potential scattering is the dominant mechanism [151]. Phonon coupling causing an enhancement in photoemission has been observed in other carbon based materials such as graphene and carbon nanotubes [152].

The PL is quenched as a result of charge transfer at metallic-C_{60} interfaces as shown in figure 7.10[49]. To observe significant photoemission, an insulating layer, in this case Al_2O_3, can be deposited between the metal and C_{60}, otherwise electron transfer quenches the photoemission. This Al_2O_3 layer acts to prevent propagation of spin waves while allowing the injection of phonons into the C_{60} film.

Moorsom et al deposit C_{60} on top of a Co and Au electrode, all on a SiO_2 substrate as represented in the schematic shown in figure 7.10[49]. The PL intensity is plotted as a function of position on the sample where the SiO_2 substrate, Co and Au are labelled. It is evident that the PL is reduced on the Co and Au in comparison to the C_{60} directly on the SiO_2 substrate. This is a result of charge transfer into the C_{60} modifying the PL, which is larger for the Co than for the Au. When an external magnetic field is applied perpendicular to the sample an enhancement in the PL is then observed. Changes in

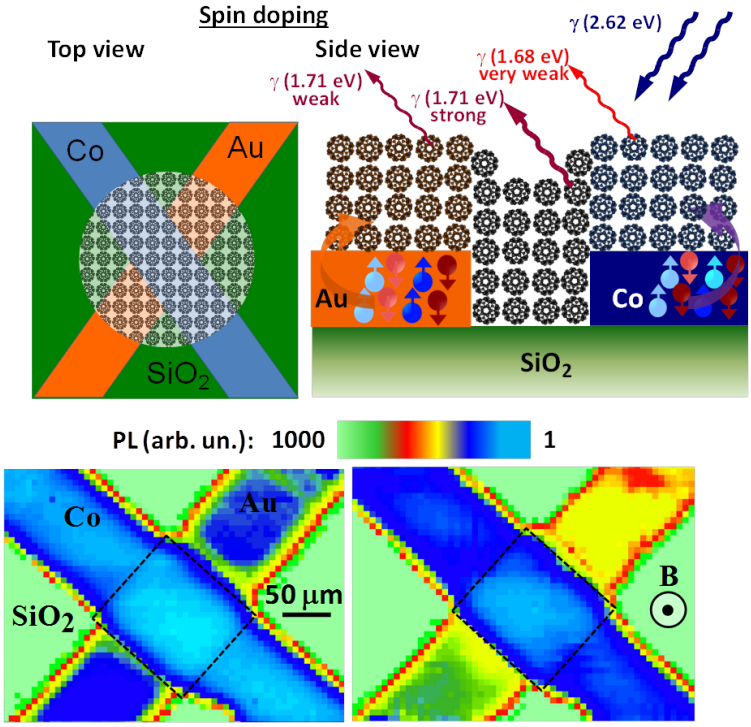

Figure 7.10: *Top left: sample schematic of a SiO_2 substrate with 100 µm wide Au and Co electrodes deposited on top, with C_{60} covering part of the sample. Top right: schematic showing the effect charge and spin transfer has on exciton recombination and PL. Bottom: PL maps in position across the sample showing reduced PL on the metals compared to on SiO_2 without a magnetic field (left) and with a magnetic field (right). Work by Mr Timothy Moorsom taken from reference [49].*

PL of C_{60} in the presence of a magnetic field have been observed before [149; 153], but what is significant here is the PL of C_{60} on Au is enhanced by 40% whereas it is enhanced by only 10% for C_{60} on Co on the application of a magnetic field. The areas of the Co which are not saturated have a smaller change in PL, suggesting that spin doping or local stray fields are the contributing to the change in PL [49].

In order to observe the effect on PL and exciton recombination from a ferromagnetic material at resonance into the adjacent C_{60}, we performed simultaneous PL-FMR measurements on and off an Al_2O_3/Py track. The sample is the same as that described in figure 7.8. PL maps can be carried out as a function of position on and off the

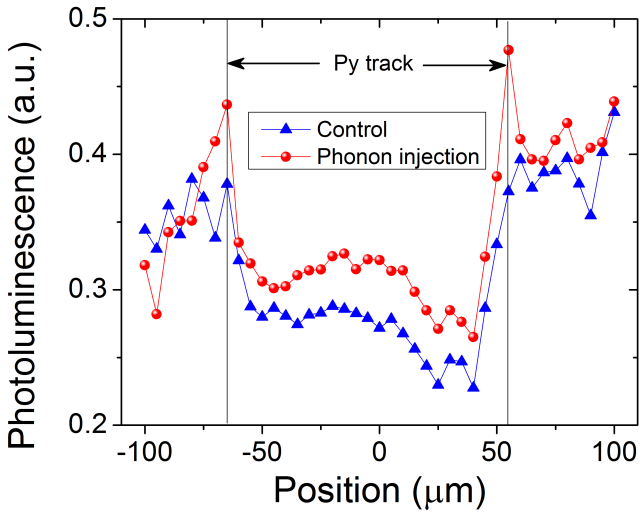

Figure 7.11: *Simultaneous FMR-PL map on glass/C_{60}/Al_2O_3/Py showing the maximum intensity as a function of position of C_{60} on and off a 100 μm /Al_2O_3/Py track all on the waveguide. The control (no FMR) and phonon injection (during FMR) measurements are compared.*

Al_2O_3/Py track. A fixed magnetic field was applied and the frequency was swept through the waveguide which has the sample positioned on top as shown in figure 7.5. An increase in the intensity of the photoemission of C_{60} by $12 \pm 3\%$ is observed when the adjacent Py is at FMR which can be attributed to phonon injection as shown in figure 7.11. The enhanced photoemission may also result from an increase in spin population or magnetisation of the C_{60}. However, the change in intensity of the photoemission of the C_{60} off the Py track is $(3 \pm 6\%)$, i.e. not significant. This result suggests the changes in PL of the C_{60} really can be attributed to the power dissipation of the Py during FMR rather than merely being an effect of the microwaves through the waveguide. The PL is slightly reduced on the Py track compared to off the track because of charge transfer into the C_{60} even though there is an Al_2O_3 layer between the Py and C_{60}. This charge transfer could be from a thin layer of unoxidised Al at the C_{60} interface.

Figure 7.12a shows normalised FMR-PL data with and without the microwave frequency through the waveguide. The control measurement was subtracted from the

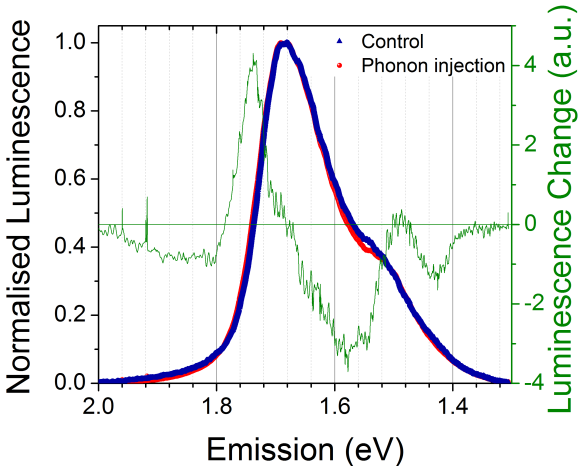

Figure 7.12: *Simultaneous FMR-PL measurement of $C_{60}/Al_2O_3/Py$. The data has been normalised to compare the control measurement and the phonon injection spectra. The control measurement has been subtracted from the phonon injection measurement (plotted in green.)*

spectra during phonon injection to reveal a complicated response during FMR. Although the overall intensity of the PL has been shown to be enhanced, the phonon replicas respond differently to the FMR. The data is normalised to the zero phonon emission peak at 1.69 eV, so in comparison to this peak the phonon replicas at 1.58 and 1.43 eV are reduced. This peak at 1.77 eV can be related to lattice distortions in the C_{60} [154] and appears to be enhanced during phonon injection.

Figure 7.13 shows the response of the PL in the C_{60} to the application of an RF pulse and the relaxation over a 2 hour time period. On the application of the RF through the waveguide the PL intensity is enhanced and continues to be enhanced during the application of the RF with time. When the RF is then removed the intensity of the PL decreases over a two hour period and eventually returns to the intensity of the original measurement without RF. One possible explanation for this slow relaxation process is an accumulation of spin polarised electrons with no ability to discharge such a build up. The timescale for the relaxation of the PL in this measurement is long. For the FMR-transport measurements, the resistance of the devices returned to that of the off RF state within the time it took to do another measurement, which was a number of minutes. The timescale for the Raman spectra to return to the off resonance state was

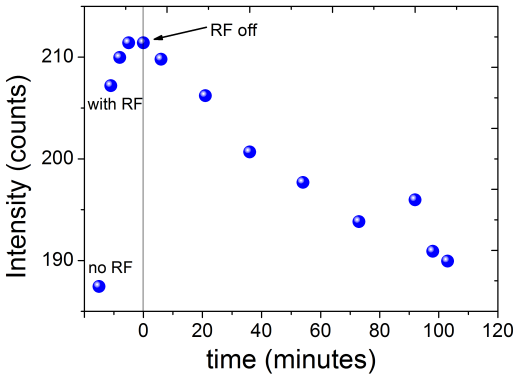

Figure 7.13: *The maximum intensity of the PL measurements of C_{60} on glass with the Py with and without RF and with time. The applied RF increases the intensity and the intensity increases further with time. When the RF is then turned off it takes 2 hours for the intensity to return to the same intensity as without RF.*

also shorter than the time it took to carry out another measurement, which was also on the order of minutes. This suggests the mechanism behind the enhancement in PL is somewhat different to that of the changes in vibrational modes and the conductivity of C_{60}. Further investigation is required to fully understand these differences, including further PL with time measurements.

7.5 Conclusion

It was shown that the resistance through C_{60} can be reduced by up to 5% as a result of phonon injection from Py at FMR. This resistance change is asymmetric as a function of bias, where the resistance is most reduced when the electron bias is in the same direction as the phonon injection as a result of the phonon-assisted transport mechanism. Simultaneous Raman-FMR measurements were carried out where splitting and shifts in energy of vibrational modes may reveal the presence of spin polarised electrons on the C_{60} molecules. Raman-FMR measurements on C_{60} with a barrier separating the C_{60} from the Py show changes in relative intensity of the vibrational modes as well, suggesting there is phonon injection into the C_{60}. Finally, changes in the PL of C_{60} were observed during FMR, including enhancements in intensity and changes in rel-

ative intensity of phonon replicas of C_{60}. It has been shown that not only can the conductivity of C_{60} be modified by phonon injection from a ferromagnetic material during FMR but the molecular vibrations and photoluminescent properties can also be manipulated. These results may pave the way for novel devices where molecular properties are controlled via phonon injection.

CHAPTER 8

Conclusions and future work

For a new technology to be worth implementing it must either surpass an existing technology by orders of magnitude or it must have new functionalities. Instead of working towards improving devices such as organic spin valves where the magnetoresistance may be equivalent to or eventually higher than conventional inorganic magnetic tunnel junctions, one must consider utilising molecular properties. In order to really outperform conventional devices, the promise of phonon-assisted electronics must be considered as a possibility for second generation spintronic devices. This is just the beginning of an exciting new field where FMR and molecular electronics can be combined in a range of new and interesting devices. The great possibilities include THz spintronics because the manipulation of THz vibrational modes has been realised by exciting devices using just GHz frequencies. As well as technological applications, there is a significant amount of fundamental physics yet to be fully understood, in particular with regards to mechanisms behind spin transport in organics and spin pumping into organics. I have addressed these problems by combining electron transport, FMR and spectroscopy techniques when studying C_{60} molecules.

The field of organic spintronics has sparked a lot of interest in recent years owing to the low atomic mass of organics, leading to weak spin orbit coupling and therefore long spin lifetimes [1]. A range of molecular materials have been used successfully as the spacer layer in organic spin valves, for instance Alq_3 and rubrene [29–31]. C_{60} has been of particular interest due to the weak hyperfine interaction in pure carbon, leading to a long spin diffusion length. Graphene and carbon nanotubes have also been used in spin injection devices [155; 156], however C_{60} was chosen in this research because it is relatively easy to deposit and is robust to the deposition of metals [18]. C_{60} based spin valve devices have been successfully deposited and measured in this research [34] as well as by other groups [18; 32; 33]. A custom built thermal sublimation source was added to the sputter deposition system to allow in-situ deposition of molecular/metallic devices. Through TEM and XRR it was determined that C_{60} could withstand the deposition of metals via sputter deposition with no observable interdiffusion of layers. This led to further studies as to whether more sensitive devices could be made in the same way. Copper based spin valves were deposited on to C_{60} underlayers where an enhanced exchange bias was observed. These results suggest hybridisation of the C_{60} with the adjacent ferromagnet and that C_{60} would be suitable as the active spacer layer

in hybrid C_{60} spin valves.

Standard Al_2O_3 magnetic tunnel junctions were deposited and optimised before adding the C_{60} spacer layer. The insulating barrier is required to allow spin injection into the C_{60} by overcoming the conductivity mismatch problem between metals and resistive organic semiconductors. Magnetoresistance of 25 % was observed through C_{60} spin valves with 60 nm of C_{60} at 10 K [34]. Magnetoresistance was also measured at room temperature through 20 nm of C_{60} with 8 % magnetoresistance. Asymmetries were observed in the resistance dependence on the direction of magnetic field in the positive and negative parallel alignments of the ferromagnetic electrodes at low temperatures in some of the thick C_{60} (60 nm) spin valves. This may suggest there is hybridisation between the C_{60} and the ferromagnetic materials forming a hard magnetic layer via antiferromagnetic coupling [49]. Additionally, the role of the Al_2O_3 layer was investigated via point contact Andreev reflection, where leaky Al_2O_3 barriers and discontinuous layers of C_{60} were deposited. Here the spin polarisation of the ferromagnetic material adjacent to the C_{60} was measured directly and was shown to decrease with increasing C_{60} thickness. Despite being able to successfully deposit and measure a number of hybrid C_{60} spin valves, it was apparent that the devices break down as a result of current causing pinholes and sudden drops in resistance.

To overcome the break down of devices and the conductivity mismatch problem for spin injection between low resistance metals and high resistance semiconductors [35], other spin injection methods can be used. Instead of using an insulating barrier in a spin valve device, one can inject spins by an adjacent ferromagnetic material at FMR [39]. Spin pumping has been used to inject spins into inorganic semiconductors [39], a conducting polymer [40] and an organic semiconductor [41]. The spin injection can be detected by a voltage induced via the inverse spin Hall effect in heavy metallic contacts. This led us to investigate the energy dissipated from a ferromagnetic material at resonance into an adjacent C_{60} film, and whether this could be used to manipulate molecular properties or for high frequency devices. FMR measurements were performed on C_{60}/ferromagnetic bilayer samples to extract both the effective magnetisation and the damping parameter. It was found that the effective magnetisation of the ferromagnetic material in contact with the C_{60} is reduced by a few percent as a

result of a transfer of spin polarised electrons from the ferromagnet into the C_{60}, or spin doping. The damping parameter was extracted from the change in linewidth as a function of frequency and it was found that the damping is enhanced by up to 50 $\%$ on the addition of an adjacent C_{60} layer. This suggests that energy is being dissipated into the C_{60} in the form of spin pumping and/or phonon injection. The lack of change in damping in YIG/C_{60} samples could be attributed to the lack of conduction electrons in both materials which would prevent spin pumping.

Despite growing interest in organic spintronics, spectroscopic techniques have been relatively underused compared to magnetotransport measurements. Boehme suggested that spectroscopy in organic spintronics should be embraced to understand the nature of spin transport in organic materials [157]. In order to determine the nature of the damping mechanism of a ferromagnetic material at FMR adjacent to C_{60}, a range of techniques were utilised. Firstly, transport measurements were carried out and it was observed that the resistance through a C_{60} film is reduced during FMR suggesting an increase in phonons aiding hopping events. Secondly, the vibrational properties of C_{60} were also observed during FMR via Raman spectroscopy to determine shifts in energy/frequency as well as broadening and splitting of these vibrational modes. These results were then related back to spin injection, temperature changes and phonon injection. Finally, photoluminescence was performed simultaneously with FMR to determine whether the photoemission of C_{60} can be modified by phonon injection. Shifts in relative intensities of phonon replicas and changes in the intensity of the photoemission were observed suggesting that there is a phonon contribution to the damping mechanism of the ferromagnet.

There is a range of interesting physics left to discover and many experiments to be carried out in the future. Low temperature FMR-transport measurements would allow a much deeper understanding of the damping mechanism of the ferromagnetic material into the C_{60}. One might expect to observe large changes in this damping parameter, particularly around 90 K where the rotational vibrational modes of the C_{60} are frozen. Further FMR-transport measurements could be carried out investigating different thicknesses of C_{60} and at a range of temperatures. We could probe the anti-Stokes region in Raman spectroscopy for vibrational modes that are already excited,

rather than exciting the vibrations with photons. Measuring this region simultaneously with FMR could provide more information about the effect spin pumping and phonon injection has on C_{60}. The low frequency region of Raman scattering, between 0 and 60 cm^{-1} can be related to intermolecular interactions so this region could be studied in depth by using an ultra-low frequency filter on the Raman spectrometer simultaneously with FMR measurements [76]. X-ray magnetic dichroism could be used to probe the spin and orbital magnetic moments of specific layers or elements during FMR [158]. Furthermore, C_{60} has been a test molecule for such experiments; investigating other molecules and observing differences in the molecular vibrations and damping mechanism of an adjacent ferromagnet could clarify our understanding. For example endohedrally doped C_{60} could be studied, where the enclosed element could be varied to investigate the effect of spin orbit coupling [159]. C_{60} could also be endohedrally doped with hydrogen to enhance hyperfine interaction [160]. Detection of spin injection in organics via the inverse spin Hall effect has proven a useful technique to study spin to charge conversion as well as spin injection [40; 41]. Using this technique to investigate other organic materials could lead to a better understanding of these systems. These exciting experiments may pave the way for the future of molecular spintronics and phonon-assisted electronics where the molecular properties can actually be utilised in second generation spintronic devices.

REFERENCES

[1] Y. Sheng, T. D. Nguyen, G. Veeraraghavan, O. Mermer, and M. Wohlgenannt, "Effect of Spin-orbit Coupling on Magnetoresistance in Organic Semiconductors," *Physical Review B*, vol. 75, no. 3, p. 035202, 2007.

[2] P. A. Bobbert, W. Wagemans, F. W. A. van Oost, B. Koopmans, and M. Wohlgenannt, "Theory for Spin Diffusion in Disordered Organic Semiconductors," *Physical Review Letters*, vol. 102, no. 15, p. 156604, 2009.

[3] X. Zhang, S. Mizukami, T. Kubota, Q. Ma, M. Oogane, H. Naganuma, Y. Ando, and T. Miyazaki, "Observation of a Large Spin-dependent Transport Length in Organic Spin Valves at Room Temperature," *Nature Communications*, vol. 4, p. 1392, 2013.

[4] Z. Bao, A. Dodabalapur, and A. J. Lovinger, "Soluble and Processable Regioregular Poly(3-hexylthiophene) for Thin Film Field-effect Transistor Applications with High Mobility," *Applied Physics Letters*, vol. 69, no. 26, p. 410810, 1996.

[5] G. Horowitz, "Organic Field-effect Transistors," *Advanced Materials*, vol. 10, no. 5, p. 36577, 1998.

[6] L. L. Chua, J. Zaumseil, J. F. Chang, E. C. W. Ou, P. K. H. Ho, H. Sirringhaus, and R. H. Friend, "General Observation of N-type Field-effect Behaviour in Organic Semiconductors," *Nature*, vol. 434, no. 7030, p. 19499, 2005.

[7] H. Sirringhaus, "Device Physics of Solution-processed Organic Field-effect Transistors," *Advanced Materials*, vol. 17, no. 20, p. 241125, 2005.

[8] J. Zaumseil and H. Sirringhaus, "Electron and Ambipolar Transport in Organic Field-effect Transistors," *Chemical Reviews*, vol. 107, no. 4, p. 12961323, 2007.

[9] H. Sirringhaus, "Reliability of Organic Field-Effect Transistors," *Advanced Materials*, vol. 21, pp. 3859–3873, 2009.

[10] G. Li, V. Shrotriya, J. S. Huang, Y. Yao, T. Moriarty, K. Emery, and Y. Yang, "High-efficiency Solution Processable Polymer Photovoltaic Cells by Self-organization of Polymer Blends," *Nature Materials*, vol. 4, no. 11, p. 86468, 2005.

[11] S. Guenes, H. Neugebauer, and N. S. Sariciftci, "Conjugated Polymer-based Organic Solar Cells," *Chemical Reviews*, vol. 107, no. 4, p. 132438, 2007.

[12] B. C. Thompson and J. M. J. Frechet, "Organic Photovoltaics - Polymer-fullerene Composite Solar Cells," *Angewandte Chemie-International Edition*, vol. 47, no. 1, p. 5877, 2008.

[13] H. Bronstein, Z. Chen, R. S. Ashraf, W. Zhang, J. Du, J. R. Durrant, P. S. Tuladhar, K. Song, S. E. Watkins, Y. Geerts, M. M. Wienk, R. A. J. Janssen, T. Anthopoulos, H. Sirringhaus, M. Heeney, and I. McCulloch, "Thieno[3,2-b]thiophene-Diketopyrrolopyrrole-Containing Polymers for High-Performance Organic Field-Effect Transistors and Organic Photovoltaic Devices," *Journal of the American Chemical Society*, vol. 133, no. 10, p. 327275, 2011.

[14] C. Tang, S. Vanslyke, and C. Chen, "Electroluminescence of Doped Organic Thin-Films," *Journal of Applied Physics*, vol. 65, no. 9, p. 361016, 1989.

[15] N. C. Greenham, R. H. Friend, and D. D. C. Bradley, "Angular-Dependence of the Emission from a Conjugated Polymer Light-Emitting Diode - Implications for Efficiency Calculations," *Advanced Materials*, vol. 6, no. 6, p. 49194, 1994.

[16] J. Kido, K. Hongawa, K. Okuyama, and K. Nagai, "White Light-Emitting Organic Electroluminescent Devices Using the Poly(n-Vinylcarbazole) Emitter Layer Doped with 3 Fluorescent Dyes," *Applied Physics Letters*, vol. 64, no. 7, p. 81517, 1994.

[17] H. W. Kroto, J. R. Heath, S. Obrien, R. F. Curl, and R. Smalley, "C60 - Buckminsterfullerene," *Nature*, vol. 318, pp. 162–163, 1985.

[18] M. Gobbi, F. Golmar, R. Llopis, F. Casanova, and L. E. Hueso, "Room-Temperature Spin Transport in C60-Based Spin Valves," *Advanced Materials*, vol. 23, p. 1609, 2011.

[19] M. Gobbi, A. Pascual, F. Golmar, R. Llopis, P. Vavassori, F. Casanova, and L. E. Hueso, "C60/NiFe Combination as a Promising Platform for Molecular Spintronics," *Organic Electronics*, vol. 13, pp. 366–372, 2012.

[20] X.-H. Zhang, B. Domercq, and B. Kippelen, "High-performance and Electrically Stable C60 Organic Field-effect Transistors," *Applied Physics Letters*, vol. 91, no. 9, p. 092114, 2007.

[21] X.-H. Zhang and B. Kippelen, "Low-voltage C60 Organic Field-effect Transistors with High Mobility and Low Contact Resistance," *Applied Physics Letters*, vol. 93, no. 13, p. 133305, 2008.

[22] H. Li, B. C.-K. Tee, J. J. Cha, Y. Cui, J. W. Chung, S. Y. Lee, and Z. Bao, "High-Mobility Field-Effect Transistors from Large-Area Solution-Grown Aligned C60 Single Crystals," *Journal of the American Chemical Society*, vol. 134, no. 5, p. 276065, 2012.

[23] P. Sullivan and T. S. Jones., "Pentacene/fullerene (C60) Heterojunction Solar Cells: Device Performance and Degradation Mechanisms," *Organic Electronics*, vol. 9, no. 5, p. 65660, 2008.

[24] G. Zhao, Y. He, and Y. Li, "6.5 Percent Efficiency of Polymer Solar Cells Based on Poly(3-hexylthiophene) and Indene-C60 Bisadduct by Device Optimization," *Advanced Materials*, vol. 22, no. 39, p. 435558, 2010.

[25] S.-H. Chanu, C.-S. Lai, H.-L. Chen, C. Ting, and C.-P. Chen, "Highly Efficient P3HT: C60 Solar Cell Free of Annealing Process," *Macromolecules*, vol. 44, no. 22, p. 888691, 2011.

[26] N. S. Sariciftci, D. Braun, C. Zhang, V. I. Srdanov, A. J. Heeger, G. Stucky, and F. Wudl, "Semiconducting Polymer-buckminsterfullerene Heterojunctions: Diodes, Photodiodes, and Photovoltaic Cells," *Applied Physics Letters*, vol. 62, no. 6, p. 58587, 1993.

[27] J. Y. Lee and J. H. Kwon, "The Effect of C60 Doping on the Device Performance of Organic Light-emitting Diodes," *Applied Physics Letters*, vol. 86, no. 6, p. 063514, 2005.

[28] J. Y. Lee, "Efficient Hole Injection in Organic Light-emitting Diodes Using C60 as a Buffer Layer for Al Reflective Anodes," *Applied Physics Letters*, vol. 88, no. 7, p. 073512, 2006.

[29] Z. H. Xiong, D. Wu, Z. V. Vardeny, and J. Shi, "Giant Magnetoresistance in organic Spin-Valves," *Nature*, vol. 427, pp. 821–824, 2004.

[30] D. Sun, L. Yin, C. Sun, H. Guo, Z. Gai, X. Zhang, T. Z. Ward, Z. Cheng, and J. Shen, "Giant Magnetoresistance in Organic Spin Valves," *Physical Review Letters*, vol. 104, 2010.

[31] X. Zhang, S. Mizukami, T. Kubota, M. Oogane, H. Naganuma, Y. Ando, and T. Miyazaki, "Spin Transport in Co/Al2O3/Alq3/Co Organic Spin Valve," *IEEE Transactions on Magnetics*, vol. 47, no. 10, p. 264951, 2011.

[32] R. Lin, F. Wang, M. Wohlgenannt, C. He, X. Zhai, and Y. Suzuki, "Organic Spin-Valves Based on Fullerene C60," *Synthetic Metals*, vol. 161, pp. 553 – 557, 2011.

[33] T. L. A. Tran, T. Q. Le, J. G. M. Sanderink, W. G. van der Wiel, and M. P. de Jong, "The Multistep Tunneling Analogue of Conductivity Mismatch in Organic Spin Valves," *Advanced Functional Materials*, vol. 22, p. 11801189, 2012.

[34] F. A. Ma'Mari, M. Wheeler, K. E. Kendrick, T. Moorsom, G. Burnell, B. J. Hickey, and O. Cespedes, "Direct Measurement of Spin Polarization in Ferromagnetic C60 Interfaces using Point-Contact Andreev Reflection," *IEEE Transactions on Magnetics*, vol. 50, no. 11, p. 14, 2014.

[35] G. Schmidt, D. Ferrand, L. W. Molenkamp, A. T. Filip, and B. J. van Wees, "Fundamental Obstacle for Electrical Spin Injection from a Ferromagnetic Metal into a Diffusive Semiconductor.," *Physical Review B*, vol. 62, p. R4790R4793, 2000.

[36] E. I. Rashba, "Theory of Electrical Spin Injection: Tunnel Contacts as a Solution of the Conductivity Mismatch Problem," *Physical Review B*, vol. 62, no. 24, p. R16267R16270, 2000.

[37] H. J. Zhu, M. Ramsteiner, H. Kostial, M. Wassermeier, H.-P. Schnherr, and K. H. Ploog, "Room-Temperature Spin Injection from Fe into GaAs," *Physical Review Letters*, vol. 87, no. 1, p. 016601, 2001.

[38] I. Appelbaum, B. Huang, and D. J. Monsma, "Electronic Measurement and Control of Spin Transport in Silicon," *Nature*, vol. 447, no. 7142, p. 29598, 2007.

[39] K. Ando, S. Takahashi, J. Ieda, H. Kurebayashi, T. Trypiniotis, C. H. W. Barnes, S. Maekawa, and E. Saitoh, "Electrically Tunable Spin Injector Free from the Impedance Mismatch Problem," *Nature Materials*, vol. 10, no. 9, p. 65559, 2011.

[40] K. Ando, S. Watanabe, S. Mooser, E. Saitoh, and H. Sirringhaus, "Solution-processed Organic Spin-charge Converter," *Nature Materials*, vol. 12, no. 7, p. 62227, 2013.

[41] S. Watanabe, K. Ando, K. Kang, S. Mooser, Y. Vaynzof, H. Kurebayashi, E. Saitoh, and H. Sirringhaus, "Polaron Spin Current Transport in Organic Semiconductors," *Nature Physics*, vol. 10, no. 4, p. 30813, 2014.

[42] K. Ando, S. Takahashi, J. Ieda, Y. Kajiwara, H. Nakayama, T. Yoshino, K. Harii, Y. Fujikawa, M. Matsuo, S. Maekawa, and E. Saitoh, "Inverse Spin-Hall Effect Induced by Spin Pumping in Metallic System," *Journal of Applied Physics*, vol. 109, no. 10, p. 103913, 2011.

[43] Z. G. Yu, "Suppression of the Hanle Effect in Organic Spintronic Devices," *Physical Review Letters*, vol. 111, no. 1, p. 016601, 2013.

[44] A. J. Drew, J. Hoppler, L. Schulz, F. L. Pratt, P. Desai, P. Shakya, T. Kreouzis, W. P. Gillin, A. Suter, N. A. Morley, V. K. Malik, A. Dubroka, K. W. Kim, H. Bouyanfif, F. Bourqui, C. Bernhard, R. Scheuermann, G. J. Nieuwenhuys, T. Prokscha, and E. Morenzoni, "Direct Measurement of the Electronic Spin Diffusion Length in a Fully Functional Organic SpinValve by Low-energy Muon Spin Rotation," *Nature Materials*, vol. 8, no. 2, p. 10914, 2009.

[45] Editorial, "A Better Spin on Organic Semiconductors," *Nature Nanotechnology*, vol. 8, no. 9, p. 611, 2013.

[46] T. Moorsom, M. Wheeler, T. M. Khan, F. A. Ma'Mari, C. Kinane, S. Langridge, D. Ciudad, A. Bedoya-Pinto, L. Hueso, G. Teobaldi, V. K. Lazarov, D. Gilks, G. Burnell, B. J. Hickey, and O. Cespedes, "Spin-Polarised Electron Transfer in Ferromagnet/C60 Interfaces," *Physical Review B*, vol. 90, no. 12, p. 125311, 2014.

[47] M. Wheeler, B. J. Hickey, and O. Cespedes, "Enhanced Exchange Bias of Spin Valves Fabricated on Fullerene-based Seed layers," *IEEE Transactions on Magnetics*, vol. 48, no. 11, 2012.

[48] S. Geller and M. A. Gilleo, "Structure and Ferrimagnetism of Yttrium and Rare-earthiron Garnets," *Acta Crystallographica*, vol. 10, no. 3, p. 239239, 1957.

[49] T. Moorsom, M. Wheeler, M. T. Khan, F. Ma'Mari, G. Burnell, B. J. Hickey, V. Lazarov, D. Gilks, and O. Cespedes, "Effects of Spin Doping and Spin Injection in the Luminescence and Vibrational Spectrum of C60," *Applied Physics Letters*, vol. 105, no. 2, p. 022408, 2014.

[50] J. S. Moodera, L. R. Kinder, T. M. Wong, and R. Meservey, "Large Magnetoresistance at Room-Temperature in Ferromagnetic Thin-Film Tunnel-Junctions," *Physical Review Letters*, vol. 74, pp. 3273–3276, 1995.

[51] M. Julliere, "Tunneling Between Ferromagnetic-films," *Physics Letters A*, vol. 54, pp. 225–226, 1975.

[52] J. S. Moodera and P. LeClair, "Nature Materials," *Spin Electronics: A Quantum Leap*, vol. 2, no. 11, p. 7078, 2003.

[53] T. Miyazaki and N. Tezuka, "Giant Magnetic Tunneling Effect in Fe/Al2O3/Fe Junction," *Journal of Magnetism and Magnetic Materials*, vol. 139, pp. L231–L234, 1995.

[54] S. M. Jaya and M. Valsakumar, "Greens Function Modeling of the Magnetoresistance of Magnetic Tunnel Junctions Exhibiting Quasiparticle Bands," *The European Physical Journal B*, vol. 72, pp. 41–51, 2009.

[55] J. G. Simmons, "Low-voltage Current-voltage Relationship of Tunnel Junctions," *Journal of Applied Physics*, vol. 34, p. 238, 1963.

[56] J. J. Akerman, R. Escudero, C. Leighton, S. Kim, D. A. Rabson, R. W. Dave, J. M. Slaughter, and I. K. Schuller, "Criteria for Ferromagnetic-Insulator-Ferromagnetic Tunneling," *Journal of Magnetism and Magnetic Materials*, vol. 240, pp. 86–91, 2002.

[57] H. N. Fuke, K. Saito, Y. Kamiguchi, H. Iwasaki, and M. Sahashi, "Spin-valve Giant Magnetoresistive films with Antiferromagnetic Ir-Mn Layers," *Journal of Applied Physics*, vol. 81, pp. 4004–4006, 1997.

[58] J. Nogues and I. K. Schuller, "Exchange Bias," *Journal of Magnetism and Magnetic Materials*, vol. 192, pp. 203–232, 1999.

[59] A. F. Andreev, "The Thermal Conductivity of the Intermediate State in Superconductors," *Soviet Physics Journal of Experimental Theoretical Physics*, vol. 19, no. 5, pp. 1228–1231, 1964.

[60] G. Blonder, M. Tinkham, and T. Klapwijk, "Transition from Metallic to Tunneling Regimes in Superconducting Microconstrictions: Excess Current, Charge Imbalance, and Supercurrent Conversion," *Physical Review B-Condensed Matter*, vol. 25, p. 4515, 1982.

[61] R. J. Soulen, J. M. Byers, M. S. Osofsky, B. Nadgorny, T. Ambrose, S. F. Cheng, P. R. Broussard, C. T. Tanaka, J. Nowak, J. S. Moodera, A. Barry, and J. M. D. Coey, "Measuring the Spin Polarization of a Metal with a Superconducting Point Contact," *Science*, vol. 282, pp. 85–88, 1998.

[62] S. K. Upadhyay, A. Palanisami, R. N. Louie, and R. A. Buhrman, "Probing Ferromagnets with Andreev Reflection," *Physical Review Letters*, vol. 81, no. 15, p. 324750, 1998.

[63] A. D. Naylor, *Measuring Spin Polarisation with Point Contact Andreev Reflection*. PhD thesis, University of Leeds, School of Physics and Astronomy, 2010.

[64] M. J. M. D. Jong and C. W. J. Beenakker, "Andreev Reflection in Ferromagnet-Superconductor Junctions," *Physical Review Letters*, vol. 74, no. 9, p. 165760, 1995.

[65] I. I. Mazin, A. A. Golubov, and B. Nadgorny, "Probing Spin Polarization with Andreev Reflection: A Theoretical Basis," *Journal of Applied Physics*, vol. 89, no. 11, p. 757678, 2001.

[66] C. V. Raman, "A Change of Wave-length in Light Scattering," *Nature*, vol. 121, p. 619619., 1928.

[67] D. W. Hahn, "Raman Scattering Theory." Department of Mechanical and Aerospace Engineering, University of Florida, 2007.

[68] J. Robertson, "Diamond-like Amorphous Carbon.," *Materials Science and Engineering: R: Reports*, vol. 37, no. 4-6, p. 129281, 2002.

[69] M. Newman, *Optimisation of the Electronic Properties of Graphene Devices*. PhD thesis, University of Leeds, School of Physics and Astronomy, 2012.

[70] G. G. Hoffmann, G. de With, and J. Loos, "Micro-Raman and Tip-Enhanced Raman Spectroscopy of Carbon Allotropes," *Macromolecular Symposia*, vol. 265, no. 1, p. 111, 2008.

[71] J. Hare, "Some Properties of Carbon and C60," accessed 01/09/2014, http://www.creative-science.org.uk/propc60.html.

[72] O. Gunnarsson, "Superconductivity in Fullerides," *Reviews of Modern Physics*, vol. 69, no. 2, pp. 575–606, 1997.

[73] S. Leach, M. Vervloet, A. Desprs, E. Brheret, J. P. Hare, T. J. Dennis, H. W. Kroto, R. Taylor, and D. R. M. Walton, "Electronic Spectra and Transitions of the Fullerene C60," *Chemical Physics*, vol. 160, pp. 451 – 466, 1992.

[74] B. Mishori, E. A. Katz, D. Faiman, A. Belu-Marian, and Y. Shapira, "Electronic Properties of C60 Thin Films," *Fullerene Science and Technology*, vol. 6, pp. 113–124, 1998.

[75] J. Menendez and J. Page, "The Vibrational Modes of Buckminsterfullerene," accessed 20/08/2014, http://www.public.asu.edu/ cosmen/C60vibrations/modeassignments.htm.

[76] T. Klaus D. Sattler and F. Group, eds., *Handbook of Nanophysics: Clusters and Fullerenes*. CRC Press, 2011.

[77] N. F. Mott, *Metal-Insulator Transitions*. Taylor and Francis, 1990.

[78] M. I. Salkola, "Intermolecular Polaron and Bipolaron Tunneling in C60," *Physical Review B*, vol. 49, no. 14, p. 953338, 1994.

[79] S. Sanvito, "Molecular spintronics: The rise of spinterface science," *Nature Physics*, vol. 6, pp. 562–564, 2010.

[80] C. Barraud, P. Seneor, R. Mattana, S. Fusil, K. Bouzehouane, C. Deranlot, P. Graziosi, L. Hueso, I. Bergenti, V. Dediu, F. Petroff, and A. Fert, "Unravelling the Role of the Interface for Spin Injection into Organic Semiconductors," *Nature Physics*, vol. 6, pp. 615–620, 2010.

[81] V. A. Dediu, L. E. Hueso, I. Bergenti, and C. Taliani, "Spin routes in Organic Semiconductors," *Nature Materials*, vol. 8, pp. 707–716, 2009.

[82] A. R. Rocha, V. M. Garcia-Suarez, S. W. Bailey, C. J. Lambert, J. Ferrer, and S. Sanvito, "Towards Molecular Spintronics," *Nature Materials*, vol. 4, pp. 335–339, 2005.

[83] V. Dediu, M. Murgia, F. C. Matacotta, C. Taliani, and S. Barbanera, "Room Temperature Spin Polarized Injection in Organic Semiconductor," *Solid State Communications*, vol. 122, pp. 181 – 184, 2002.

[84] A. Fert and H. Jaffres, "Conditions for Efficient Spin Injection from a Ferromagnetic Metal into a Semiconductor," *Physical Review B*, vol. 64, p. 184420, 2001.

[85] L. Lin, Z. Y. Pang, F. G. Wang, M. S. Lv, T. L. Yang, L. N. Ye, and S. H. Han, "The Origination of Ill-Defined Layer in Organic Spin Valves," *Applied Surface Science*, vol. 255, pp. 5682–5685, 2009.

[86] Y. Zhou, M. Ogawa, M. Bao, W. Han, R. K. Kawakami, and K. L. Wang, "Engineering of Tunnel Junctions for Prospective Spin Injection in Germanium," *Applied Physics Letters*, vol. 94, p. 242104, 2009.

[87] L. Landau and E. Lifshitz, "On the Theory of the Dispersion of Magnetic Permeability in Ferromagnetic Bodies," *Physikalische Zeitschrift der Sowjetunion*, vol. 8, p. 153169, 1935.

[88] C. Kittel, *Introduction to Solid State Physics*. John Wiley & Sons, Inc, 2005.

[89] L. Berger, "Emission of Spin Waves by a Magnetic Multilayer Traversed by a Current," *Physical Review B*, vol. 54, no. 13, p. 935358, 1996.

[90] Y. Tserkovnyak, A. Brataas, and G. E. W. Bauer, "Enhanced Gilbert Damping in Thin Ferromagnetic Films," *Physical Review Letters*, vol. 88, p. 117601, 2002.

[91] K. Ellmer, "Magnetron Sputtering of Transparent Conductive Zinc Oxide: relation between the sputtering parameters and the electronic properties," *Journal of Physics D-Applied Physics*, vol. 33, pp. R17–R32, 2000.

[92] F. M. Penning, "Sputtering Apparatus Paper," *Physica*, vol. 3, no. 9, p. 873, 1936.

[93] E. W. Williams, "An Introduction to Sputtering of Magnetic and Magneto-optic Thin Films for Data Recording," *Journal of Magnetism and Magnetic Materials*, vol. 95, no. 3, p. 356, 1991.

[94] N. Porter, *Magnetoresistance in n-type Silicon*. PhD thesis, University of Leeds, School of Physics and Astronomy, 2010.

[95] W. D. Sproul, D. J. Christie, and D. C. Carter, "Control of Reactive Sputtering Processes," *Thin Solid Films*, vol. 491, no. 12, pp. 1–17, 2005.

[96] M. Gobbi, *Spintronic Devices Based on Fullerene C60*. PhD thesis, NanoGune, 2013.

[97] M. M. Woolfson, *An Introduction to X-ray Crystallography*. Cambridge: Cambridge University Press, 1970.

[98] J. Als-Nielson and D. McMorrow, *Elements of Modern X-ray Physics*. Hoboken, New Jersey: John Wiley and Sons, 2001.

[99] S. D. Bader, "SMOKE," *Journal of Magnetism and Magnetic Materials*, vol. 100, no. 1-3, pp. 440–454, 1991.

[100] D. A. Allwood, G. Xiong, M. D. Cooke, and R. P. Cowburn, "Magneto-optical Kerr Effect Analysis of Magnetic Nanostructures," *Journal of Physics D-Applied Physics*, vol. 36, pp. 2175–2182, 2003.

[101] I. Yuitoo, S. Sasaki, and Y. Hamakawa, "Study of the Direction of Magnetization and Noise of Magnetic Thin Films Using a Scanning Kerr Effect Microscope," *Journal of Magnetism and Magnetic Materials*, vol. 159, no. 3, p. 395400., 1996.

[102] S. S. Kalarickal, P. Krivosik, M. Wu, C. E. Patton, M. L. Schneider, P. Kabos, T. J. Silva, and J. P. Nibarger, "Ferromagnetic Resonance Linewidth in Metallic Thin Films: Comparison of Measurement Methods.," *Journal of Applied Physics*, vol. 99, no. 9, p. 093909, 2006.

[103] C. E. Patton, "Linewidth and Relaxation Processes for the Main Resonance in the Spin Wave Spectra of NiFe Alloy Films," *Journal of Applied Physics*, vol. 39, no. 7, p. 306068, 1968.

[104] I. Bady, "Measurement of Linewidth of Single Crystal Ferrites by Monitoring the Reflected Wave in Short-circuited Transmission Line," *IEEE Transactions on Magnetics*, vol. 3, no. 3, p. 52126, 1967.

[105] F. J. Cadieu, R. Rani, W. Mendoza, B. Peng, S. A. Shaheen, M. J. Hurben, and C. E. Patton, "Static Magnetic and Microwave Properties of Li-ferrite Films Prepared by Pulsed Laser Deposition," *Journal of Applied Physics*, vol. 81, no. 8, p. 48013, 1997.

[106] W. Barry, "A Broad-Band, Automated, Stripline Technique for the Simultaneous Measurement of Complex Permittivity and Permeability," *IEEE Transactions on Microwave Theory and Techniques*, vol. 34, no. 1, p. 8084, 1986.

[107] W. K. Hiebert, A. Stankiewicz, and M. R. Freeman, "Direct Observation of Magnetic Relaxation in a Small Permalloy Disk by Time-Resolved Scanning Kerr Microscopy," *Physical Review Letters*, vol. 79, no. 6, p. 113437, 1997.

[108] Y. Chen, D. Hung, Y. Yao, S. Lee, H. Ji, and C.Yu, "Ferromagnetic Resonance Study of Thickness-dependent Magnetization Precession in Ni80Fe20 Films," *Journal of Applied Physics*, vol. 101, no. 9, 2007.

[109] M. Wormington, C. Panaccione, K. M. Matney, and D. K. Bowen, "Characterization of Structures from X-ray Scattering Data Using Genetic Algorithms," *Philosophical Transactions of the Royal Society of London A: Mathematical, Physical and Engineering Sciences*, vol. 357, no. 1761, p. 282748, 1999.

[110] M. E. Schabes, "Micromagnetic Theory of Non-uniform Magnetization Processes in Magnetic Recording Particles," *Journal of Magnetism and Magnetic Materials*, vol. 95, no. 3, p. 24988, 1991.

[111] W. H. Meiklejohn and C. P. Bean, "New Magnetic Anisotropy," *Physical Review*, vol. 105, pp. 904–913, 1957.

[112] Q. Zhenghong, J. M. Sivertsen, and J. H. Judy, "Magnetic Behavior of NiFe/NiO Bilayers," *Journal of Applied Physics*, vol. 83, no. 11, p. 682527, 1988.

[113] Y. Kamiguchi, H. Iwasaki, H. N. Fuke, K. Saito, and M. Sahashi, "Spin-Valve Giant Magnetoresistive films with Antiferromagnetic Ir-Mn layers," *Journal of Applied Physics*, vol. 81, pp. 4004–4006, 1997.

[114] Y. T. Chen, Y. Lin, S. Jen., J. Y. Tseng, and Y. D. Yao, "Effect of Ta Seed Layer on Crystalline Structure and Magnetic Properties in an Exchange-biased Co/IrMn System," *Journal of Alloys and Compounds*, vol. 509, pp. 5587–5590, 2011.

[115] C. Leighton, J. Nogues, B. J. Jonsson-Akerman, and I. K. Schuller, "Coercivity Enhancement in Exchange Biased Systems Driven by Interfacial Magnetic Frustration," *Physical Review Letters*, vol. 84, pp. 3466–3469, 2000.

[116] M. Ali, C. H. Marrows, and B. J. Hickey, "Suppression of Magnetization Ripple by Exchange Bias," *Physical Review B*, vol. 79, p. 064415, 2009.

[117] T. Tahmasebi, S. N. Piramanayagam, R. Sbiaa, R. Law, and T. C. Chong, "Effect of Different Seed Layers on Magnetic and Transport Properties of Perpendicular Anisotropic Spin Valves," *IEEE Transactions on Magnetics*, vol. 46, pp. 1933–1936, 2010.

[118] N. P. Aley, S. Takayama, A. Hirohata, and K. OGrady, "Enhancement of Exchange Bias in the Co2FeSi/IrMn System," *IEEE Transactions on Magnetics*, vol. 47, pp. 3490–3493, 2011.

[119] S. F. Parker, S. M. Bennington, J. W. Taylor, H. Herman, I. Silverwood, P. Albers, and K. Refson, "Complete Assignment of the Vibrational Modes of C60 by Inelastic Neutron Scattering Spectroscopy and Periodic-DFT," *Physical Chemistry Chemical Physics*, vol. 13, p. 77897804, 2011.

[120] J. G. Hou, Y. Wang, W. Xu, S. Y. Zhang, and Z. Jian, "Synthesis and Characterization of AgC60 Nanostructure film," *Applied Physics Letters*, vol. 70, p. 3110, 1997.

[121] M. R. C. Hunt, S. Modesti, P. Rudolf, and R. E. Palmer, "Charge-Transfer and Structure in C60 Adsorption on Metal-Surfaces," *Physical Review B*, vol. 51, no. 15, p. 1003947, 1995.

[122] O. Cespedes, M. S. Ferreira, S. Sanvito, M. Kociak, and J. M. D. Coey, "Contact Induced Magnetism in Carbon Nanotubes," *Journal of Physics: Condensed Matter*, p. L155L161, 2004.

[123] F. J. Wang, C. G. Yang, Z. V. Vardeny, and X. G. Li, "Spin Response in Organic Spin Valves Based on LSMO Electrodes," *Physical Review B*, vol. 75, p. 245324, 2007.

[124] J. H. Shim, K. V. Raman, Y. J. Park, T. S. Santos, G. X. Miao, B. Satpati, and J. S. Moodera, "Large Spin Diffusion Length in an Amorphous Organic Semiconductor," *Physical Review Letters*, vol. 100, 2008.

[125] W. Thompson, "Effects of Magnetization on the Electric Conductivity of Nickel and of Iron," *Proceedings of the Royal Society*, vol. 8, p. 546, 1857.

[126] C. M. Wang, "Anisotropic Magnetoresistance in a Two-Dimensional Electron system with Rashba and Dresselhaus Spin-Orbit Coupling," *Physical Review B*, vol. 82, pp. 165331–(1–14), 2010.

[127] S. Andreev and P. Dimitrova, "Anisotropic-Magnetoresistance Integrated Sensors," *Journal of Optoelectronics and Advanced Materials*, vol. 7, pp. 199–206, 2005.

[128] J. Akerman, M. DeHerrera, J. Slaughter, R. Dave, J. Sun, J. Martin, and S. Tehrani, "Intrinsic Reliability of AlOx-Based Magnetic Tunnel Junctions," *IEEE Transactions on Magnetics*, vol. 42, pp. 2661 – 2663, 2006.

[129] R. Benabderrahmane, M. Kanoun, N. Bruyant, C. Baraduc, A. Bsiesy, and H. Achard, "Al2O3 Tunnel Barrier as a Good Candidate for Spin Injection into Silicon," *Solid-State Electronics*, vol. 54, no. 8, p. 74144, 2010.

[130] R. J. M. van de Veerdonk, J. Nowak, R. Meservey, J. S. Moodera, and W. J. M. deJonge, "Current Distribution Effects in Magnetoresistive Tunnel Junctions," *Applied Physics Letters*, vol. 71, pp. 2839–2841, 1997.

[131] S. Zhang, P. M. Levy, A. C. Marley, and S. S. P. Parkin, "Quenching of Magnetoresistance by Hot Electrons in Magnetic Tunnel Junctions," *Physical Review Letters*, vol. 79, p. 374447, 1997.

[132] E. Y. Tsymbal, O. N. Mryasov, and P. R. LeClair, "Spin-dependent Tunnelling in Magnetic Tunnel Junctions," *Journal of Physics: Condensed Matter*, vol. 15, pp. R109–R142, 2003.

[133] W. David, R. Ibberson, T. Dennis, J. Hare, and K. Prassides, "Structural Phase-Transitions in the Fullerene C60," *Europhysics Letters*, vol. 18, no. 3, p. 21925, 1992.

[134] R. J. M. van de Veerdonk et al *ICMFS Conf. digests 15th*, pp. 74–75, 1997.

[135] R. Meservey, P. M. Tedrow, and P. Fulde, "Magnetic Field Splitting of Quasiparticle States in Superconducting Aluminum Films," *Physical Review Letters*, vol. 25, no. 18, p. 1270, 1970.

[136] P. M. Tedrow and R. Meservey, "Spin-Dependent Tunneling into Ferromagnetic Nickel," *Physical Review Letters*, vol. 26, no. 4, p. 192, 1971.

[137] P. M. Tedrow and R. Meservey, "Spin Polarization of Electrons Tunneling from Films of Fe, Co, Ni, and Gd," *Physical Review B*, vol. 7, no. 1, p. 31826, 1973.

[138] R. Meservey and P. M. Tedrow, "Spin-polarized Electron Tunneling," *Physics Reports*, vol. 238, no. 4, p. 173243, 1994.

[139] H. L. Wang, C. H. Du, Y. Pu, R. Adur, P. C. Hammel, and F. Y. Yang, "Large Spin Pumping from Epitaxial Y3Fe5O12 Thin Films to Pt and W Layers," *Physical Review B*, vol. 88, no. 10, p. 100406, 2013.

[140] O. Mosendz, J. E. Pearson, F. Y. Fradin, G. E. W. Bauer, S. D. Bader, and A. Hoffmann, "Quantifying Spin Hall Angles from Spin Pumping: Experiments and Theory," *Physical Review Letters*, vol. 104, no. 4, p. 046601, 2010.

[141] S. M. Rezende, R. L. Rodrguez-Surez, M. M. Soares, L. H. Vilela-Leo, D. L. Domnguez, and A. Azevedo, "Enhanced Spin Pumping Damping in Yttrium Iron garnet/Pt Bilayers," *Applied Physics Letters*, vol. 102, no. 1, p. 012402, 2013.

[142] S. R. Marmion, M. Ali, M. McLaren, D. A. Williams, and B. J. Hickey, "Temperature Dependence of Spin Hall Magnetoresistance in Thin YIG/Pt Films," *Physical Review B*, vol. 89, no. 22, p. 220404, 2014.

[143] A. A. Serga, A. V. Chumak, and B. Hillebrands, "YIG Magnonics," *Journal of Physics D: Applied Physics*, vol. 43, no. 26, p. 264002., 2010.

[144] B. J. Isherwood, "An X-ray Multiple Diffraction Study of Yttrium Iron Garnet Crystals," *Journal of Applied Crystallography*, vol. 1, no. 5, p. 299307, 1968.

[145] B. Bhoi, N. Venkataramani, R. Aiyar, and S. Prasad, "FMR and Magnetic Studies on Polycrystalline YIG Thin Films Deposited Using Pulsed Laser," *IEEE Transactions on Magnetics*, vol. 49, no. 3, p. 99094, 2013.

[146] N. Biziere and C. Fermon, "Dc Effect in a Single Micrometric Spin Valve Sensor Under Ferromagnetic Resonance," *Applied Physics Letters*, vol. 92, no. 9, p. 092503, 2008.

[147] N. Biziere and C. Fermon, "High-frequency Giant Magnetoresistance Measurement to Study the Dynamics of a Micron-scale Spin-valve Sensor," *Physical Review B*, vol. 78, no. 6, p. 064408, 2008.

[148] B. U. School of Chemistry, "Superconductivity Theory - Background," accessed 10/09/2014, http://www.chm.bris.ac.uk/webprojects2000/igrant/theory.html.

[149] Z. X. Luo, X. Cheng, Y. Luo, B. H. Loo, A. D. Peng, and J. N. Yao, "Photoassisted Magnetization of Fullerene C60 with Magnetic-Field Trapped Raman Scattering," *Journal of the American Chemical Society*, vol. 134, no. 2, p. 1130, 2012.

[150] S. C. Jeoung, D. Kim, S. Kim, and S. K. Kim, "Triplet-State Raman-Spectra of C60 and C70," *Chemical Physics Letters*, vol. 241, no. 5-6, p. 528, 1995.

[151] A. Chernikov, V. Bornwasser, M. Koch, S. Chatterjee, C. N. Bttge, T. Feldtmann, M. Kira, S. W. Koch, T. Wassner, S. Lautenschlger, B. K. Meyer, and M. Eickhoff, "Phonon-assisted Luminescence of Polar Semiconductors: Frohlich Coupling versus Deformation-potential Scattering," *Physical Review B*, vol. 85, p. 035201, 2012.

[152] S. Essig, C. Marquardt, A. Vijayaraghavan, M. Ganzhorn, S. Dehm, F. Hennrich, F. Ou, A. A. Green, C. Sciascia, F. Bonaccorso, K.-P. Bohnen, H. v. Lhneysen, M. M. Kappes, P. M. Ajayan, M. C. Hersam, A. C. Ferrari, and R. Krupke, "Phonon-Assisted Electroluminescence from Metallic Carbon Nanotubes and Graphene," *Nano Letters*, vol. 10, p. 1589, 2010.

[153] B. R. Gautam, T. D. Nguyen, E. Ehrenfreund, and Z. V. Vardeny, "Magnetic Field Effect Spectroscopy of C60-based Films and Devices," *Journal of Applied Physics*, vol. 113, no. 14, p. 143102, 2013.

[154] J. L. Sauvajol, Z. Hricha, N. Coustel, Z. Zahab, and R. Aznar, "Photoluminescence of Solid C60," *Journal of Physics: Condensed Matter*, vol. 5, no. 13, p. 2045, 1993.

[155] N. Tombros, C. Jozsa, M. Popinciuc, H. T. Jonkman, and B. J. van Wees., "Electronic Spin Transport and Spin Precession in Single Graphene Layers at Room Temperature," *Nature*, vol. 448, no. 7153, p. 57174, 2007.

[156] K. Tsukagoshi, B. W. Alphenaar, and H. Ago, "Coherent Transport of Electron Spin in a Ferromagnetically Contacted Carbon Nanotube," *Nature*, vol. 401, no. 6753, p. 57274, 1999.

[157] C. Boehme and J. M. Lupton, "Challenges for Organic Spintronics," *Nature Nanotechnology*, vol. 8, no. 9, p. 61215., 2013.

[158] G. van der Laan, "Applications of Soft X-ray Magnetic Dichroism," *Journal of Physics: Conference Series*, vol. 430, no. 1, p. 012127, 2013.

[159] D. S. Bethune, R. D. Johnson, J. Salem, M. S. Devries, and C. S. Yannoni, "Atoms in Carbon Cages - the Structure and Properties of Endohedral Fullerenes," *Nature*, vol. 366, no. 6451, p. 12328, 1993.

[160] M. Murata, Y. Murata, and K.Komatsu, "Synthesis and Properties of Endohedral C60 Encapsulating Molecular Hydrogen," *Journal of the American Chemical Society*, vol. 128, no. 24, p. 802433, 2006.